

Cancer Metabolism Historical Perspectives: A Chronicle of Controversies and Consensus

Chi V. Dang^{1,2,3,4}

¹Ludwig Institute for Cancer Research, New York, New York 10017, USA

²Department of Oncology, Johns Hopkins University School of Medicine, Baltimore, Maryland 21205, USA

³Department of Biochemistry and Molecular Biology, Johns Hopkins University Bloomberg School of Public Health, Baltimore, Maryland 21205, USA

⁴Bloomberg-Kimmel Institute for Cancer Immunotherapy, Sidney Kimmel Comprehensive Cancer Center, Johns Hopkins University, Baltimore, Maryland 21287, USA

Correspondence: cvdang@jhmi.edu; cdang@lcr.org

A century ago, Otto Warburg's work sparked the field of cancer metabolism, which has since taken a tortuous path. As evidence accumulated over the decades, consensus views of causes of cancer emerged, whereby genetic and epigenetic oncogenic drivers promoted immune evasion and induced new blood vessels and neoplastic metabolism to support tumor growth. Neoplastic cells abandon social cues of intercellular cooperation, escape tissue confinement, metastasize, and ultimately kill the host. Herein, key milestones in the study of cancer metabolism are chronicled with an emphasis on carbohydrate metabolism. The field began with a cancer cell–autonomous view that has been refined by a richer understanding of solid cancers as growing, immune-suppressive, complex organs comprising different cell types that are nourished by a variety of nutrients and variable amounts of oxygen through abnormal neovasculatures. Based on foundational historical studies, our current understanding of cancer metabolism offers a hopeful outlook for targeting metabolism to enhance cancer therapy.

The origin of life is thought to arise in part from a nascent nonenzymatic glycolytic pathway that is common to all self-sustaining life forms (Ralser 2018). In fact, the last hypothetical universal common ancestor (LUCA) of all cells is surmised to use nonoxidative sugar metabolism (Weiss et al. 2016). LUCA evolved long before the Great Oxidation Event resulting from the proliferation of photosynthetic organisms some 2.4 billion years ago (Holland 2006).

The availability of oxygen enabled the emergence of mitochondria as synthetic organelles to power eukaryotic metabolism and promote the evolution of metazoans. Oxygen availability also leads to reactive, toxic metabolic wastes. These byproducts, in addition to exogenous genotoxins, can corrupt the life-propagating encoded information, leading to cell growth arrest, death, or neoplastic cell transformation. In this way, the evolved metabolic processes of metazo-

C.V. Dang

ans not only enable such complex life forms but also imperil them. In turn, deregulated neoplastic cell growth and proliferation also depend on these evolved metabolic pathways, but in ways that may distinguish neoplastic from physiologic metabolism.

EARLY CONCEPTS OF CANCER BIOLOGY

In 1885, Ernst Freund reported that blood glucose levels were elevated in individuals with cancer (Freund 1885) and proposed that glucose must sustain cancer. On this subject, the *New York Times* reported on December 23, 1887 that blood from the German Prince Frederick III, who married Queen Victoria's daughter, was to be analyzed for excess sugar to determine whether his laryngeal nodule was a cancer (Baron 1999). During this time, a small laryngeal biopsy by Morell Mackenzie, a leading head and neck surgeon sent by Queen Victoria, was rendered nonmalignant by Rudolph Virchow (Baron 1999). Based on the biopsy results, Mackenzie suggested that extensive surgical resection with high morbidity should not be undertaken. Unfortunately, for Prince Frederick, the nodule was not benign and progressive cancer was later diagnosed (Mackenzie 1888). The result of the Freund "diagnostic" blood test could not be found in the detailed Mackenzie report (Mackenzie 1888). In any event, the validity of Freund's test was questioned by a subsequent December 24, 1887 *New York Times* precis pointing to the possibility that the association of high blood sugar and cancer could be coincidental in patients with preexisting diabetes mellitus, and that one condition did not cause the other. Intriguingly, diabetes with hyperinsulinemia is now known to be a major risk factor for developing cancer (Gallagher and LeRoith 2020).

In parallel around the same time, some of the first information about cancer's interactions with the immune system and genomic alterations were uncovered. The surgeon William Coley noted that a patient with sarcoma underwent complete remission after a severe postsurgical wound infection with *Streptococcus pyogenes* and surmised that the infection was critical for

the cure (Hoption Cann et al. 2003). In the 1890s, he developed a vaccine of killed bacteria (known as "Coley's toxins") to inoculate his patients and found complete remission of a sarcoma in his first patient. Arguably, this was the first cancer immunotherapy approach without the knowledge of the immediate cause of cancer or the role of tumor immunity. In 1902, Theodor Boveri speculated that malignant tumors could result from "certain abnormal chromosome constitution" based on his studies of chromosomes of fertilized urchin eggs and the appearance of tumor-like growths when chromosomes were present in imbalanced numbers (Boveri 2008), laying the groundwork for modern cancer genomics.

In the early 1900s, the cause of aneuploidy and the substance of heredity in chromosomes were unknown, but a clue for the cause of cancer was reported in a seminal 1911 paper (Rous 1911) by Peyton Rous, documenting that chicken tumor cell-free extracts can induce avian cancers. In this paper, Rous also noted spontaneous regression of these chicken tumors, which were found to have an "accumulation of lymphocytes," now known as tumor-infiltrating lymphocytes. Rous' observations were initially obscured but later led to the discovery of the Rous sarcoma virus, which proved to be foundational for the discovery of retroviral oncogenes.

The biochemistry of cancer was boosted by Otto Warburg who won the Nobel prize in 1931 for his discovery of cytochrome *c* oxidase (Warburg 1928). It was not his Nobel discovery, but a series of papers (Warburg 1930) in the 1920s underscoring the connection between altered glucose metabolism and cancer that brought Warburg into the limelight of cancer research. He provided evidence for what he believed to be the key cause of cancer—damaged cellular respiration.

In 1933, Hans Krebs found that among amino acids, glutamate-exposed guinea pig kidney consumed the most oxygen and noted an accompanying diminished ammonia level (Krebs 1935). In the same year, Dickens and Greville also noted that spleen, Jensen rat sarcoma, and rat or chick embryos produced large amounts of ammonia in the absence of sugar (Dickens and

Greville 1933). Krebs reported in 1935 the findings of an enzyme system for the synthesis of glutamine from glutamate and ammonia as well as the enzyme hydrolysis of glutamine, reversing the reaction (Krebs 1935). These observations documented the existence of glutamine synthetase and glutaminase, which are now known to play critical roles in tumor glutamine metabolism (Altman et al. 2016).

In 1945, Leuchtenberger and colleagues reported the striking finding of complete remissions of spontaneous murine mammary tumors treated with folic acid (Leuchtenberger et al. 1945). Based on these results, Sidney Farber treated 11 children with lethal acute lymphocytic leukemia (ALL) with folate and observed an “acceleration phenomenon” in the bone marrow of these patients (Farber 1949). This unexpected acceleration of the leukemia led Farber to the idea of using antifolates to treat leukemia. Farber reported clinical responses of childhood ALL to aminopterin in the landmark 1948 paper (Farber and Diamond 1948), underscoring the importance of inhibiting one-carbon metabolism in cancer and laying the foundation for modern chemotherapy (Stine et al. 2022). It should be noted that acute leukemias, which can proliferate in circulation, are distinctly different from solid tumors that have complex tumor microenvironments and grow slower. The rapid proliferation of leukemias requires heightened metabolism that renders them more responsive to cytotoxic therapies. A recent study using *in vivo* isotopic labeling and mass spectrometry (Fig. 1) underscores the difference between liquid and solid tumors, showing that tricarboxylic acid (TCA) cycling is higher in leukemia compared to solid tumors (Bartman et al. 2023).

Cancer neovascularization emerged in 1945 (Algire et al. 1945) as another key concept in cancer biology and one intimately connected to energy delivery and waste disposal. The work by Algire et al. recorded the appearance of new blood vessels in grafted normal tissues or tumor grafts. They observed that vascularization of normal transplanted tissues increased over a week and the emergence of arterioles and venules became visible. In contrast, tumors recruited new capillaries rapidly over 3 days evolving into large

vessels that did not develop into arterioles or venules. The tumor neovasculature is disordered but the tumors continued to be able to recruit new vasculature as they grew (Folkman et al. 1971). Without neo-angiogenesis, solid tumors would be limited to sizes less than ~200 μm in diameter, the limit of tissue oxygen diffusion (Carmeliet and Jain 2000).

In retrospect, synthesis of observations from the late 1800s into the 1950s provides a picture of solid cancer as a neoplastic mass, often with genomic changes, which can arise from a cell-free viral tumor extract, requires neovascularization, consumes glucose to produce lactate, consumes amino acids, converts glutamine to glutamate and ammonia, and is sensitive to one-carbon metabolism inhibition. The apparent conflicting observations that folate reduced the growth of mammary tumors but accelerated childhood leukemia suggest that fast-growing liquid tumors require folate for neoplastic growth and perhaps in the case of mammary tumors, folate may be required for the function of the antitumor arm of the immune system, although that was not appreciated at the time (Ron-Harel et al. 2016). More clearly, the observations of complete remissions induced by Coley’s toxin underscored the importance of tumor immunity even before key concepts of innate and adaptive immunity were known.

OTTO WARBURG, CARL AND GERTY CORI, AND AEROBIC GLYCOLYSIS

Otto Warburg was a meticulous quantitative biochemist who innovated the “Warburg” manometric apparatus (Fig. 1A) that permitted precise measurements of glucose and oxygen consumption as well as carbon dioxide and lactate production by thin slices of normal or cancer tissues. His early studies of sea urchin eggs led to the finding that, upon fertilization, there was a rapid rise in oxygen consumption. Hence, he postulated that cancer tissue, being proliferative, would consume high amounts of oxygen relative to normal tissues. Instead of higher oxygen consumption, he reported in 1924 (Warburg 1930) that the Flexner–Jobling rat liver carcinoma tissue slices did not take up more oxygen than normal liver,

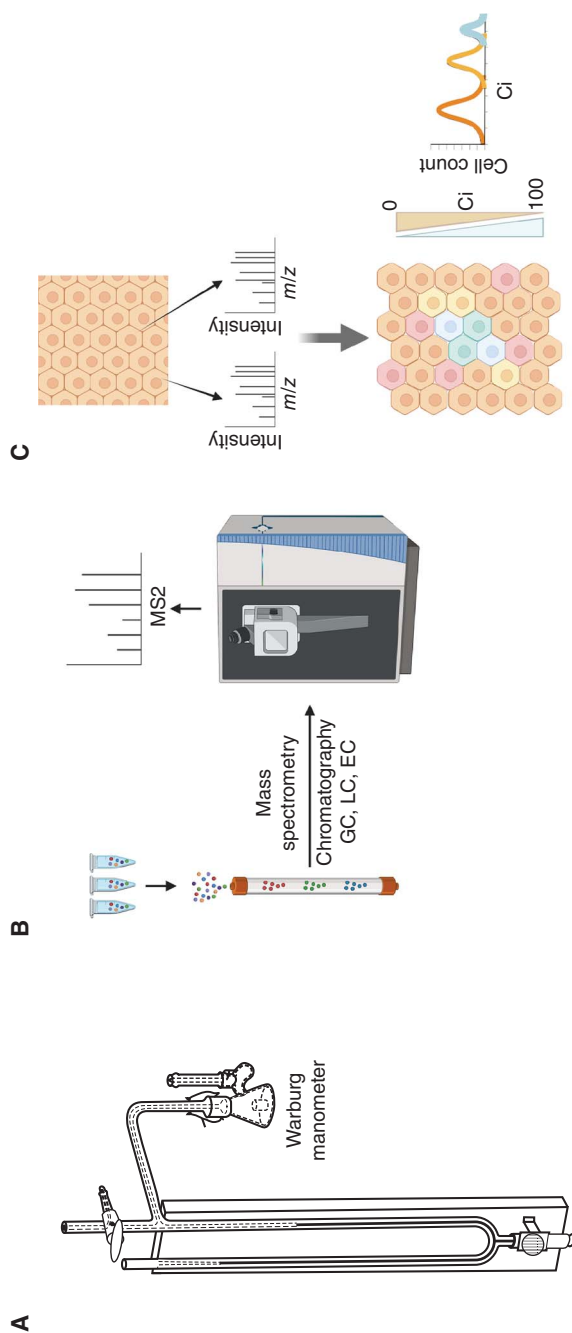


Figure 1. From Warburg manometer to mass spectrometry. Cancer metabolism research over the last century has been advanced by emerging technologies from the (A) Warburg manometer, to (B) mass spectrometry, and (C) illustration showing spatial mass spectrometry imaging of a tissue section that generates relative densities of metabolite signal intensity across the tissue section. The graph (*right*) depicts cell counts as a function of the distribution of signal intensities (Ci) of a metabolite. Each technological advance offers additional views of the complexity of cancer metabolism particularly in the context of the tumor immune microenvironment. (GC) Gas chromatography, (LC) liquid chromatography, (EC) electrochemical. (Figure created with BioRender.com.)

but rather the carcinoma produced more lactate than normal liver under oxygenated conditions (Warburg 1925). Known as the Pasteur effect first described in 1861 (Racker 1974), oxygen was documented to suppress glycolysis in yeast. The converse whereby glucose suppresses respiration is known as the Crabtree effect (Crabtree 1929). As such, the heightened glycolytic feature in cancer tissues bypasses the Pasteur effect resulting in aerobic glycolysis, the ability to undergo glycolysis in the presence of oxygen that was coined the “Warburg effect” by Efraim Racker (Fig. 2; Racker 1972).

The propensity of cancers to take up glucose avidly and convert the vast majority to lactate, or the Warburg effect, became a paradigm for cancer research in the early and mid-1900s. This concept, generated largely from *in vitro* experiments, was studied in tumors by Carl and Gerty Cori and reported in 1925 (Cori and Cori 1925a, b). They found that glucose levels tend to be diminished in mouse and rat tumors compared to normal muscle. Likewise, tumor lactate levels were diminished compared to muscle in fasting animals. Hence, they reasoned that tumor lactate might be washed away by blood circulation and surmised that an increase in glucose by intraperitoneal injection could reveal the propensity of tumors to produce high lactate levels. Indeed, when glucose was administered, tumor glucose levels rose significantly and were accompanied by an elevation of tumor lactate, a phenomenon that was not seen with normal liver. Further, they found that blood lactate levels were more elevated in tumor-bearing animals than in non-tumor-bearing animals after glucose administration. Thus, they concluded that the *in vivo* experiments were not contradictory to the *in vitro* findings of Warburg, but rather the production of tumor lactate depends on the availability of circulating glucose. Their continued studies of glucose and lactate metabolism led to the 1947 Nobel prize discovery of the Cori cycle (Cori and Cori 1929), the conversion of glucose by muscle to lactate that in turn is converted to liver glycogen, which can be mobilized to produce circulating glucose (Fig. 3A).

Corroborating earlier studies of Rous sarcomas (Cori and Cori 1925b), Warburg and col-

leagues published in 1927 (Warburg et al. 1927) the study of tumor metabolism *in vivo*. The experimental approach was meticulous, requiring the dissection of normal or tumor arterial and venous vessels from the anesthetized animal for the collection of efferent and afferent blood (Fig. 3A). The major blood vessels were sampled, and a drop in glucose level was found in each case from the arterial to venous side. Compared to these normal differences in glucose levels, the drop across Jensen sarcomas were pronounced, suggesting that the consumption of glucose was higher in the tumor. When measuring arteriovenous differences in lactic acid level, they found that most organs consumed lactate, except for the brain (i.e., comparing levels in arterial vs. venous “Jugularis”). In contrast to evidence of lactate consumption by normal tissues, in all 10 Jensen tumors, venous lactate was much higher than arterial levels, indicating that Jensen tumors consumed glucose and produced lactate. These studies corroborated the findings by the Coris a few years earlier (Cori and Cori 1925b) and supported the notion of the Warburg effect in tumors (Fig. 3A). Intriguingly, these historical studies are now largely substantiated by more sophisticated mass spectrometry (Fig. 1B) with the use of isotopically labeled substrates such as glucose, lactate, or 2-deoxyglucose and modeling of metabolite distributions *in vivo* (Faubert et al. 2017; Liu et al. 2020; Bartman et al. 2023). Although lactate produced from glucose can be oxidized by tumors (Faubert et al. 2017), the Warburg effect has been documented in solid tumor models (Bartman et al. 2023), underscored by the utility of ¹⁸F-2-deoxyglucose clinical imaging of human cancers (Fig. 3B; Som et al. 1980; Nolop et al. 1987).

CANCER METABOLISM CONTROVERSIES

The dogma of the Warburg effect providing an oversimplified view of cancer metabolism began to be challenged with controversies that crescendoed into the 1960s. Crabtree sought to determine whether Warburg metabolism is an “exclusive feature of malignant tissues” and whether anaerobic versus aerobic glycolysis have any relationships to the magnitude of respiration

C.V. Dang

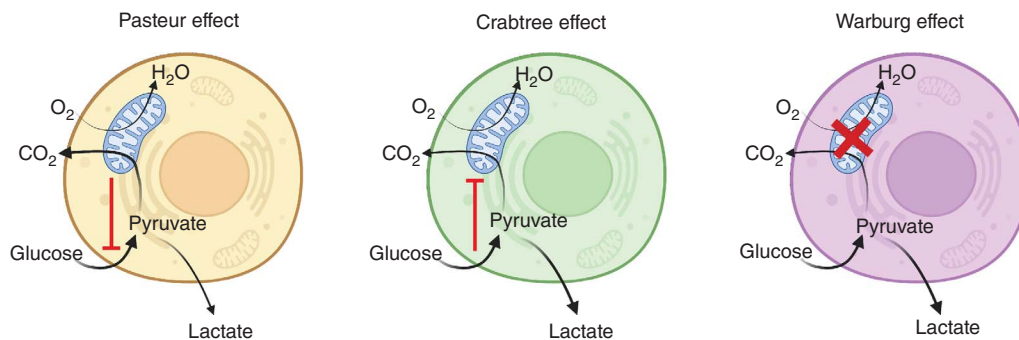


Figure 2. Pasteur, Crabtree, and Warburg effects. Generalized mammalian cells are depicted with the consumption of glucose through mitochondrial oxidation or glycolysis. Pasteur described the ability of oxygen to suppress yeast glycolysis that produces ethanol (not lactate as illustrated for mammalian cells), a phenomenon known as the Pasteur effect. Conversely, Crabtree found that some yeast strains demonstrated the ability of glucose to suppress respiration, known as the Crabtree effect. Warburg hypothesized that damaged mitochondria in cancer cells result in enhanced aerobic glycolysis, which bypasses the Pasteur effect, termed the Warburg effect. (Figure created with BioRender.com.)

(Crabtree 1928). Crabtree cited several publications documenting that nonmalignant tissues, such as the retina, placenta, and leukocytes, have high aerobic glycolysis, thereby questioning the validity of the Warburg hypothesis. Further, Crabtree used the Warburg manometer to study infectious nonmalignant lesions, such as pigeon pox, chicken vaccinia, or human warts or papillomas. He found that the excess glycolysis in pigeon pox slices was in the same order as those found by Warburg for tumor slices. Crabtree documented the elevation of glycolysis in Rous sarcoma tumors but surmised from his findings that changes accompanying the Warburg effect "... are not specific for malignant tissues but are a common feature of pathological overgrowths." Crabtree's historical findings presaged later studies that document virus-induced cellular glycolytic metabolism (Bissell et al. 1972; Thai et al. 2014).

The debate on the role of the Warburg effect in malignancies continued with camps on both sides digging into their positions. In studies of normal and tumor tissues, Elliott and Baker (1935) did not find differences in the Warburg effect between normal and tumor tissues (Elliott and Baker 1935) as compared to studies by Dickens (Dodds and Dickens 1940). Further, Boyland reported for the British Empire Cancer Campaign in 1940 and mentioned glycolysis, which

can be high in normal tissues, and hence is "... therefore impossible to consider this characteristic to be peculiar to tumours" (Boyland 1940a). This report resulted in a debate in *Nature* (March 30, 1940) between Dickens and Boyland about the merits of the Warburg effect in cancer (Boyland 1940b).

The ongoing debate on the Warburg effect was punctuated by Warburg's 1956 Science article that provided an overview titled "On the Origin of Cancer Cells" (Warburg 1956). He wrote with dogmatic authority, unshaken by contradictory data, that cancer cells have injured respiration (Fig. 2), and the resulting aerobic glycolysis causes cancer. He dismissed the roles of carcinogens and viruses in cancer, stating that "From this point of view, mutation and carcinogenic agent are not alternatives, but empty words, unless metabolically specified. Even more harmful in the struggle against cancer can be the continual discovery of miscellaneous cancer agents and cancer viruses, which, by obscuring the underlying phenomena, may hinder necessary preventive measures and thereby become responsible for cancer cases." Warburg's views on damaged respiration that drives glycolysis as a cause of cancer were challenged by Sidney Weinhouse (Weinhouse 1956) citing that isotope tracer studies revealed no difference between tumor and normal tissue in their conversion of glucose to

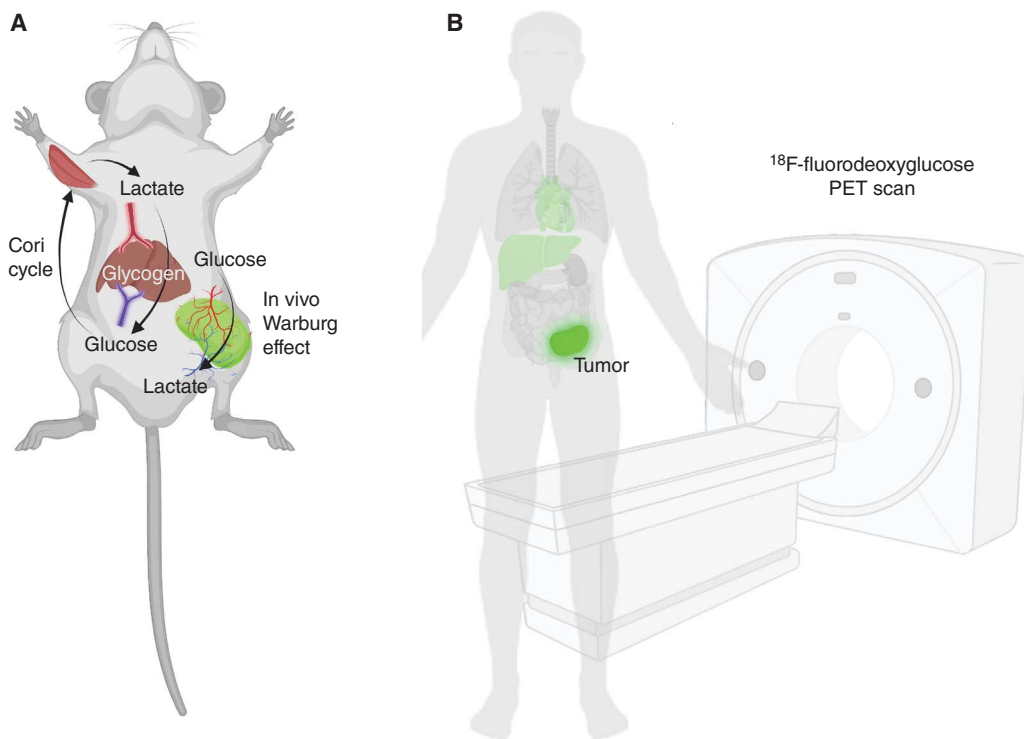


Figure 3. In vivo Warburg effect, the Cori cycle, and in vivo cancer positron emission tomography (PET) imaging. (A) By sampling arterial and venous blood across rodent normal organs, such as the liver, and tumors (green), Crabtree observed that increased glucose resulted in a higher lactate venous output from tumors than normal tissues, which tend to take up lactate from arterial blood. Warburg also documented that tumors have a propensity to convert high levels of glucose to lactate in vivo. In the case of liver, glycogen is produced through gluconeogenesis from muscle-generated lactate and in turn glucose released from glycogen can then be used by muscle in an interorgan circuit termed the Cori cycle. (B) The Warburg effect is exploited clinically to diagnose and monitor human cancers using an ¹⁸F-fluorodeoxyglucose PET scan. Normal heart and liver also accumulate ¹⁸F-labeled deoxyglucose, but tumors tend to have abnormally high uptake of the tracer (green). (Figure created with BioRender.com.)

carbon dioxide. Dean Burk (Burk and Schade 1956), another key figure, tipped the scale toward Warburg's aerobic glycolysis as a feature of cancer, but Burk acknowledged the validity of Weinhouse's objection to the concept of damaged mitochondria as a driver for malignancies. Warburg was wrong to dismiss an active role of mitochondria in tumorigenesis, in particular, since evidence shows the importance of mitochondrial function in cancer (Vasan et al. 2020).

Efraim Racker was a prolific biochemist who contributed fundamental insights into carbohydrate metabolism. His entry into cancer metabolism began with fundamental studies of glycolysis in the Ehrlich ascites tumor cells,

demonstrating that the conversion of glucose to lactate in cell extracts could be enhanced by the additional of purified phosphofructokinase and glyceraldehyde-3-phosphate dehydrogenase together with hexokinase, thereby defining the limiting glycolytic steps in ascites tumor extracts (Wu and Racker 1959). Skeptical of Warburg's damaged mitochondria hypothesis, Racker proposed that there are multiple causes of cancer, which share in common inefficient sodium-potassium ATPase pumps associated with aerobic glycolysis (Racker 1972). In 1981, Racker and Spector (1981) reported that the Src oncogenic kinase phosphorylates and suppresses the ATPase pump and thereby promotes aerobic gly-

C.V. Dang

colysis. This putative first link between an oncogene and the Warburg effect further overshadows observations of aerobic glycolysis in normal cells, such as mitogen-activated lymphocytes (Hedekov 1968) that in retrospect were perhaps the first reported glimpse of immunometabolism.

Racker's striking report of a link between an oncogene and tumor metabolism was, unfortunately, the result of scientific misconduct by his graduate student Spector (Racker 1989). The harbinger of misconduct was uncovered by the finding that ^{125}I iodine was spiked in his student's experiments to mimic the results of ^{32}P in the phosphorylation studies. The notion that Src drives the Warburg effect evaporated with this scandal. However, in 1983, Cooper in Hunter's laboratory and colleagues (Cooper et al. 1983) reported that enolase, phosphoglycerate kinase, and lactate dehydrogenase (LDH) were tyrosine phosphorylated in cells transformed by the Rous sarcoma virus bearing the v-Src oncogene, but the functional significance was unclear. During this time, an early study of positron emission tomography (PET) using ^{18}F -fluoro-2-deoxyglucose (FDG) showed enhanced glucose tumor uptake, assumed to be the Warburg effect, correlated with the degree of malignancy of cerebral gliomas (Di Chiro et al. 1982). The use of FDG PET (Fig. 3B) to detect altered cancer metabolism expanded (Hillner et al. 2008) and is now a standard of practice in clinical oncology.

The Warburg effect controversies distracted the literature from the key findings of Krebs (1935) and Dickens (Dodds and Dickens 1940) on the conversion of glutamine to glutamate and ammonia by normal tissues and the Jensen rat sarcoma. Glutamine was further shown by Eagle and coworkers in 1956 to be essential for mammalian cell growth in vitro (Eagle et al. 1956), providing the basis for Basal Medium Eagle. In 1983, consumption of glutamine was found to be increased in stimulated rat lymphocytes resulting in the production of glutamate, aspartate, and ammonia (Ardawi and Newsholme 1983). Brand reported (Brand et al. 1984) that concanavalin A-activated lymphocytes increased expression of glycolytic enzymes, enhancing glucose metabolism by 54-fold, whereby glucose was converted 90% to lactate and 1% was consumed for respi-

ration. This contrasts with resting lymphocytes that oxidize 27% of the glucose to CO_2 . Glutamine use increased by eightfold in stimulated lymphocytes, producing glutamate, ammonia, aspartate, and CO_2 . These foundational observations were largely forgotten in the current literature, but undoubtedly paved the way for recent studies on the use of glucose and glutamine for cancer metabolism (Cairns et al. 2011; DeBerardinis and Chandel 2016; Pavlova et al. 2022). In this respect, a recent tumor nutrient-partitioning study documents highest use of glutamine by tumor cells versus highest use of glucose by tumor myeloid cells in a mouse syngeneic MC38 colon tumor cell model (Reinfeld et al. 2021).

Warburg's controversial views on carbohydrate metabolism as the primary cause of cancer dominated the dialog on the biochemistry of cancer and ushered in an era of research on cancer metabolic pathways until the late 1970s when proto-oncogenes were discovered as precursors of viral oncogenes that drive neoplastic transformation. At the turn of the decade, in the 1980s, many oncogenes were discovered and documented to be altered in human cancers, opening a new chapter in cancer research focusing on the genetics of cancer (Varmus 1984). At this point, the interest in metabolism began to wane partly due to controversies over Warburg's dogmatic views and whether cancer metabolism is any different than normal metabolism. The field of cancer metabolism was further displaced by the view that oncogenes and tumor suppressors are the primary drivers of cancer with metabolism playing a subservient role to genetics.

ONCOGENES, TUMOR SUPPRESSORS, AND ALTERED TUMOR METABOLISM

The Src oncogene, fraudulently linked to the Warburg effect by Spector, appeared again with Ras in 1987, when Flier and coworkers (Flier et al. 1987) reported that rodent fibroblasts transfected with these oncogenes increased the mRNA expression of a glucose transporter and had increased uptake of 2-deoxyglucose. This connection between oncogenes and glucose uptake was further supported by the finding in 1989 that Ras and c-Mos-transformed NIH3T3 fibroblasts ex-

pressed more GAPDH than control cells (Persons et al. 1989). Intriguingly, Myc expression did not result in increased glucose transporter expression or glucose uptake in the Flier study (Flier et al. 1987), but the levels of GAPDH in NIH3T3 appeared to correlate with Myc expression in the Persons study (Persons et al. 1989). However, the detailed mechanistic links between these oncogenes and elevation of the glucose transporter mRNA were missing. Within a decade of these findings, Myc-dependent genes in Myc-transformed Rat1a fibroblasts were identified based on the notion that the product of the MYC oncogene behaves as a transcription factor (Kato et al. 1990; Lewis et al. 1997).

To identify Myc-responsive genes, control or anchorage-independent Myc-transformed Rat1a fibroblasts were grown in suspension cultures. Through representational difference analysis, a form of PCR-assisted subtraction cloning, over 20 putative Myc-responsive genes were identified (Lewis et al. 1997). Among these, lactate dehydrogenase A (LDHA) was transcriptionally induced in Rat1a-Myc cells as evidenced by nuclear run-on assays and Myc-binding sites that are required for Myc transactivation of an LDHA promoter-luciferase reporter (Shim et al. 1997). Importantly, Myc transformation was dependent on LDHA. The finding of LDHA among putative Myc target genes functionally linked Myc to the Warburg effect, providing a firm mechanistic link between an oncogene and aerobic glycolysis. Semenza and coworkers (Wang et al. 1995) cloned the hypoxia-inducible factor (HIF) gene, which was shown to induce the expression of many glycolytic genes under hypoxic conditions (Firth et al. 1994; Semenza et al. 1994). The induction of these genes by HIF to mediate anaerobic glycolysis contrasts with the ability of Myc to induce glycolysis under aerobic conditions (Dang and Semenza 1999).

In addition to the hypoxic stabilization of HIF-1 α and HIF-2 α proteins, HIF-1 is also thought to be stabilized by upstream oncogenic signaling. In this regard, HIF-driven metabolic rewiring downstream of oncogenic drivers contributes to neoplastic glycolytic metabolism and angiogenesis. Activation of mTORC1 by amino

acids and growth signaling through RHEB induces glucose metabolism through increasing Myc and HIF-1 α activity and expression (Düvel et al. 2010). It is intriguing to note that MYC is central to PI3K inhibitor resistance (Muellner et al. 2011) and oncogenic alterations of metabolism downstream of PI3K-Akt (Hoxhaj and Manning 2020). Moreover, RAS induces pancreatic cancer glycolytic metabolism (Reinfeld et al. 2021) in a MYC-dependent manner (Ying et al. 2012). In this context, it should be noted that the RAS-ERK pathway has been shown to increase Myc expression and protein levels (Farrell and Sears 2014). As such, the potential collaboration between MYC and HIF signaling downstream of oncogenic pathways could be central to the Warburg effect seen in different cancers.

Subsequent to the observation on MYC-associated, glucose-deprivation-induced cell death (Shim et al. 1998), MYC overexpressing human cells were found to be addicted to glutamine (Yuneva et al. 2007), suggesting a role for MYC in regulating glutamine metabolism. In this respect, the Thompson (Wise et al. 2008) and Dang (Gao et al. 2009) laboratories independently reported the regulation of glutaminolysis by MYC, which activates glutaminase for the conversion of glutamine to glutamate and subsequent catabolism through the TCA cycle. Further, MYC is broadly involved in regulating many metabolic pathways including nucleotide and lipid metabolism (Dang 2012).

Based on their studies of the metabolism of activated T cells, Thompson and coworkers in 2002 reported that costimulation via CD28 triggered a PI3K-Akt-dependent activation of glycolysis (Frauwirth et al. 2002). While Akt was a known oncogene, first identified as the cellular homolog of v-Akt found in the rodent AKT8 retrovirus, activating mutations of PIK3Ca (PI3K) in human cancers were not reported until 2004 (Samuels et al. 2004). In this respect, activated Akt was documented to drive aerobic glycolysis (Elstrom et al. 2004) and subsequent studies underscore the ability of Akt to directly phosphorylate and activate HK2 and PFKFBP2 (Hoxhaj and Manning 2020).

Loss-of-function of tumor suppressors also contributes to altered oncogenic metabolism

(Levine and Puzio-Kuter 2010; Humpton and Vousden 2016). For example, increased expression of the tumor suppressor PTEN, which opposes PI3K, resulted in heightened oxidative metabolism *in vivo* (Garcia-Cao et al. 2012), which is the phenotypic converse of the activation of glycolysis by PI3K (Hu et al. 2016). The tumor suppressor p53 tends to diminish glycolysis in favor of a more heightened oxidative metabolism (Humpton and Vousden 2016). This is in part driven by p53 activation of TIGAR as reported (Bensaad et al. 2006). Further, p53 induces synthesis of cytochrome *c* oxidase (SCO2) to drive mitochondrial respiration, such that loss of wild-type p53 decreased SCO2 expression, resulting in increased glycolysis (Matoba et al. 2006). Conversely, mitochondrial function affects p53 response. Inhibition of mitochondrial complex III or dihydroorotate dehydrogenase (DHODH) activity depletes pyrimidines and activates p53 (Ladds et al. 2018; Mick et al. 2020). In this respect, p53 is both downstream and upstream of metabolic perturbations. The tumor-suppressive effects of tuberous sclerosis complex TSC1 and TSC2 and alteration of metabolism are largely through their ability to inhibit mTOR activity (Manning and Cantley 2003). The tumor suppressor retinoblastoma (RB) has been implicated in glutamine metabolism, such that loss of Rb enhanced E2F-mediated expression of ASCT2- and E2F-independent increase in GLS (Reynolds et al. 2014).

Intriguingly, at the same time that canonical oncogenes were shown to impact metabolism, several core metabolic enzymes were shown to behave as tumor suppressors. Inherited mutations of several nuclear-encoded mitochondrial components, including succinate dehydrogenase subunits SDHB, SDHC, and SDHD and fumarate hydratase (FH), predispose to family syndromes of cancers such as pheochromocytoma, paraganglioma, leiomyosarcoma, and chromophobe renal cell carcinoma (Gottlieb and Tomlinson 2005). These findings suggest that these enzymes are tumor suppressive and the mechanism underlying their tumor-suppression function in part involves HIF stabilization (Selak et al. 2005) and epigenetic modification. For example, SDH mutation causes an accumulation

of succinate, which inhibits α -ketoglutarate-dependent prolyl hydroxylases and stabilizes HIF-1 α (Selak et al. 2005), whereas FH mutations cause an accumulation of fumarate, which inhibits α -ketoglutarate-dependent demethylases and leads to epigenomic alterations that drive epithelial–mesenchymal transition (EMT) (Sciacovelli et al. 2016). These direct links between metabolic enzyme mutations and familial cancer underscore the importance of metabolic perturbation as a cancer driver.

EMERGING CANCER METABOLISM CONSENSUS

Considering general principles, it is apt to distinguish between maintenance and proliferative metabolism (Vander Heiden et al. 2009). Maintenance metabolism is required to sustain and renew cellular structures and functions by providing ATP to support membrane potentials and protein synthesis. These processes are diurnally dynamic, driven by the circadian clock core transcription factor Clock: Bmal1, whose oncogenic perturbation is documented (Sancar and Van Gelder 2021). As such, normal metabolic studies *in vivo* can be affected by this diurnal fluctuation that enables daily oscillation of cellular metabolism to synchronize with organismal feeding and fasting cycles.

Proliferative metabolism, on the other hand, can result from normal growth signaling such as activation of T cells, proliferation of bone marrow cells required to replace cellular blood components, or proliferation of the gut epithelium. Upon growth stimulation, signaling through Ras-MEK-ERK signaling cascade activates and stabilizes MYC to induce metabolic and growth-related mRNAs such as those for glucose or amino acid transporter to import nutrients for cell growth (Dang 2012). The influx of amino acids and growth signal transduction through PI3K-Akt-TSC2-RHEB activates mTOR to induce translation and protein synthesis (Cantor and Sabatini 2012). Together, MYC and mTOR can be envisioned to amplify transcription and translation (Hoxhaj and Manning 2020), respectively, of growth signaling and drive proliferative metabolism (Fig. 4). The hypoxia-independent

A Historical Perspective on Cancer Metabolism

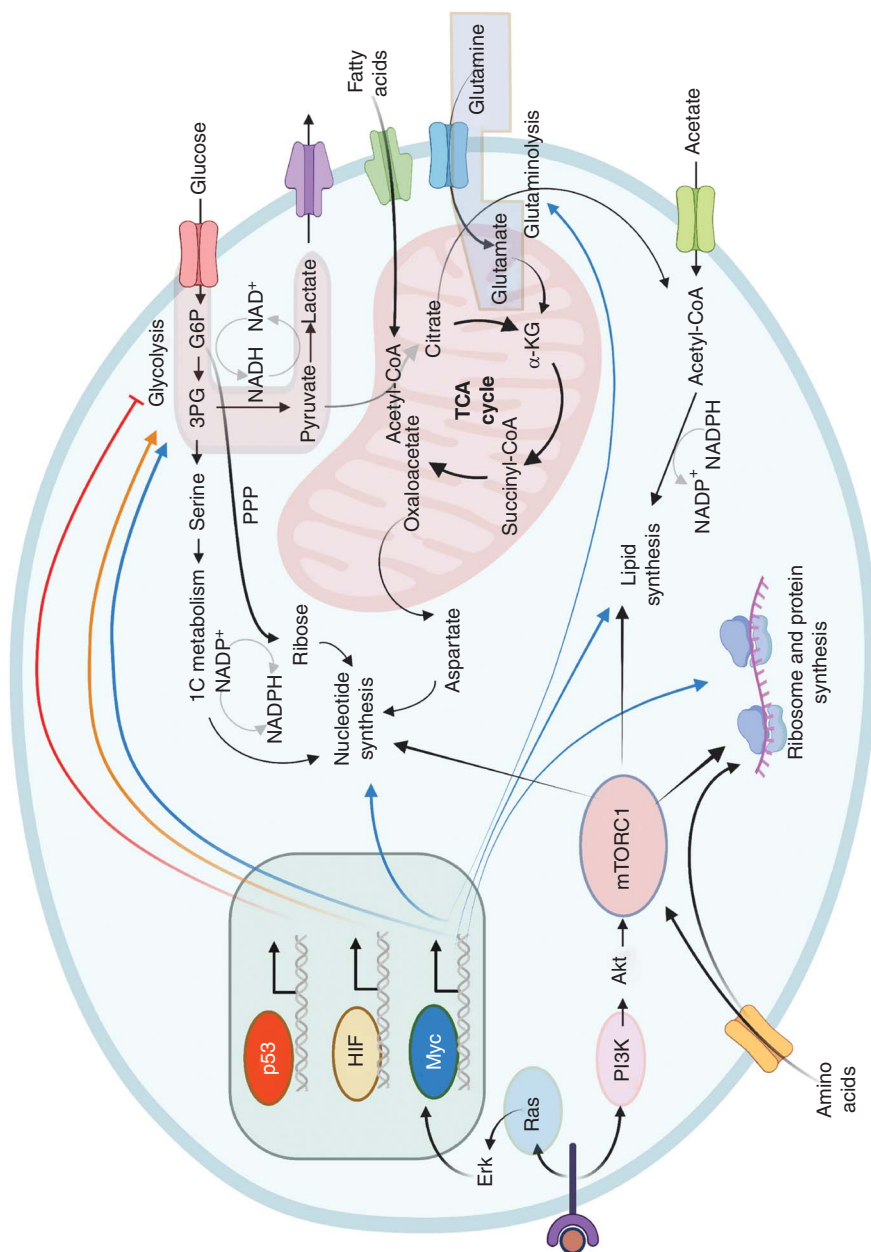


Figure 4. Oncogenic alterations of metabolism. The diagram shows a cell with an activated growth factor receptor (left) triggering signal transduction down the Ras-MEK-Erk pathway to activate Myc. Growth signal is also transmitted down the PI3K-Akt pathway to activate mTORC1, which senses amino acids for full activation. Myc, in turn, activates genes involved in anabolic metabolism, driving glycolysis, glutaminolysis, nucleotide, lipid, and protein synthesis. mTORC1 amplifies growth signaling by stimulating translation and protein synthesis for mass accumulation that includes its direct activation of nucleotide and lipid synthesis. The hypoxia-inducible factor (HIF) can be induced by mTORC1 and stabilized under hypoxia to induce anaerobic glycolysis. On the other hand, the tumor suppressor p53 suppresses glycolysis and induces mitochondrial respiration. Note that the prevalent human oncogenes Ras and PI3K are upstream of Myc and mTORC1, enabling transcriptional and translational amplification of oncogenic cell growth and proliferation. Fatty acids as an energy source through oxidation is depicted. (1C) One-carbon, (PPP) pentose phosphate pathway. (Figure created with BioRender.com.)

C.V. Dang

stabilization of HIF-1 is not necessary but can contribute to proliferative metabolism and induction of tumor neovascularization (Fig. 4). Tumor suppressors such as PTEN and TSC2 attenuate the growth signaling pathways driven by PI3K and mTORC1, respectively (Cantor and Sabatini 2012). Hence, loss of these tumor suppressors increased signaling through these oncogenic pathways and their effects on metabolism. p53 can attenuate Myc function by sensing an overactive Myc-Arf axis (Zindy et al. 1998) or suppress proliferation by sensing DNA replication or ribosomal stress (Lindström et al. 2022). p53 can sense ribosomal stress when MDM2 is bound to specific ribosomal subunits and release p53 from its grip. Increased p53 function, in turn, inhibits glycolysis and increases respiration (Fig. 4).

A key question is whether there are key differences between normal proliferative versus oncogenic metabolism (Vander Heiden et al. 2009). As discussed previously, the Warburg effect can be observed in cancers and normal tissues. For example, whereas resting T cells use less glycolysis and rely on oxidative metabolism, T-cell receptor (TCR) stimulation of murine T cells induces a proliferative metabolic program resembling that of malignant lymphocytes (Madden and Rathmell 2021). Specifically, stimulation of T cells with anti-CD3 and anti-CD28 drives glycolysis and glutaminolysis in a Myc-dependent fashion that enables proliferation, which does not depend on HIF-1 α (Fig. 5A; Wang et al. 2011). Upon withdrawal of stimulation, T cells undergo apoptosis and some attain a resting memory oxidative metabolic state. In contrast to normal T cells, oncogenic NOTCH-driven T-cell lymphomas are dependent on constitutive MYC expression, which drives a constitutive proliferation metabolic profile that cannot return to a resting state (Zhou et al. 2022). In this regard, a difference in normal versus neoplastic proliferative metabolism is that the former can be turned off. In contrast, the latter is constitutively turned on, rendering the malignant state addicted to a constant supply of nutrients. Normal cells have mechanisms that sense nutrient deprivation such as AMPK, which can induce cell growth arrest. However, MYC-addicted cells are vulner-

able to glucose or glutamine deprivation-induced cell death as are AKT-addicted cells (Shim et al. 1998; Elstrom et al. 2004; Yuneva et al. 2007). Given these observations, are there sufficient therapeutic indices to exploit metabolism for cancer therapy?

METABOLIC THERAPY AND LESSONS LEARNED

When considering metabolic vulnerabilities of cancers, recent studies have highlighted the importance of tissue-specific metabolic effects of oncogenic drivers, metabolic plasticity, diet, as well as the impact of these features on the microbiome and antitumor immunity. Different oncogenes induce different metabolic profiles in the same organ. For example, in contrast to MYC, which drives glutamine and glucose metabolism in MYC-inducible liver cancer, MET oncogene-driven liver cancer expresses glutamine synthetase and hence appears less dependent on exogenous glutamine (Yuneva et al. 2012). On the other hand, the same oncogene can induce different metabolic effects in different tissues. Kras effects on branched chain amino metabolism are different in Kras, p53-loss-driven murine pancreatic adenocarcinoma versus non-small-cell lung cancer (NSCLC) (Mayers et al. 2016). In the former, branched chain amino acid (BCAA) uptake is diminished, whereas in NSCLC, the tumors incorporate BCAA into proteins. Hence, tissue-specific effects of oncogenes add to the complexity of tumor metabolism in vivo when considering the metabolic vulnerabilities of cancers.

Metabolic plasticity (Fendt et al. 2020) and metabolic stress such as activation of AMPK or the integrated stress-response pathways induce resistance to inhibition of cancer metabolism (Costa-Mattioli and Walter 2020). Metabolic plasticity was elegantly illustrated by Yuneva and coworkers using a MYC-inducible model of mouse HCC (Méndez-Lucas et al. 2020). They demonstrated that lost glutaminase (Gls) extended survival as seen with pharmacological Gls inhibition (Xiang et al. 2015). However, loss of hexokinase 2 (Hk2) did not extend survival. Intriguingly, loss of both Gls and Hk2 further

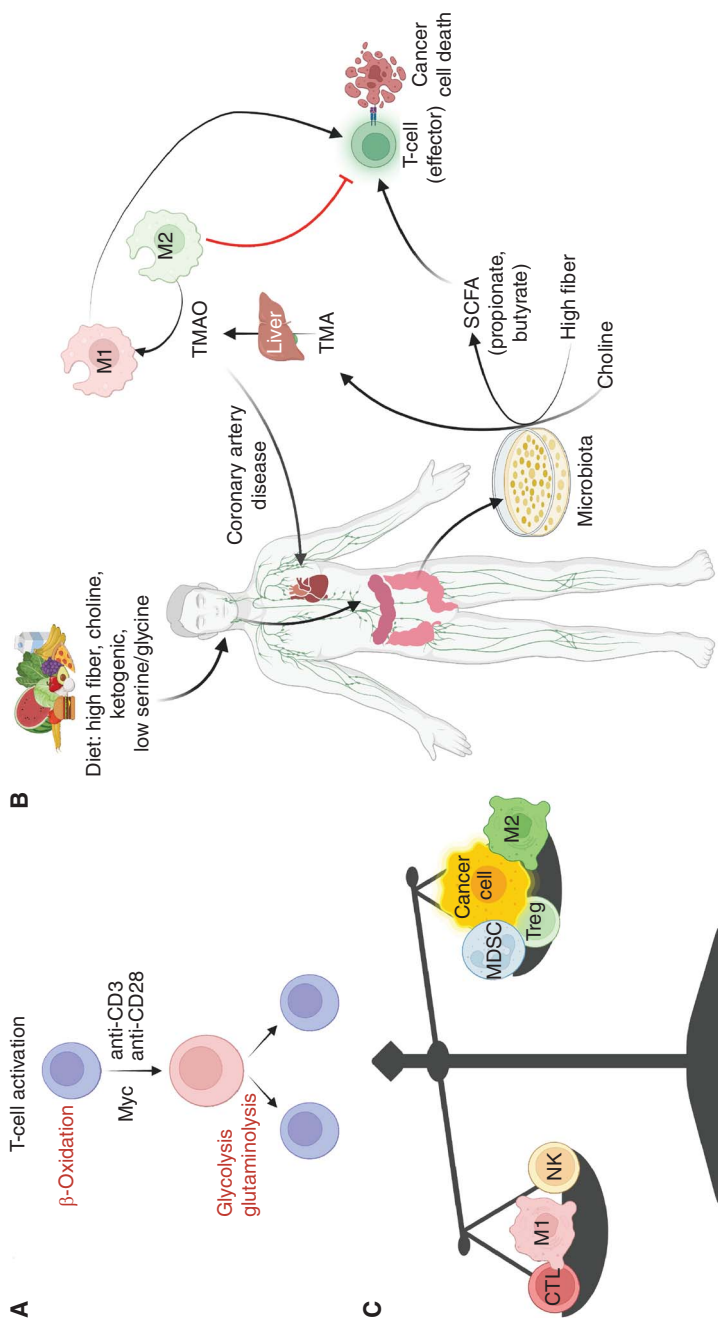


Figure 5. T-cell activation and the effect of diets on tumor and immune cell metabolism and fate. (A) Anti-CD3 plus anti-CD28 activation of resting primary murine T cells, which requires Myc, which activates glycolysis and glutaminolysis to drive biomass accumulation for cell proliferation. (B) Dietary high fiber or choline is shown to produce microbial short chain fatty acids (SCFAs) or trimethylamine (TMA) and liver-derived trimethylamine oxide (TMAO). SCFAs activate effector T cells, whereas TMAO polarizes macrophages toward inflammatory M1 states that increase coronary artery inflammation or enhance immune checkpoint blockade cancer therapy. Ketogenic diet affects the gut microbiota and tumor immunity; results from ongoing clinical studies are pending. Whether a serine/glycine deprivation diet proves to increase cancer therapy response in humans remains to be established. (C) The illustration depicts a scale balancing cells that have antitumor activity, such as cytotoxic CD8⁺ T cells (CD8), natural killer (NK) cells, or inflammatory M1 macrophages, versus cells, such as myeloid-derived suppressor cells (MDSCs), regulatory T (Treg) cells, or alternatively activated M2 macrophages that assist cancer cell growth. (CTL) Cytotoxic T-lymphocyte. (Figure created with BioRender.com.)

extended survival, but these double-knockout (KO) tumors eventually caused the demise of their hosts, indicating yet other ways that allow for neoplastic cells to circumvent metabolic blocks. This genetic evidence for metabolic plasticity is underscored by the cooperation between metabolic inhibitors, such as a combination of inhibitors of LDH and mitochondrial complex I, to slow tumor growth (Oshima et al. 2020).

Whereas loss of Hk2 did not extend survival of MYC-induced HCC, Hk2 is documented to be required for initiation and maintenance of murine KRas-driven lung cancer and ErbB2-driven breast cancer (Patra et al. 2013). Further, systemic deletion of Hk2 also reduced tumorigenesis in a diethylnitrosamine-induced murine model of HCC (DeWaal et al. 2018), and, importantly, loss of Hk2 did not affect T-cell proliferation or T-cell-mediated viral immunity (Mehta et al. 2018). Notably, some human multiple myelomas do not express hexokinase 1 and are highly sensitive to decreased HK2 (Xu et al. 2019). These observations suggest that HK2 is an example of an enzyme that appears to be cancer specific.

Under nutrient-depleted conditions, decreased mTOR activity and activation of AMPK induce ULK activity to drive autophagy, whereby autophagosomes are formed and destined for lysosomal degradation to recycle metabolites for survival (Onodera and Ohsumi 2005; Rabinowitz and White 2010). Further, mitophagy—a form of autophagy—is necessary to cull dysfunctional mitochondria. The maintenance of an NAD^+/NADH ratio $\gg 1$ to drive oxidative anabolism is essential for cell function. As such, under nutrient deprivation, autophagy maintains NAD^+ levels (Kataura et al. 2022). When the conversion of NADH to NAD^+ is saturated via mitochondrial NADH malate-aspartate and glycerol-3-phosphate dehydrogenase shuttles, aerobic glycolysis is induced to regenerate cytosolic NAD^+ to drive GADPH-mediated catalysis (Wang et al. 2022). Hence, pathways that can regenerate cytosolic NAD^+ when NADH is in excess could increase in activity when other pathways are limited. Excessive NADH levels induce reductive stress (Mick et al. 2020) and activate as the transcriptional

corepressor CtBP to generate an adaptive transcriptome (Di et al. 2013).

In the study of MYC-driven murine liver cancer (Méndez-Lucas et al. 2020), the loss of Psat1, which drives one-carbon metabolism through serine and glycine, did not affect survival. However, withdrawal of serine and glycine from the diet as done previously by Vousden et al. (Maddocks et al. 2017) prolonged the survival of Psat KO but not wild-type tumor-bearing animals (Méndez-Lucas et al. 2020). These findings underscore that the effect of diet depends on the metabolic wiring of the tumor cells (Kalaany and Sabatini 2009; Lien and Vander Heiden 2019). What was not accounted for in these studies is the effect of diet on the host microbiome or immunity. Since the availability of dietary L-serine can affect the gut microbiota during inflammation (Kitamoto et al. 2020), whether a serine/glycine deprivation diet influences tumor immunity beyond a cancer cell-autonomous effect remains to be established. In this regard, the ketogenic diet can alter the host microbiome (Fig. 5B; Ang et al. 2020) and curb several models of mouse tumorigenesis. Ketogenic diet curbs tumor growth in a model of mouse pancreatic adenocarcinoma in combination with chemotherapy (Yang et al. 2022). Further, this combination also worked in immunocompromised mice, but sustained response was observed only in mice with an intact immune system. Intriguingly, a ketogenic diet alters gut and serum metabolome in dogs with implications on tumor immunity (Allenspach et al. 2022).

Dietary choline can induce inflammation through its conversion to trimethylamine (TMA) by the gut microbiota, and in turn oxidized by the liver to trimethylamine oxide (TMAO), which is well-implicated in provoking coronary artery disease (Wang et al. 2015). Dietary choline or administration of TMAO induces inflammatory M1 macrophages (Fig. 5B) that increase graft-versus-host response as well as response of tumors to immune checkpoint blockade (Wu et al. 2020; Mirji et al. 2022). As such, there is much more to learn about the effects of components of diet, such as high fiber content that generates microbial short chain fatty acids with immune modulatory activities (Fig. 5B), on

the microbiota that in turn increase cancer therapy responses (He et al. 2021; Spencer et al. 2021).

The idea of targeting metabolism for cancer treatment was championed by Sidney Farber who targeted nucleotide synthesis with the “anti-metabolite” aminopterin and subsequently methotrexate, which is still used clinically (Farber and Diamond 1948; Farber 1949). Together with asparaginase, an active therapy in lymphoblastic leukemias, this demonstrates that metabolic therapies can be active anticancer agents. However, other metabolic therapies have proven less efficacious. The fact that 2-deoxyglucose can inhibit glycolysis made it a candidate for studies in cancer patients, but studies from decades ago showed that it did not produce clear benefit, and patients had side effects such as diaphoresis (Landau et al. 1958). Likewise, the glutamine analog 6-diazo-5-oxo-1-norleucine (DON), which targets a multitude of glutamine using enzymes and hence is imprecise, was also tested in humans, but it appeared too toxic for clinical use (Magill et al. 1957). It is notable that a DON prodrug has significant preclinical efficacy against several tumor models in immunocompetent mice (Leone et al. 2019). Whether clinical trials on DON prodrug prove to be effective remains to be seen. Recent failures of metabolic inhibitors in the clinic result from either lack of activity or intolerable side effects. For example, CB-839, which is a highly specific glutaminase (GLS) inhibitor with little associated side effects, failed in a study of patients with renal cell carcinoma due to a lack of efficacy (Tannir et al. 2022). The use of the mitochondrial complex I inhibitor IACS-07549 failed in clinical studies because of neurotoxicity (Yap et al. 2023). However, an exception is the successful implementation of specific inhibitors for mutant isocitrate dehydrogenases, IDH1 and IDH2, for the treatment of cancers such as acute myelogenous leukemia (DiNardo et al. 2018). Here, the therapeutic index is widened by the specificity of the drugs for mutant versus wild-type enzymes.

CONCLUDING REMARKS

Over the past century, Warburg’s studies on cancer metabolism and those reporting the use of Coley’s

toxin for cancer therapy lay the foundation for current studies that offer a hopeful outlook for new cancer therapeutic opportunities. Given the profound success of cancer immunotherapy, it should be noted that the use of metabolic inhibitors can interfere with or potentiate the antitumor arm of the immune system (Leone et al. 2019; Hermans et al. 2020). As such, the development of metabolic inhibitors to target cancer cells should also account for its potential adverse effect on antitumor immunity (Fig. 5C). Notably, a major challenge to effective immunotherapy is tumor acidity (Boedtker and Pedersen 2020; Tu et al. 2021; Gillies et al. 2022), whose mitigation in the clinical setting has not been sufficiently addressed by current research. The rapid improvement of mass spectrometry imaging (Ma and Fernández 2022) of tissues down to the single-cell level should provide the spatial resolution necessary to gain a richer understanding of the tumor immune microenvironment metabolic states (Fig. 1C) and potentially expose novel cancer metabolic vulnerabilities. The emerging field of immunometabolism (Buck et al. 2017; Leone and Powell 2020; Madden and Rathmell 2021; Stine et al. 2022) offers a richer understanding of metabolic vulnerabilities of immune versus cancer cells that is anticipated to provide novel druggable opportunities to enhance immunity while diminishing cancer cell viability.

ACKNOWLEDGMENTS

This historical perspective is from one viewpoint, and I realize that there may be alternative perspectives of the development of the field of cancer metabolism. In this respect, citations are limited and not meant to be comprehensive. I thank Adam Wolpaw, Rajeshkumar NV, and Zach Stine for comments. This work is supported in part by a Bloomberg Distinguished Professorship at Johns Hopkins, the Ludwig Institute for Cancer Research, and NCI grants R01 CA252225, CA051497, and CA053741.

REFERENCES

- Algire GH, Chalkley HW, Legliss FY, Park HD. 1945. Vascular reactions of normal and malignant tissues in vivo. I: Vascular reactions of mice to wounds and to normal and

C.V. Dang

- neoplastic transplants. *J Natl Cancer Inst* **6**: 73–85. doi:10.1093/jnci/6.1.73
- Allenspach K, Borchering DC, Iennarella-Servantez CA, Mosichuk AP, Atherly T, Sahoo DK, Kathrani A, Suchodolski JS, Bourgeois-Mochel A, Seroa MR, et al. 2022. Ketogenic diets in healthy dogs induce gut and serum metabolome changes suggestive of anti-tumourigenic effects: a model for human ketotherapy trials. *Clin Transl Med* **12**: e1047. doi:10.1002/ctm2.1047
- Altman BJ, Stine ZE, Dang CV. 2016. From Krebs to clinic: glutamine metabolism to cancer therapy. *Nat Rev Cancer* **16**: 619–634. doi:10.1038/nrc.2016.71
- Ang QY, Alexander M, Newman JC, Tian Y, Cai J, Upadhyay V, Turnbaugh JA, Verdin E, Hall KD, Leibel RL, et al. 2020. Ketogenic diets alter the gut microbiome resulting in decreased intestinal Th17 cells. *Cell* **181**: 1263–1275. e16. doi:10.1016/j.cell.2020.04.027
- Ardawi MS, Newsholme EA. 1983. Glutamine metabolism in lymphocytes of the rat. *Biochem J* **212**: 835–842. doi:10.1042/bj2120835
- Baron DN. 1999. A surgical mishap. *BMJ* **319**: 1360. doi:10.1136/bmj.319.7221.1360
- Bartman CR, Weilandt DR, Shen Y, Lee WD, Han Y, TeSlaa T, Jankowski CSR, Samarah L, Park NR, da Silva-Diz V, et al. 2023. Slow TCA flux and ATP production in primary solid tumours but not metastases. *Nature* **614**: 349–357. doi:10.1038/s41586-022-05661-6
- Bensaad K, Tsuruta A, Selak MA, Vidal MN, Nakano K, Bartrons R, Gottlieb E, Vousden KH. 2006. TIGAR, a p53-inducible regulator of glycolysis and apoptosis. *Cell* **126**: 107–120. doi:10.1016/j.cell.2006.05.036
- Bissell MJ, Hatie C, Rubin H. 1972. Patterns of glucose metabolism in normal and virus-transformed chick cells in tissue culture. *J Natl Cancer Inst* **49**: 555–565.
- Boedtkjer E, Pedersen SF. 2020. The acidic tumor microenvironment as a driver of cancer. *Annu Rev Physiol* **82**: 103–126. doi:10.1146/annurev-physiol-021119-034627
- Boveri T. 2008. Concerning the origin of malignant tumours by Theodor Boveri (translated and annotated by Henry Harris). *J Cell Sci* **121**: 1–84. doi:10.1242/jcs.025742
- Boylard E. 1940a. The British Empire cancer campaign. *Nature* **145**: 246–248. doi:10.1038/145246a0
- Boylard E. 1940b. Metabolism of tumours. *Nature* **145**: 513. doi:10.1038/145513a0
- Brand K, Williams JF, Weidemann MJ. 1984. Glucose and glutamine metabolism in rat thymocytes. *Biochem J* **221**: 471–475. doi:10.1042/bj2210471
- Buck MD, Sowell RT, Kaech SM, Pearce EL. 2017. Metabolic instruction of immunity. *Cell* **169**: 570–586. doi:10.1016/j.cell.2017.04.004
- Burk D, Schade AL. 1956. On respiratory impairment in cancer cells. *Science* **124**: 270–272. doi:10.1126/science.124.3215.270
- Cairns RA, Harris IS, Mak TW. 2011. Regulation of cancer cell metabolism. *Nat Rev Cancer* **11**: 85–95. doi:10.1038/nrc2981
- Cantor JR, Sabatini DM. 2012. Cancer cell metabolism: one hallmark, many faces. *Cancer Discov* **2**: 881–898. doi:10.1158/2159-8290.CD-12-0345
- Carmeliet P, Jain RK. 2000. Angiogenesis in cancer and other diseases. *Nature* **407**: 249–257. doi:10.1038/35025220
- Cooper JA, Reiss NA, Schwartz RJ, Hunter T. 1983. Three glycolytic enzymes are phosphorylated at tyrosine in cells transformed by Rous sarcoma virus. *Nature* **302**: 218–223. doi:10.1038/302218a0
- Cori CF, Cori GT. 1925a. The carbohydrate metabolism of tumors. I: The free sugar, lactic acid, and glycogen content of malignant tumors. *J Biol Chem* **64**: 11–22. doi:10.1016/S0021-9258(18)84944-4
- Cori CF, Cori GT. 1925b. The carbohydrate metabolism of tumors. II: Changes in the sugar, lactic acid, and CO₂ combining power of blood passing through a tumor. *J Biol Chem* **65**: 397–405. doi:10.1016/S0021-9258(18)84849-9
- Cori CF, Cori GT. 1929. Glycogen formation in the liver from *d*- and *l*-lactic acid. *J Biol Chem* **81**: 389–403. doi:10.1016/S0021-9258(18)83822-4
- Costa-Mattioli M, Walter P. 2020. The integrated stress response: from mechanism to disease. *Science* **368**: eaat5314. doi:10.1126/science.aat5314
- Crabtree HG. 1928. The carbohydrate metabolism of certain pathological overgrowths. *Biochem J* **22**: 1289–1298. doi:10.1042/bj0221289
- Crabtree HG. 1929. Observations on the carbohydrate metabolism of tumours. *Biochem J* **23**: 536–545. doi:10.1042/bj0230536
- Dang CV. 2012. MYC on the path to cancer. *Cell* **149**: 22–35. doi:10.1016/j.cell.2012.03.003
- Dang CV, Semenza GL. 1999. Oncogenic alterations of metabolism. *Trends Biochem Sci* **24**: 68–72. doi:10.1016/S0968-0004(98)01344-9
- DeBerardinis RJ, Chandel NS. 2016. Fundamentals of cancer metabolism. *Sci Adv* **2**: e1600200. doi:10.1126/sciadv.1600200
- DeWaal D, Nogueira V, Terry AR, Patra KC, Jeon SM, Guzman G, Au J, Long CP, Antoniewicz MR, Hay N. 2018. Hexokinase-2 depletion inhibits glycolysis and induces oxidative phosphorylation in hepatocellular carcinoma and sensitizes to metformin. *Nat Commun* **9**: 446. doi:10.1038/s41467-017-02733-4
- Di LJ, Byun JS, Wong MM, Wakano C, Taylor T, Bilke S, Baek S, Hunter K, Yang H, Lee M, et al. 2013. Genome-wide profiles of CtBP link metabolism with genome stability and epithelial reprogramming in breast cancer. *Nat Commun* **4**: 1449. doi:10.1038/ncomms2438
- Di Chiro G, DeLaPaz RL, Brooks RA, Sokoloff L, Kornblith PL, Smith BH, Patronas NJ, Kufta CV, Kessler RM, Johnston GS, et al. 1982. Glucose utilization of cerebral gliomas measured by ¹⁸F-fluorodeoxyglucose and positron emission tomography. *Neurology* **32**: 1323–1323. doi:10.1212/WNL.32.12.1323
- Dickens F, Greville GD. 1933. Metabolism of normal and tumour tissue: ammonia and urea formation. *Biochem J* **27**: 1123–1133. doi:10.1042/bj0271123
- DiNardo CD, Stein EM, de Botton S, Roboz GJ, Altman JK, Mims AS, Swords R, Collins RH, Mannis GN, Pollyea DA, et al. 2018. Durable remissions with ivosidenib in *IDH1*-mutated relapsed or refractory AML. *N Engl J Med* **378**: 2386–2398. doi:10.1056/NEJMoa1716984
- Dodds EC, Dickens F. 1940. The biochemistry of malignant tissue. *Annu Rev Biochem* **9**: 423–458. doi:10.1146/annurev.bi.09.070140.002231

- Düvel K, Yecies JL, Menon S, Raman P, Lipovsky AI, Souza AL, Triantafellow E, Ma Q, Gorski R, Cleaver S, et al. 2010. Activation of a metabolic gene regulatory network downstream of mTOR complex 1. *Mol Cell* **39**: 171–183. doi:10.1016/j.molcel.2010.06.022
- Eagle H, Oyama VI, Levy M, Horton CL, Fleischman R. 1956. The growth response of mammalian cells in tissue culture to L-glutamine and L-glutamic acid. *J Biol Chem* **218**: 607–616. doi:10.1016/S0021-9258(18)65826-0
- Elliott KA, Baker Z. 1935. The respiratory quotients of normal and tumour tissue. *Biochem J* **29**: 2433–2441. doi:10.1042/bj0292433
- Elstrom RL, Bauer DE, Buzzai M, Karnauskas R, Harris MH, Plas DR, Zhuang H, Cinalli RM, Alavi A, Rudin CM, et al. 2004. Akt stimulates aerobic glycolysis in cancer cells. *Cancer Res* **64**: 3892–3899. doi:10.1158/0008-5472.CAN-03-2904
- Farber S. 1949. Some observations on the effect of folic acid antagonists on acute leukemia and other forms of incurable cancer. *Blood* **4**: 160–167. doi:10.1182/blood.V4.2.160.160
- Farber S, Diamond LK. 1948. Temporary remissions in acute leukemia in children produced by folic acid antagonist, 4-aminopteroyl-glutamic acid. *N Engl J Med* **238**: 787–793. doi:10.1056/NEJM194806032382301
- Farrell AS, Sears RC. 2014. MYC degradation. *Cold Spring Harb Perspect Med* **4**: a014365. doi:10.1101/cshperspect.a014365
- Faubert B, Li KY, Cai L, Hensley CT, Kim J, Zacharias LG, Yang C, Do QN, Doucette S, Burguete D, et al. 2017. Lactate metabolism in human lung tumors. *Cell* **171**: 358–371.e9. doi:10.1016/j.cell.2017.09.019
- Fendt SM, Frezza C, Erez A. 2020. Targeting metabolic plasticity and flexibility dynamics for cancer therapy. *Cancer Discov* **10**: 1797–1807. doi:10.1158/2159-8290.CD-20-0844
- Firth JD, Ebert BL, Pugh CW, Ratcliffe PJ. 1994. Oxygen-regulated control elements in the phosphoglycerate kinase 1 and lactate dehydrogenase A genes: similarities with the erythropoietin 3' enhancer. *Proc Natl Acad Sci* **91**: 6496–6500. doi:10.1073/pnas.91.14.6496
- Flier JS, Mueckler MM, Usher P, Lodish HF. 1987. Elevated levels of glucose transport and transporter messenger RNA are induced by *ras* or *src* oncogenes. *Science* **235**: 1492–1495. doi:10.1126/science.3103217
- Folkman J, Merler E, Abernathy C, Williams G. 1971. Isolation of a tumor factor responsible for angiogenesis. *J Exp Med* **133**: 275–288. doi:10.1084/jem.133.2.275
- Frauwirth KA, Riley JL, Harris MH, Parry RV, Rathmell JC, Plas DR, Elstrom RL, June CH, Thompson CB. 2002. The CD28 signaling pathway regulates glucose metabolism. *Immunity* **16**: 769–777. doi:10.1016/S1074-7613(02)00323-0
- Freund E. 1885. Zur diagnose des karzinoms [To diagnose carcinomas]. *Wiener Medizinische Blätter* **9**: 268–269.
- Gallagher EJ, LeRoith D. 2020. Hyperinsulinaemia in cancer. *Nat Rev Cancer* **20**: 629–644. doi:10.1038/s41568-020-0295-5
- Gao P, Tchernyshyov I, Chang TC, Lee YS, Kita K, Ochi T, Zeller KI, De Marzo AM, Van Eyk JE, Mendell JT, et al. 2009. c-Myc suppression of miR-23a/b enhances mitochondrial glutaminase expression and glutamine metabolism. *Nature* **458**: 762–765. doi:10.1038/nature07823
- Garcia-Cao I, Song MS, Hobbs RM, Laurent G, Giorgi C, de Boer VC, Anastasiou D, Ito K, Sasaki AT, Rameh L, et al. 2012. Systemic elevation of PTEN induces a tumor-suppressive metabolic state. *Cell* **149**: 49–62. doi:10.1016/j.cell.2012.02.030
- Gillies RJ, Ibrahim-Hashim A, Ordway B, Gatenby RA. 2022. Back to basic: trials and tribulations of alkalinizing agents in cancer. *Front Oncol* **12**: 981718. doi:10.3389/fonc.2022.981718
- Gottlieb E, Tomlinson IP. 2005. Mitochondrial tumour suppressors: a genetic and biochemical update. *Nat Rev Cancer* **5**: 857–866. doi:10.1038/nrc1737
- He Y, Fu L, Li Y, Wang W, Gong M, Zhang J, Dong X, Huang J, Wang Q, Mackay CR, et al. 2021. Gut microbial metabolites facilitate anticancer therapy efficacy by modulating cytotoxic CD8⁺ T cell immunity. *Cell Metab* **33**: 988–1000.e7. doi:10.1016/j.cmet.2021.03.002
- Hedeskov CJ. 1968. Early effects of phytohaemagglutinin on glucose metabolism of normal human lymphocytes. *Biochem J* **110**: 373–380. doi:10.1042/bj1100373
- Hermans D, Gautam S, García-Cañaveras JC, Gromer D, Mitra S, Spolski R, Li P, Christensen S, Nguyen R, Lin JX, et al. 2020. Lactate dehydrogenase inhibition synergizes with IL-21 to promote CD8⁺ T cell stemness and antitumor immunity. *Proc Natl Acad Sci* **117**: 6047–6055. doi:10.1073/pnas.1920413117
- Hillner BE, Siegel BA, Liu D, Shields AF, Gareen IF, Hanna L, Stine SH, Coleman RE. 2008. Impact of positron emission tomography/computed tomography and positron emission tomography (PET) alone on expected management of patients with cancer: initial results from the National Oncologic PET Registry. *J Clin Oncol* **26**: 2155–2161. doi:10.1200/JCO.2007.14.5631
- Holland HD. 2006. The oxygenation of the atmosphere and oceans. *Philos Trans R Soc Lond B Biol Sci* **361**: 903–915. doi:10.1098/rstb.2006.1838
- Hoption Cann SA, van Netten JP, van Netten C. 2003. Dr William Coley and tumour regression: a place in history or in the future. *Postgrad Med J* **79**: 672–680. doi:10.1093/postgradmedj/79.938.672
- Hoxhaj G, Manning BD. 2020. The PI3K-AKT network at the interface of oncogenic signalling and cancer metabolism. *Nat Rev Cancer* **20**: 74–88. doi:10.1038/s41568-019-0216-7
- Hu H, Juvekar A, Lyssiotis CA, Lien EC, Albeck JG, Oh D, Varma G, Hung YP, Ullas S, Lauring J, et al. 2016. Phosphoinositide 3-kinase regulates glycolysis through mobilization of aldolase from the actin cytoskeleton. *Cell* **164**: 433–446. doi:10.1016/j.cell.2015.12.042
- Humpton TJ, Vouden KH. 2016. Regulation of cellular metabolism and hypoxia by p53. *Cold Spring Harb Perspect Med* **6**: a026146. doi:10.1101/cshperspect.a026146
- Kalaany NY, Sabatini DM. 2009. Tumours with PI3K activation are resistant to dietary restriction. *Nature* **458**: 725–731. doi:10.1038/nature07782
- Kataura T, Sedlackova L, Otten EG, Kumari R, Shapira D, Scialo F, Stefanatos R, Ishikawa KI, Kelly G, Seranova E, et al. 2022. Autophagy promotes cell survival by maintaining NAD levels. *Dev Cell* **57**: 2584–2598.e11. doi:10.1016/j.devcel.2022.10.008

C.V. Dang

- Kato GJ, Barrett J, Villa-Garcia M, Dang CV. 1990. An amino-terminal c-myc domain required for neoplastic transformation activates transcription. *Mol Cell Biol* **10**: 5914–5920.
- Kitamoto S, Alteri CJ, Rodrigues M, Nagao-Kitamoto H, Sugihara K, Himpls SD, Bazzi M, Miyoshi M, Nishioka T, Hayashi A, et al. 2020. Dietary L-serine confers a competitive fitness advantage to Enterobacteriaceae in the inflamed gut. *Nat Microbiol* **5**: 116–125. doi:10.1038/s41564-019-0591-6
- Krebs HA. 1935. Metabolism of amino acids: the synthesis of glutamine from glutamic acid and ammonia, and the enzymic hydrolysis of glutamine in animal tissues. *Biochem J* **29**: 1951–1969. doi:10.1042/bj0291951
- Ladds M, van Leeuwen IMM, Drummond CJ, Chu S, Healy AR, Popova G, Pastor Fernández A, Mollick T, Darekar S, Sedimbi SK, et al. 2018. A DHODH inhibitor increases p53 synthesis and enhances tumor cell killing by p53 degradation blockage. *Nat Commun* **9**: 1107. doi:10.1038/s41467-018-03441-3
- Landau BR, Laszlo J, Stengle J, Burk D. 1958. Certain metabolic and pharmacologic effects in cancer patients given infusions of 2-deoxy-D-glucose. *J Natl Cancer Inst* **21**: 485–494.
- Leone RD, Powell JD. 2020. Metabolism of immune cells in cancer. *Nat Rev Cancer* **20**: 516–531. doi:10.1038/s41568-020-0273-y
- Leone RD, Zhao L, Englert JM, Sun IM, Oh MH, Sun IH, Arwood ML, Bettencourt IA, Patel CH, Wen J, et al. 2019. Glutamine blockade induces divergent metabolic programs to overcome tumor immune evasion. *Science* **366**: 1013–1021. doi:10.1126/science.aav2588
- Leuchtenberger R, Leuchtenberger C, Laszlo D, Lewisohn R. 1945. The influence of “folic acid” on spontaneous breast cancers in mice. *Science* **101**: 46. doi:10.1126/science.101.2611.46.a
- Levine AJ, Puzio-Kuter AM. 2010. The control of the metabolic switch in cancers by oncogenes and tumor suppressor genes. *Science* **330**: 1340–1344. doi:10.1126/science.1193494
- Lewis BC, Shim H, Li Q, Wu CS, Lee LA, Maity A, Dang CV. 1997. Identification of putative c-Myc-responsive genes: characterization of *rcl*, a novel growth-related gene. *Mol Cell Biol* **17**: 4967–4978. doi:10.1128/MCB.17.9.4967
- Lien EC, Vander Heiden MG. 2019. A framework for examining how diet impacts tumour metabolism. *Nat Rev Cancer* **19**: 651–661. doi:10.1038/s41568-019-0198-5
- Lindström MS, Bartek J, Maya-Mendoza A. 2022. P53 at the crossroad of DNA replication and ribosome biogenesis stress pathways. *Cell Death Differ* **29**: 972–982. doi:10.1038/s41418-022-00999-w
- Liu S, Dai Z, Cooper DE, Kirsch DG, Locasale JW. 2020. Quantitative analysis of the physiological contributions of glucose to the TCA cycle. *Cell Metab* **32**: 619–628. e21. doi:10.1016/j.cmet.2020.09.005
- Ma X, Fernández FM. 2022. Advances in mass spectrometry imaging for spatial cancer metabolomics. *Mass Spectrom Rev* e21804. doi:10.1002/mas.21804
- Mackenzie M. 1888. *The fatal illness of Frederick the Noble*. Sampson Low, Marston, Searle & Rivington, London.
- Madden MZ, Rathmell JC. 2021. The complex integration of T-cell metabolism and immunotherapy. *Cancer Discov* **11**: 1636–1643. doi:10.1158/2159-8290.CD-20-0569
- Maddocks ODK, Athineos D, Cheung EC, Lee P, Zhang T, van den Broek NJF, Mackay GM, Labuschagne CF, Gay D, Kruiswijk F, et al. 2017. Modulating the therapeutic response of tumours to dietary serine and glycine starvation. *Nature* **544**: 372–376. doi:10.1038/nature22056
- Magill GB, Myers WP, Reilly HC, Putnam RC, Magill JW, Sykes MP, Escher GC, Karnofsky DA, Burchenal JH. 1957. Pharmacological and initial therapeutic observations on 6-diazo-5-oxo-1-norleucine (DON) in human neoplastic disease. *Cancer* **10**: 1138–1150. doi:10.1002/1097-0142(195711/12)10:6<1138::AID-CNCR2820100608>3.0.CO;2-K
- Manning BD, Cantley LC. 2003. Rheb fills a GAP between TSC and TOR. *Trends Biochem Sci* **28**: 573–576. doi:10.1016/j.tibs.2003.09.003
- Matoba S, Kang JG, Patino WD, Wragg A, Boehm M, Gavrilova O, Hurley PJ, Bunz F, Hwang PM. 2006. P53 regulates mitochondrial respiration. *Science* **312**: 1650–1653. doi:10.1126/science.1126863
- Mayers JR, Torrence ME, Danai LV, Papagiannakopoulos T, Davidson SM, Bauer MR, Lau AN, Ji BW, Dixit PD, Hosios AM, et al. 2016. Tissue of origin dictates branched-chain amino acid metabolism in ductal *Kras*-driven cancers. *Science* **353**: 1161–1165. doi:10.1126/science.aaf5171
- Mehta MM, Weinberg SE, Steinert EM, Chhiba K, Martinez CA, Gao P, Perlman HR, Bryce P, Hay N, Chandel NS. 2018. Hexokinase 2 is dispensable for T cell-dependent immunity. *Cancer Metab* **6**: 10. doi:10.1186/s40170-018-0184-5
- Méndez-Lucas A, Lin W, Driscoll PC, Legrave N, Novellademunt L, Xie C, Charles M, Wilson Z, Jones NP, Rayport S, et al. 2020. Identifying strategies to target the metabolic flexibility of tumours. *Nat Metab* **2**: 335–350. doi:10.1038/s42255-020-0195-8
- Mick E, Titov DV, Skinner OS, Sharma R, Jourdain AA, Mootha VK. 2020. Distinct mitochondrial defects trigger the integrated stress response depending on the metabolic state of the cell. *eLife* **9**: e49178. doi:10.7554/eLife.49178
- Mirji G, Worth A, Bhat SA, El Sayed M, Kannan T, Goldman AR, Tang HY, Liu Q, Auslander N, Dang CV, et al. 2022. The microbiome-derived metabolite TMAO drives immune activation and boosts responses to immune checkpoint blockade in pancreatic cancer. *Sci Immunol* **7**: eabn0704. doi:10.1126/sciimmunol.abn0704
- Muellner MK, Uras IZ, Gapp BV, Kerzendorfer C, Smida M, Lechtermann H, Craig-Mueller N, Colinge J, Duernberger G, Nijman SM. 2011. A chemical-genetic screen reveals a mechanism of resistance to PI3K inhibitors in cancer. *Nat Chem Biol* **7**: 787–793. doi:10.1038/nchembio.695
- Nolop KB, Rhodes CG, Brudin LH, Beaney RP, Krausz T, Jones T, Hughes JM. 1987. Glucose utilization in vivo by human pulmonary neoplasms. *Cancer* **60**: 2682–2689. doi:10.1002/1097-0142(19871201)60:11<2682::AID-CNCR2820601118>3.0.CO;2-H
- Onodera J, Ohsumi Y. 2005. Autophagy is required for maintenance of amino acid levels and protein synthesis

- under nitrogen starvation. *J Biol Chem* **280**: 31582–31586. doi:10.1074/jbc.M506736200
- Oshima N, Ishida R, Kishimoto S, Beebe K, Brender JR, Yamamoto K, Urban D, Rai G, Johnson MS, Benavides G, et al. 2020. Dynamic imaging of LDH inhibition in tumors reveals rapid in vivo metabolic rewiring and vulnerability to combination therapy. *Cell Rep* **30**: 1798–1810.e4. doi:10.1016/j.celrep.2020.01.039
- Patra KC, Wang Q, Bhaskar PT, Miller L, Wang Z, Wheaton W, Chandel N, Laakso M, Muller WJ, Allen EL, et al. 2013. Hexokinase 2 is required for tumor initiation and maintenance and its systemic deletion is therapeutic in mouse models of cancer. *Cancer Cell* **24**: 213–228. doi:10.1016/j.ccr.2013.06.014
- Pavlova NN, Zhu J, Thompson CB. 2022. The hallmarks of cancer metabolism: still emerging. *Cell Metab* **34**: 355–377. doi:10.1016/j.cmet.2022.01.007
- Persons DA, Schek N, Hall BL, Finn OJ. 1989. Increased expression of glycolysis-associated genes in oncogene-transformed and growth-accelerated states. *Mol Carcinog* **2**: 88–94. doi:10.1002/mc.2940020207
- Rabinowitz JD, White E. 2010. Autophagy and metabolism. *Science* **330**: 1344–1348. doi:10.1126/science.1193497
- Racker E. 1972. Bioenergetics and the problem of tumor growth. *Am Sci* **60**: 56–63.
- Racker E. 1974. History of the Pasteur effect and its pathobiology. *Mol Cell Biochem* **5**: 17–23. doi:10.1007/BF01874168
- Racker E. 1989. A view of misconduct in science. *Nature* **339**: 91–93. doi:10.1038/339091a0
- Racker E, Spector M. 1981. Warburg effect revisited: merger of biochemistry and molecular biology. *Science* **213**: 303–307. doi:10.1126/science.6264596
- Ralser M. 2018. An appeal to magic? The discovery of a non-enzymatic metabolism and its role in the origins of life. *Biochem J* **475**: 2577–2592. doi:10.1042/BCJ20160866
- Reinfeld BI, Madden MZ, Wolf MM, Chytil A, Bader JE, Patterson AR, Sugiura A, Cohen AS, Ali A, Do BT, et al. 2021. Cell-programmed nutrient partitioning in the tumor microenvironment. *Nature* **593**: 282–288. doi:10.1038/s41586-021-03442-1
- Reynolds MR, Lane AN, Robertson B, Kemp S, Liu Y, Hill BG, Dean DC, Clem BF. 2014. Control of glutamine metabolism by the tumor suppressor Rb. *Oncogene* **33**: 556–566. doi:10.1038/onc.2012.635
- Ron-Harel N, Santos D, Ghergurovich JM, Sage PT, Reddy A, Lovitch SB, Dephonne N, Satterstrom FK, Sheffer M, Spinelli JB, et al. 2016. Mitochondrial biogenesis and proteome remodeling promote one-carbon metabolism for T cell activation. *Cell Metab* **24**: 104–117. doi:10.1016/j.cmet.2016.06.007
- Rous P. 1911. A sarcoma of the fowl transmissible by an agent separable from the tumor cells. *J Exp Med* **13**: 397–411. doi:10.1084/jem.13.4.397
- Samuels Y, Wang Z, Bardelli A, Silliman N, Ptak J, Szabo S, Yan H, Gazdar A, Powell SM, Riggins GJ, et al. 2004. High frequency of mutations of the *PIK3CA* gene in human cancers. *Science* **304**: 554. doi:10.1126/science.1096502
- Sancar A, Van Gelder RN. 2021. Clocks, cancer, and chronochemotherapy. *Science* **371**: eabb0738. doi:10.1126/science.abb0738
- Sciacovelli M, Gonçalves E, Johnson TI, Zecchini VR, da Costa AS, Gaude E, Drubbel AV, Theobald SJ, Abbo SR, Tran MG, et al. 2016. Fumarate is an epigenetic modifier that elicits epithelial-to-mesenchymal transition. *Nature* **537**: 544–547. doi:10.1038/nature19353
- Selak MA, Armour SM, MacKenzie ED, Boulahbel H, Watson DG, Mansfield KD, Pan Y, Simon MC, Thompson CB, Gottlieb E. 2005. Succinate links TCA cycle dysfunction to oncogenesis by inhibiting HIF- α prolyl hydroxylase. *Cancer Cell* **7**: 77–85. doi:10.1016/j.ccr.2004.11.022
- Semenza GL, Roth PH, Fang HM, Wang GL. 1994. Transcriptional regulation of genes encoding glycolytic enzymes by hypoxia-inducible factor 1. *J Biol Chem* **269**: 23757–23763. doi:10.1016/S0021-9258(17)31580-6
- Shim H, Dolde C, Lewis BC, Wu CS, Dang G, Jungmann RA, Dalla-Favera R, Dang CV. 1997. c-Myc transactivation of *LDH-A*: implications for tumor metabolism and growth. *Proc Natl Acad Sci* **94**: 6658–6663. doi:10.1073/pnas.94.13.6658
- Shim H, Chun YS, Lewis BC, Dang CV. 1998. A unique glucose-dependent apoptotic pathway induced by c-Myc. *Proc Natl Acad Sci* **95**: 1511–1516. doi:10.1073/pnas.95.4.1511
- Som P, Atkins HL, Bandyopadhyay D, Fowler JS, MacGregor RR, Matsui K, Oster ZH, Sacker DF, Shiue CY, Turner H, et al. 1980. A fluorinated glucose analog, 2-fluoro-2-deoxy-D-glucose (F-18): nontoxic tracer for rapid tumor detection. *J Nucl Med* **21**: 670–675.
- Spencer CN, McQuade JL, Gopalakrishnan V, McCulloch JA, Vetzou M, Cogdill AP, Khan MAW, Zhang X, White MG, Peterson CB, et al. 2021. Dietary fiber and probiotics influence the gut microbiome and melanoma immunotherapy response. *Science* **374**: 1632–1640. doi:10.1126/science.aaz7015
- Stine ZE, Schug ZT, Salvino JM, Dang CV. 2022. Targeting cancer metabolism in the era of precision oncology. *Nat Rev Drug Discov* **21**: 141–162. doi:10.1038/s41573-021-00339-6
- Tannir NM, Agarwal N, Porta C, Lawrence NJ, Motzer R, McGregor B, Lee RJ, Jain RK, Davis N, Appleman LJ, et al. 2022. Efficacy and safety of telaglenastat plus cabozantinib vs placebo plus cabozantinib in patients with advanced renal cell carcinoma: the CANTATA Randomized Clinical Trial. *JAMA Oncol* **8**: 1411–1418. doi:10.1001/jamaoncol.2022.3511
- Thai M, Graham NA, Braas D, Nehil M, Komisopoulou E, Kurdistani SK, McCormick F, Graeber TG, Christofk HR. 2014. Adenovirus E4ORF1-induced MYC activation promotes host cell anabolic glucose metabolism and virus replication. *Cell Metab* **19**: 694–701. doi:10.1016/j.cmet.2014.03.009
- Tu VY, Ayari A, O'Connor RS. 2021. Beyond the lactate paradox: how lactate and acidity impact T cell therapies against cancer. *Antibodies (Basel)* **10**: 25. doi:10.3390/antib10030025
- Vander Heiden MG, Cantley LC, Thompson CB. 2009. Understanding the Warburg effect: the metabolic requirements of cell proliferation. *Science* **324**: 1029–1033. doi:10.1126/science.1160809
- Varmus HE. 1984. The molecular genetics of cellular oncogenes. *Annu Rev Genet* **18**: 553–612. doi:10.1146/annurev.ge.18.120184.003005

C.V. Dang

- Vasan K, Werner M, Chandel NS. 2020. Mitochondrial metabolism as a target for cancer therapy. *Cell Metab* **32**: 341–352. doi:10.1016/j.cmet.2020.06.019
- Wang GL, Jiang BH, Rue EA, Semenza GL. 1995. Hypoxia-inducible factor 1 is a basic-helix-loop-helix-PAS heterodimer regulated by cellular O₂ tension. *Proc Natl Acad Sci* **92**: 5510–5514. doi:10.1073/pnas.92.12.5510
- Wang R, Dillon CP, Shi LZ, Milasta S, Carter R, Finkelstein D, McCormick LL, Fitzgerald P, Chi H, Munger J, et al. 2011. The transcription factor Myc controls metabolic reprogramming upon T lymphocyte activation. *Immunity* **35**: 871–882. doi:10.1016/j.immuni.2011.09.021
- Wang Z, Roberts AB, Buffa JA, Levison BS, Zhu W, Org E, Gu X, Huang Y, Zamanian-Daryoush M, Culley MK, et al. 2015. Non-lethal inhibition of gut microbial trimethylamine production for the treatment of atherosclerosis. *Cell* **163**: 1585–1595. doi:10.1016/j.cell.2015.11.055
- Wang Y, Stancliffe E, Fowle-Grider R, Wang R, Wang C, Schwaiger-Haber M, Shriver LP, Patti GJ. 2022. Saturation of the mitochondrial NADH shuttles drives aerobic glycolysis in proliferating cells. *Mol Cell* **82**: 3270–3283. e9. doi:10.1016/j.molcel.2022.07.007
- Warburg O. 1925. The metabolism of carcinoma cells. *J Cancer Res* **9**: 148–163. doi:10.1158/jcr.1925.148
- Warburg O. 1928. The chemical constitution of respiration ferment. *Science* **68**: 437–443. doi:10.1126/science.68.1767.437
- Warburg OH. 1930. *The metabolism of tumors*. Constable, London.
- Warburg O. 1956. On the origin of cancer cells. *Science* **123**: 309–314. doi:10.1126/science.123.3191.309
- Warburg O, Wind F, Negelein E. 1927. The metabolism of tumors in the body. *J Gen Physiol* **8**: 519–530. doi:10.1085/jgp.8.6.519
- Weinhouse S. 1956. On respiratory impairment in cancer cells. *Science* **124**: 267–269. doi:10.1126/science.124.3215.267
- Weiss MC, Sousa FL, Mrnjavac N, Neukirchen S, Roettger M, Nelson-Sathi S, Martin WF. 2016. The physiology and habitat of the last universal common ancestor. *Nat Microbiol* **1**: 16116. doi:10.1038/nmicrobiol.2016.116
- Wise DR, DeBerardinis RJ, Mancuso A, Sayed N, Zhang XY, Pfeiffer HK, Nissim I, Daikhin E, Yudkoff M, McMahon SB, et al. 2008. Myc regulates a transcriptional program that stimulates mitochondrial glutaminolysis and leads to glutamine addiction. *Proc Natl Acad Sci* **105**: 18782–18787. doi:10.1073/pnas.0810199105
- Wu R, Racker E. 1959. Regulatory mechanisms in carbohydrate metabolism. III: Limiting factors in glycolysis of ascites tumor cells. *J Biol Chem* **234**: 1029–1035. doi:10.1016/S0021-9258(18)98124-X
- Wu K, Yuan Y, Yu H, Dai X, Wang S, Sun Z, Wang F, Fei H, Lin Q, Jiang H, et al. 2020. The gut microbial metabolite trimethylamine N-oxide aggravates GVHD by inducing M1 macrophage polarization in mice. *Blood* **136**: 501–515. doi:10.1182/blood.2019003990
- Xiang Y, Stine ZE, Xia J, Lu Y, O'Connor RS, Altman BJ, Hsieh AL, Gouw AM, Thomas AG, Gao P, et al. 2015. Targeted inhibition of tumor-specific glutaminase diminishes cell-autonomous tumorigenesis. *J Clin Invest* **125**: 2293–2306. doi:10.1172/JCI75836
- Xu S, Zhou T, Doh HM, Trinh KR, Catapang A, Lee JT, Braas D, Bayley NA, Yamada RE, Vasuthasawat A, et al. 2019. An HK2 antisense oligonucleotide induces synthetic lethality in HK1⁻HK2⁺ multiple myeloma. *Cancer Res* **79**: 2748–2760. doi:10.1158/0008-5472.CAN-18-2799
- Yang L, TeSlaa T, Ng S, Nofal M, Wang L, Lan T, Zeng X, Cowan A, McBride M, Lu W, et al. 2022. Ketogenic diet and chemotherapy combine to disrupt pancreatic cancer metabolism and growth. *Med (N Y)* **3**: 119–136.
- Yap TA, Daver N, Mahendra M, Zhang J, Kamiya-Matsuoka C, Meric-Bernstam F, Kantarjian HM, Ravandi F, Collins ME, Francesco MED, et al. 2023. Complex I inhibitor of oxidative phosphorylation in advanced solid tumors and acute myeloid leukemia: phase I trials. *Nat Med* **29**: 115–126. doi:10.1038/s41591-022-02103-8
- Ying H, Kimmelman AC, Lyssiotis CA, Hua S, Chu GC, Fletcher-Sananikone E, Locasale JW, Son J, Zhang H, Colloff JL, et al. 2012. Oncogenic Kras maintains pancreatic tumors through regulation of anabolic glucose metabolism. *Cell* **149**: 656–670. doi:10.1016/j.cell.2012.01.058
- Yuneva M, Zamboni N, Oefner P, Sachidanandam R, Lazebnik Y. 2007. Deficiency in glutamine but not glucose induces MYC-dependent apoptosis in human cells. *J Cell Biol* **178**: 93–105. doi:10.1083/jcb.200703099
- Yuneva MO, Fan TW, Allen TD, Higashi RM, Ferraris DV, Tsukamoto T, Matés JM, Alonso FJ, Wang C, Seo Y, et al. 2012. The metabolic profile of tumors depends on both the responsible genetic lesion and tissue type. *Cell Metab* **15**: 157–170. doi:10.1016/j.cmet.2011.12.015
- Zhou Y, Petrovic J, Zhao J, Zhang W, Bigdeli A, Zhang Z, Berger SL, Pear WS, Faryabi RB. 2022. EBF1 nuclear repositioning instructs chromatin refolding to promote therapy resistance in T leukemic cells. *Mol Cell* **82**: 1003–1020.e15. doi:10.1016/j.molcel.2022.01.015
- Zindy F, Eischen CM, Randle DH, Kamijo T, Cleveland JL, Sherr CJ, Roussel MF. 1998. Myc signaling via the ARF tumor suppressor regulates p53-dependent apoptosis and immortalization. *Genes Dev* **12**: 2424–2433. doi:10.1101/gad.12.15.2424

Imaging Tumor Metabolism

Thomas Ruan¹ and Kayvan R. Keshari^{1,2,3}

¹Department of Radiology, Memorial Sloan Kettering Cancer Center, New York, New York 10065, USA

²Molecular Pharmacology Program, Memorial Sloan Kettering Cancer Center, New York, New York 10065, USA

³Weill Cornell Graduate School, New York, New York 10065, USA

Correspondence: rahimikk@mskcc.org

Molecular imaging—the mapping of molecular and cellular processes in vivo—has the unique capability to interrogate cancer metabolism in its spatial contexts. This work describes the usage of the two most developed modalities for imaging metabolism in vivo: positron emission tomography (PET) and magnetic resonance (MR). These techniques can be used to probe glycolysis, glutamine metabolism, anabolic metabolism, redox state, hypoxia, and extracellular acidification. This review aims to provide an overview of the strengths and limitations of currently available molecular imaging strategies.

Cancer metabolism is spatially heterogeneous. The metabolic phenotypes involved in tumor progression evolve in response to local environmental drivers such as nutrient availability, perfusion, and hypoxia (Gatenby and Vincent 2003; Pavlova et al. 2022). Tumor metabolism must, therefore, be studied in its native contexts, and molecular imaging—the in vivo visualization of biochemical processes at molecular and cellular levels—is uniquely capable of shedding light on the spatial aspects of cancer metabolism (Rowe and Pomper 2022).

Molecular imaging methods detect metabolism-associated molecules, which are either endogenous or administered via perfusion. These in vivo methods yield insights into spatial heterogeneity, which are inaccessible by ex vivo or nonlocalized measurements. However, heterogeneity of signal can result from technical artifacts as well as the targeted biological processes

themselves. Proper interpretation of imaging data thus requires a clear understanding of signal generation, both in terms of the biochemical mechanisms of probe metabolism and the technical aspects of image formation.

When choosing an imaging method several factors must be considered, including spatial resolution, sensitivity, field of view, temporal resolution, and the potential for clinical translation. This review will describe applications of the two most common molecular imaging modalities: positron emission tomography (PET) and magnetic resonance spectroscopy or imaging (MRS/MRI).

POSITRON EMISSION TOMOGRAPHY (PET)

PET measures positron emission or β^+ decay, a process whereby an unstable radionuclide emits a positron that collides with an electron, creating

γ rays measured by a closed ring of detectors (James and Gambhir 2012). PET does not produce reference images of the body and is typically paired with anatomic imaging by X-ray-computed tomography (CT) or an MRI. In the clinic, PET is typically paired with CT due to its fast scan acquisition and low cost. However, MRI provides superior soft-tissue contrast and reduced radiation exposure, making PET/MRI more appropriate for certain patients (Mayerhoefer et al. 2020). PET offers exceptional sensitivity due to negligible background signal; the lower detection limit is in the picomolar range and nano-to-milligram quantities of tracer molecules are typically delivered. PET also offers high spatial resolution (1–2 mm preclinical, 5–7 mm clinical) and can cover a large field of view, enabling whole-body imaging. Most PET probes, or tracers, are structural analogs of the metabolite they report on, differing only by an appended radioisotope moiety. The most commonly used isotope in PET tracer analogs is ^{18}F due to its long radioactive half-life of ~ 110 min and its structural similarity to a hydroxyl group. Even modest chemical modifications can alter interactions with transporters or enzymes in profound ways. Therefore, it is important to be aware that ^{18}F -functionalized probes do not undergo the same biochemistry as the metabolites they mimic. A different approach to PET probe design is to substitute an atom in the target metabolite with a radioisotope such as ^{11}C or ^{13}N . Substituted PET probes are attractive because they are biochemically identical to the metabolites they report on; however, the short half-lives of ^{11}C (20 min) and ^{13}N (10 min) make the application of these probes challenging (Neumann et al. 2007).

For a PET tracer to successfully inform on tumor metabolism, it must be differentially taken up by or retained within cancer cells over healthy tissue. The degree of differential uptake, or avidity, of a tracer is typically quantified in the clinic by the standardized uptake value (SUV), which is calculated by dividing measured radioactivity in a region of interest by the total activity of the injected dose per volume of the entire body (Thie 2004). Besides static SUV values, more sophisticated information can be obtained by ki-

netic modeling of dynamic PET data. The dynamic PET signal in a region of interest will depend on probe delivery through the blood, described by an input function, and irreversible retention of the probe in cells following a metabolic process (Carson 2003). A typical approach is compartmental modeling, where the PET probe is transported with linear first-order kinetics between compartments such as plasma, extracellular space, and intracellular space. In most cases, the final transfer step into intracellular space can be treated as unidirectional and irreversible. The relevant parameter derived from compartmental modeling is the net influx rate (K_i)—the linear rate of unidirectional probe uptake and trapping where all reversible compartments are in dynamic equilibrium.

Two major drawbacks limit the utility of PET imaging. First, PET tracers generate ionizing radiation, restricting the number of scans that can be safely performed on a single subject. Second, regardless of the radionuclide's chemical environment, positron emission always produces γ rays with identical energy. Thus, PET cannot distinguish between metabolites, and only indirectly measures metabolism as a function of probe uptake and retention.

MAGNETIC RESONANCE SPECTROSCOPY/IMAGING (MRS/MRI)

When atomic nuclei with a nonzero angular momentum quantum number (spin) are placed in a magnetic field, they align either with or against the field. The difference between these states of alignment—that is, their polarization—can be perturbed by radiofrequency excitation pulses, giving rise to a magnetic resonance (MR) signal. The frequency of a given nucleus's MR signal is specific to its local chemical environment. This phenomenon is known as chemical shift and allows the spectroscopic identification of different molecules. Spatially varying gradient magnetic fields allow for the localization of MR signals, producing an image showing signal intensity (magnetic resonance imaging; MRI) or a grid of localized MR spectra (magnetic resonance spectroscopy or spectroscopic imaging; MRS or MRSI). The most used isotopes in MR are ^1H and

^{13}C . Polarization levels for these nuclei at thermal equilibrium are quite low, resulting in poor MR sensitivity of $\sim 10^{-3}$ – 10^{-5} M. The most abundant and MR-sensitive nucleus is ^1H , so MRSI of endogenous ^1H is feasible for measuring metabolite pool sizes in vivo. However, $\sim 99\%$ of naturally occurring carbon is ^{12}C , which has zero spin and is undetectable by MR. MR detection of carbon thus requires the introduction of ^{13}C -enriched molecules in experiments that can be thought of as akin to isotope tracing by mass spectrometry. A conceptually similar experiment to ^{13}C MR tracing is an infusion of molecules labeled with ^2H , a technique called deuterium metabolic imaging (DMI).

The MR signal of ^{13}C -labeled probes can be dramatically magnified by a process termed hyperpolarization (HP) involving prepolarization of nuclei outside the detection magnet. The most common HP method is dissolution dynamic nuclear polarization (dDNP), whereby microwave radiation is used to transfer spin polarization from a free radical electron to ^{13}C nuclei at extremely low temperatures of ~ 1 K. After HP has been sufficiently built up, the frozen sample is rapidly dissolved by a heated buffer for injection (Ardenkjær-Larsen et al. 2003; Golman et al. 2003). More recently, methods coupling solution-state chemistry to separately polarized parahydrogen have been employed to achieve similar HP enhancements without the use of problematically low temperatures (Hövenner et al. 2018; Gierse et al. 2023). In general, HP techniques increase the MR signal by several orders of magnitude, facilitating in vivo spatially resolved isotope tracing. It is important to note that the HP signal enhancement for a given nucleus has an effective lifetime—analogueous to the half-life of radioactive nuclei—mediated by a process called T1 relaxation. Recent work has shown that the T1 time constant can be lengthened by the deuteration of the HP molecule or even the dissolution solvent (Keshari and Wilson 2014; Cho et al. 2018; Deh et al. 2024). However, the most effective strategy for mitigating T1 relaxation is the judicious selection of the ^{13}C enrichment position. Attached hydrogens undergo a dipolar cross-relaxation interaction with ^{13}C , making T1 relaxation efficient. For

this reason, most ^{13}C nuclei used for HP are in a carbonyl group (Keshari and Wilson 2014).

The key benefit of imaging metabolism with HP ^{13}C -enriched molecules is the use of chemical shift to separate signals coming from the injected molecule and its downstream metabolites (Brindle et al. 2011; Wang et al. 2019). For this to be possible, the chemical shifts of the probe molecule and its metabolic products must be sufficiently far apart for spectral resolution. MR experiments produce data in the form of signal intensities that are not inherently quantitative, so results are typically reported in ratios of metabolite-to-probe intensities. More sophisticated analyses fit HP MR data as a compartmental system, yielding kinetic rate constants with units of inverse seconds (Harrison et al. 2012; Bankson et al. 2015; Crane et al. 2021).

METABOLIC TARGETS

Glycolysis

The reprogramming of energy metabolism in cancer is an especially attractive target for molecular imaging due to its role as an integral requirement for cellular proliferation (Hanahan and Weinberg 2011). It should, therefore, come as no surprise that several of the most studied metabolic imaging strategies focus on the central feature of cancer energy metabolism: elevated glycolysis, also known as the Warburg effect (Fig. 1A; Warburg 1956).

Glucose

The paradigmatic success story of molecular imaging is perhaps [^{18}F]fluorodeoxyglucose (FDG) (Fig. 1Bi). PET of FDG is frequently used in the clinic to diagnose, stage, and monitor a range of cancers, with millions of scans performed in the United States every year (Alavi et al. 2004; Kelloff et al. 2005; Czernin et al. 2013; Rosenkrantz et al. 2016). FDG is an analog of glucose with ^{18}F substituted for the C2 hydroxyl group (Ido et al. 1978). FDG is readily imported into cells by the glucose transporters (GLUTs) and undergoes the reversible first step of glycolysis, phosphorylation of the C6 hydroxyl. However, fur-

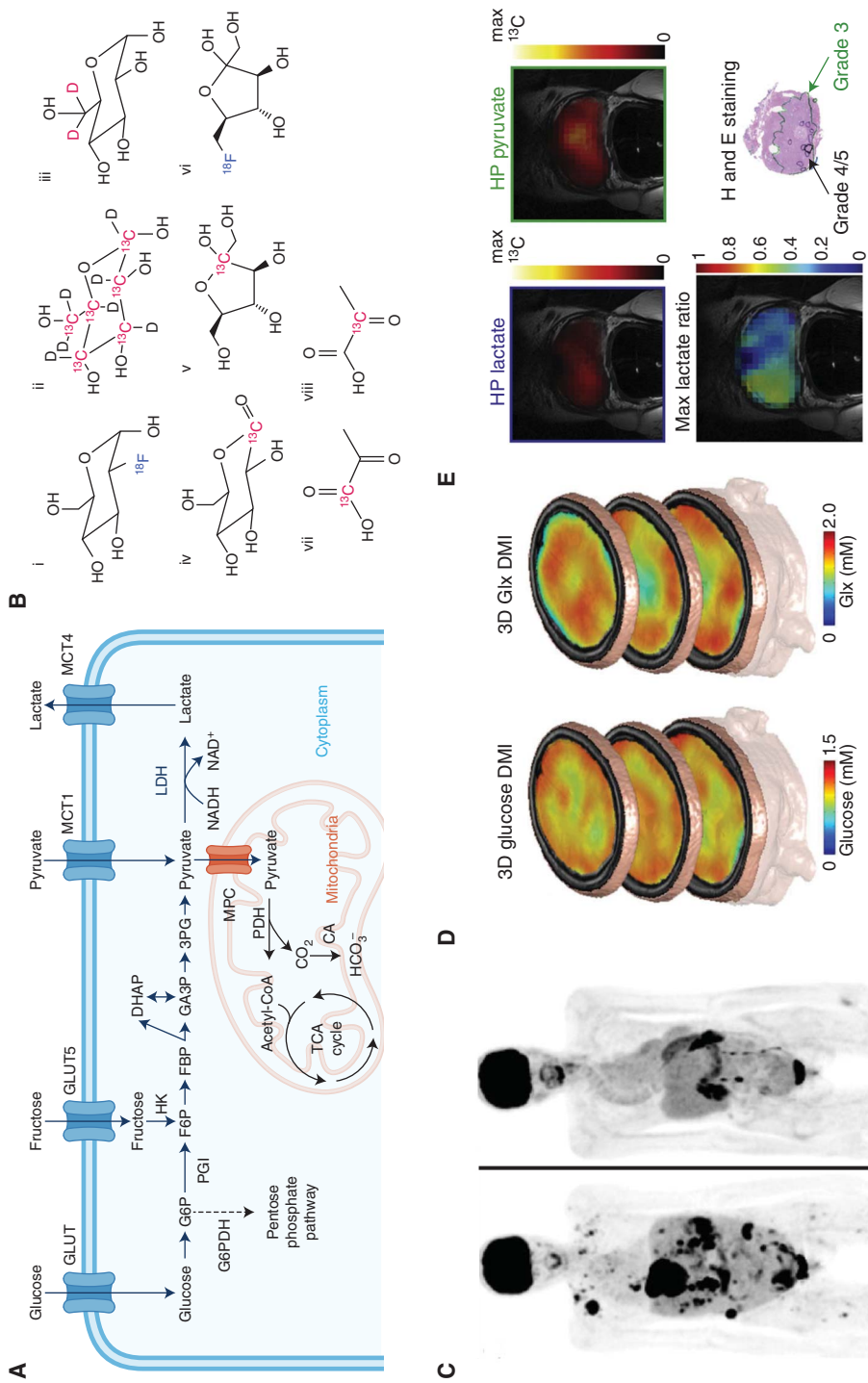


Figure 1. (See following page for legend.)

ther metabolism of FDG-6-phosphate through canonical glycolysis via phosphoglucose isomerase (PGI) is not possible due to the fluorine on C2. Since FDG-6-phosphate must be dephosphorylated before it can be effluxed, radioactivity in the cell is trapped in a dynamic equilibrium of uptake by GLUT, phosphorylation, and dephosphorylation (Gallagher et al. 1978). Thus, FDG-PET indirectly reports on the proximal aspects of glycolysis.

FDG is avidly taken up by any cells that consume large amounts of glucose, so FDG-PET is problematic for imaging tumors in the brain, which has high baseline levels of glycolysis (Fig. 1C). In other areas of the body, nonmalignant sources of accumulation can complicate FDG-PET imaging (Long and Smith 2011). Inflammation, for example, is a cause of nonspecific signals since activated inflammatory cells require high levels of glycolysis to function (Skoura et al. 2016). Knowledge of the underlying biochemical mechanism can help overcome this potential issue. Inflammatory cells also express high levels of glucose-6-phosphatase, the enzyme that dephosphorylates FDG-6-phos-

phate, and thus efflux radioactivity faster than tumor cells. As such, imaging at two time points can help differentiate between tumors and inflammation—while tumor and inflammatory cells will both show high SUV at an early time point, only tumor cells will retain the PET probe over a long time course (Alavi et al. 2004; Long and Smith 2011).

Historically, FDG-PET has not been used for imaging of prostate cancers, which tend to exhibit a modest Warburg effect. However, some evidence suggests that advanced prostate cancers that have become castration-resistant are amenable to FDG-PET as a result of dramatically increased glucose uptake (Jadvar 2016). Although FDG uptake is classically interpreted as a readout of glycolytic activity, there is some recent evidence suggesting that FDG uptake can also depend on flux through the pentose phosphate pathway (PPP) (Sambuceti et al. 2021). Silencing of hexose-6-phosphate dehydrogenase, the enzyme that catalyzes entry into the PPP in the endoplasmic reticulum, in mouse cell culture models of colon and breast cancer resulted in decreased FDG uptake despite in-

Figure 1. Molecular imaging of glycolysis. (A) Diagram of metabolites, enzymes, and transporters relevant to glycolysis. (G6P) Glucose-6-phosphate, (F6P) fructose-6-phosphate, (FBP) fructose-1,6-biphosphate, (GA3P) glyceraldehyde 3-phosphate, (DHAP) dihydroxyacetone phosphate, (3PG) 3-phosphoglycerate, (NAD⁺/NADH) oxidized/reduced nicotinamide adenine dinucleotide, (CO₂) carbon dioxide, (HCO₃⁻) bicarbonate, (acetyl-CoA) acetyl coenzyme A, (G6PDH) glucose-6-phosphate dehydrogenase, (PGI) phosphoglucose isomerase, (HK) hexokinase, (LDH) lactate dehydrogenase, (PDH) pyruvate dehydrogenase, (CA) carbonic anhydrase, (GLUT) glucose transporter, (MCT1/4) monocarboxylate transporter, (MPC) mitochondrial pyruvate carrier. (A created with BioRender.com.) (B) Chemical structures of probes for imaging glycolysis. (i) [¹⁸F]fluorodeoxyglucose (FDG), (ii) [1,2,3,4,5,6,6'-²H₇, U-¹³C₆]-glucose, (iii) [6,6'-²H₂]glucose, (iv) δ-[1-¹³C]gluconolactone, (v) [2-¹³C]fructose, (vi) 6-deoxy-6-[¹⁸F]fluoro-D-fructose (6-[¹⁸F]FDF), (vii) [1-¹³C]pyruvate, (viii) [2-¹³C]pyruvate. β-Emitting radioisotopes detected by positron emission tomograph (PET) are blue, and nuclei detected by magnetic resonance (MR) are red. (Structures created with ChemDraw). (C) PET-FDG maximum intensity projection images of patients with metastatic melanoma before (*left*) and after (*right*) BRAF inhibitor treatment. This image highlights the capability of PET to image metastasis over the whole body, and nonspecific FDG uptake in the brain and urinary system. (C reprinted from Czernin et al. 2013 under the terms of the Creative Commons Attribution License.) (D) Deuterium metabolic imaging (DMI) of orally administered [6,6'-²H₂]glucose in brains of healthy humans. 3D maps of glucose (*left*) and glutamine/glutamate (Glx; *right*) show modestly heterogeneous delivery of deuterium-labeled substrate and conversion to Glx, with slightly lower Glx signal in the gray matter-rich ventricles. (D reprinted from De Feyter et al. 2018 under the terms of the Creative Commons Attribution-NonCommercial License.) (E) Hyperpolarization (HP) [1-¹³C]pyruvate imaging of a prostate cancer patient. Data from an HP experiment can be represented in metabolite maps of lactate (*top left*), pyruvate (*top right*), or the ratio of product to substrate (*bottom left*). Color maps of signal intensity are overlaid on ¹H T2-weighted magnetic resonance imaging (MRI) images for anatomical reference. The lactate-to-pyruvate ratio is elevated in the *left* region of the prostate, corresponding to regions of higher Gleason grade in matched histology sections (*bottom right*). (E reprinted from Granlund et al. 2019, Elsevier © 2016.)

T. Ruan and K.R. Keshari

creases in glycolytic flux and lactate secretion (Marini et al. 2016). In this context, FDG-PET may report on NADPH generation through the PPP, which is up-regulated in proliferative cancers. In all, although FDG-PET has become a workhorse clinical imaging modality, its lack of specificity has limited its effectiveness in basic research.

Other glucose-based PET probes have also been reported, although with limited application to imaging cancer metabolism. For example, PET of ^{11}C -labeled glucose has been used for PET imaging in brain cancer patients (Ericson et al. 1985; Spence et al. 1998). However, this probe is chemically identical to endogenous glucose and is not trapped in tumors like FDG. There have also been attempts to produce PET probes based on other sugars, such as 6-deoxy-6- ^{18}F fluoro-D-fructose (6- ^{18}F FDF), a radio analog of fructose (Fig. 1Bvi; Wuest et al. 2011). 6- ^{18}F FDF is trapped in tumor cells by a similar mechanism to FDG, and has been used to image breast cancers that up-regulate the fructose transporter GLUT5 (Bouvet et al. 2014). In one comparative study, 6- ^{18}F FDF uptake was shown to be more specific for breast cancers than FDG, indicating a potential clinical role for the imaging of sugars other than glucose (Wuest et al. 2017).

Elevated glucose uptake can be imaged directly with an MRI of HP uniformly ^{13}C -labeled glucose (Fig. 1Bii). The primary benefit of this approach is that it directly quantifies glucose metabolism in addition to uptake. An early demonstration of this technique on T47D cells in an NMR-compatible bioreactor system showed that lactate, and smaller amounts of dihydroxyacetone phosphate (DHAP) and 3-phosphoglyceric acid (3PG), can be detected from HP glucose (Harris et al. 2013). While imaging of mice implanted with EL4 and LL2 tumors detected HP glucose in tumors and organs such as the brain, heart, and kidney, only tumors produced HP lactate and, to a lesser extent, HP DHAP, bicarbonate, and 6-phosphogluconic acid (6PG) (Rodrigues et al. 2014). These latter two metabolites report on the shunting of glucose-6-phosphate to the PPP, demonstrating the ability of HP MR to simultaneously quantify multiple

pathways. Another study linked the production of 6PG from HP glucose to the expression of telomerase reverse transcriptase, which up-regulates GLUT1 and glucose-6-phosphate dehydrogenase, in low-grade oligodendrogliomas (Viswanath et al. 2021a). MRS of HP glucose in glioblastoma models showed increased lactate production in a cell culture-based model, which produced a compact tumor, over a patient-derived model with an infiltrative phenotype (Mishkovsky et al. 2021). The biggest disadvantage of HP glucose is its short HP lifetime. Uniformly ^{13}C -labeled HP glucose has a T1 of only a few seconds, which is too short for in vivo detection of metabolism. Although synthetic strategies such as selective ^{13}C labeling or perdeuteration can help raise the T1 of glucose to ~ 10 sec (Mishkovsky et al. 2017), the fast HP decay of this probe still limits the achievable detection window.

A thermal (nonhyperpolarized) MR-based technique that targets glycolysis is glucose chemical exchange saturation transfer (glucoCEST). This method operates by saturating the MR signal of glucose hydroxyl hydrogens with a selective radiofrequency pulse. The exchange of the saturated nuclei with water hydrogens causes a decrease in the water ^1H MR signal. The extent of this attenuation correlates with the concentration of glucose, providing a method to sensitively measure local glucose concentrations. The median intensity and spatial distribution of the glucoCEST signal in xenograft tumors of two models of colorectal cancer (LS174T and SW1222) correlates with FDG-PET (Walker-Samuel et al. 2013). However, there was no significant correlation between glucoCEST uptake and perfusion, as measured by the common MRI contrast agent Gd-DTPA. These findings indicate that glucoCEST specifically reports on glucose uptake rather than perfusion of the delivered bolus. GlucoCEST is analogous to FDG-PET in that it measures glucose uptake, not subsequent metabolism. However, glucoCEST does not require the synthesis of a radiotracer, does not use ionizing radiation, and has a much higher spatial resolution than FDG-PET. Additionally, there may be contexts where glucoCEST is more sensitive to changes

in glucose uptake than FDG-PET. For example, the metabolic response to doxorubicin treatment in mice implanted with 4T1 tumors was detected by glucoCEST but not FDG-PET (Cappozza et al. 2022). The initial work of implementing glucoCEST in the clinic is underway (Xu et al. 2015; Bender et al. 2022), but this is still a nascent technology; for glucoCEST to supplant FDG-PET issues such as low sensitivity, susceptibility to subject motion, and full elucidation of signal compartmentalization must be addressed (Kim et al. 2022).

DMI is another MR-based technique for imaging glucose metabolism that has been gaining interest recently. The advantages of imaging deuterium-labeled molecules include experimental simplicity, high sensitivity, and low background noise (De Feyter and de Graaf 2021). A landmark study used DMI of [6,6'-²H₂]glucose in rat and human brains to generate steady-state metabolic maps of glucose, lactate, and glutamine + glutamate (Glx; the signals from these similar metabolites overlap in the ²H spectrum) (Fig. 1Biii; De Feyter et al. 2018). The ratio of lactate to Glx was higher in tumors, reflecting the Warburg phenotype of imbalance toward reductive metabolism of glucose (Fig. 1D). DMI has also been used to measure dynamic fluxes of glucose metabolism in mouse xenografts (Kreis et al. 2019; Markovic et al. 2021). While promising, this approach is hampered by long scan times and low spatial resolution associated with the poor MR sensitivity of deuterium. One promising solution to this problem measures decreases in the ¹H signals of glycolytic metabolites following administration of ²H-labeled glucose to indirectly quantify ²H enrichment (Rich et al. 2020). This method, described by its authors as “quantitative exchanged-label turnover MRS,” may provide an easier path to clinical implementation for deuterium tracing experiments (Cember et al. 2022).

Besides imaging uptake and metabolism of glucose directly, other inputs and outputs of the glycolytic pathway have been investigated as molecular imaging targets. HP [2-¹³C]fructose has been used to image the generation of fructose-6-phosphate in models of prostate cancer (Keshari et al. 2009) and fructose-1-phosphate

in hepatocellular carcinoma models (Fig. 1Bv; Tee et al. 2022). HP δ-[1-¹³C]gluconolactone was developed as a probe of the oxidative portion of the PPP (Fig. 1Biv). In orthotopic models of glioblastoma in rats, the flux of HP δ-[1-¹³C]gluconolactone to HP [¹³C]bicarbonate was higher in tumor tissue than contralateral or tumor-free control brains, and decreased in tumors upon silencing of TERT signaling (Batsios et al. 2021; Minami et al. 2023). There has also been some work on developing HP [2-¹³C]dihydroxyacetone as a probe for gluconeogenesis, which enters glycolysis after phosphorylation to DHAP, although it has not yet been applied in the context of cancer metabolism (Moreno et al. 2017; Marco-Rius et al. 2021; Ragavan et al. 2021).

Lactate

Another popular target of molecular imaging is lactate, the predominant final product of glycolysis in tumors. This is due to its abundance and the ability to target it via a wide range of approaches. Historically, ¹H MRSI has been used in the clinic to measure lactate pool size, especially in brain cancers (Öz et al. 2014). Cross-validation studies show that higher-grade gliomas that exhibit high FDG-PET avidity also produce large amounts of lactate (Herholz et al. 1992). PET of [3-¹¹C]lactate has been used to measure lactate utilization in the healthy heart and brain (Herrero et al. 2007; Temma et al. 2018). This probe could be useful in studying cancers that have been shown to use lactate as a fuel source for the TCA cycle (Faubert et al. 2017).

HP pyruvate has been extensively investigated as a probe for lactate generation. [1-¹³C] pyruvate can build up high levels of polarization, has a long T1 (>60 sec), and is predominantly reduced to [1-¹³C]lactate (chemical shift difference of ~12 ppm) via the lactate dehydrogenase complex (LDH) in tumor cells (Fig. 1Bvii; Albers et al. 2008; Keshari and Wilson 2014). HP pyruvate-to-lactate flux has been identified in a wide range of preclinical contexts as a biomarker of cancer metabolism, progression, and treatment response (Golman et al. 2006; Day et al. 2007; Albers et al. 2008; Hu et al. 2010, 2011; Park et al. 2010, 2012; Keshari et al. 2013; Serrao et al. 2016;

Dong et al. 2018; Grashei et al. 2022). [$1\text{-}^{13}\text{C}$] Pyruvate is the first HP probe to be translated to the clinic (Kurhanewicz et al. 2019), with applications to patients with prostate cancer (Fig. 1E; Nelson et al. 2013; Aggarwal et al. 2017; Chen et al. 2020; Granlund et al. 2020; de Kouchkovsky et al. 2022), renal carcinomas (Tran et al. 2019; Tang et al. 2021; Ursprung et al. 2022), breast cancer (Gallagher et al. 2020; Woitek et al. 2020), brain cancer (Miloushev et al. 2018; Park et al. 2018; Zaccagna et al. 2022), and pancreatic cancer (Stødtkilde-Jørgensen et al. 2020).

Elevated HP pyruvate-to-lactate flux is typically interpreted as a consequence of the Warburg effect. However, some evidence suggests that other factors also control the kinetics of HP pyruvate metabolism. Studies that correlate HP lactate generation with HP perfusion imaging (Lau et al. 2016) or mass spectrometry imaging of nonhyperf polarized ^{13}C -labeled pyruvate (Fala et al. 2021) indicate that one of the main determinants for increased HP pyruvate-to-lactate flux in tumors is the delivery of HP pyruvate. Additionally, pharmacological blockade of VEGF signaling, which decreases tumor vascularization, decreases HP pyruvate-to-lactate flux despite increases in LDH activity and lactate pool size (Bohndiek et al. 2012; Park et al. 2016). Elevated HP lactate formation also correlates with the expression of the pyruvate importer monocarboxylate transporter 1 (MCT1) in a variety of preclinical (Keshari et al. 2013; Xu et al. 2014; Sushentsev et al. 2022) and clinical contexts (Granlund et al. 2019; Gallagher et al. 2020). Overexpression of MCT1 in pancreatic carcinoma cells causes a marked increase in HP pyruvate-to-lactate flux, suggesting a possible rate-limiting role of membrane transport (Rao et al. 2020). Finally, pharmacological inhibition of LDH (Dutta et al. 2013; Varma et al. 2021) or indirect down-regulation of LDH through inhibition of upstream signaling (Dafni et al. 2010; Ward et al. 2010) dramatically ablates flux to lactate. Interestingly, there is some evidence that blocking off pyruvate reduction to lactate can result in compensatory increases in the utilization of other pathways, such as entry into the TCA cycle via pyruvate dehydrogenase (PDH) (Oshima et al. 2020). Overall, further work is required to clarify

the precise mechanisms influencing the kinetics of HP pyruvate metabolism.

HP [$1\text{-}^{13}\text{C}$]pyruvate readily reports on flux to lactate, but entry into the TCA cycle via PDH involves decarboxylation at the 1C position, forming [^{13}C]carbon dioxide that rapidly equilibrates to [^{13}C]bicarbonate via carbonic anhydrase (CA). Although [^{13}C]bicarbonate levels can be used as a proxy of pyruvate-derived carbon entry into the TCA cycle, the particulars of TCA cycle flux are functionally invisible to [$1\text{-}^{13}\text{C}$]pyruvate. To this end, HP [$2\text{-}^{13}\text{C}$]pyruvate (Fig. 1Bviii) has been investigated as a probe of TCA cycle flux in the production of glutamate, citrate, and acetylcarnitine (Schroeder et al. 2009; Marjańska et al. 2010; Park et al. 2013; Izquierdo-Garcia et al. 2015). Glutamate levels are responsive to pharmacological manipulation of pyruvate entry into the TCA cycle. Treatment with dichloroacetate, which indirectly activates PDH activity by inhibiting PDH kinase, increased HP glutamate formation in healthy rat brains (Park et al. 2013), whereas IDH1 mutant glioblastoma cells displayed a decrease in HP [$5\text{-}^{13}\text{C}$]glutamate generation concomitant with down-regulation of PDH expression (Izquierdo-Garcia et al. 2015). A pilot study on the clinical translation of HP [$2\text{-}^{13}\text{C}$]pyruvate in healthy brains of volunteers demonstrated that HP [$2\text{-}^{13}\text{C}$]pyruvate converted to lactate at a similar rate as [$1\text{-}^{13}\text{C}$]pyruvate (Chung et al. 2019). The full potential of [$2\text{-}^{13}\text{C}$]pyruvate has not yet been fully realized. Copolarization and injection of mixed [$1\text{-}^{13}\text{C}$]pyruvate and [$2\text{-}^{13}\text{C}$]pyruvate could allow simultaneous detection of the reductive and oxidative fates of pyruvate, expanding informational in a kind of multiplexing approach (Wilson et al. 2010; DeBerardinis and Keshari 2022). Another strategy is to use doubly labeled [$1,2\text{-}^{13}\text{C}_2$]pyruvate (Chen et al. 2012; Sriram et al. 2015), which can directly measure rates of key metabolic pathways in competition with each other.

In conclusion, glycolysis has presented ample targets for molecular imaging of cancer metabolism. FDG-PET and HP [$1\text{-}^{13}\text{C}$]pyruvate are the most used probes of their respective modalities, and several MR methods for the detection of glycolysis are in development.

Glutamine

Glutaminolysis

The second most attractive molecular imaging target for cancer after glucose is glutamine, which participates in several key tumor metabolic processes (Fig. 2A). Glutamine is involved in up-regulated proliferation through the biosynthesis of nucleotides or hexosamines and, via glutamate, can supply carbon to the TCA cycle for energy generation, amino acid synthesis, or reductive carboxylation (DeBerardinis and Cheng 2010; Altman et al. 2016). Early PET studies reported increased ^{13}N - or ^{11}C -labeled glutamine uptake in murine and canine tumor models, although the short half-lives of these radioisotopes (~ 10 and 20 min, respectively) limited detailed investigation (Gelbard et al. 1977; Qu et al. 2012).

Several fluorine-based analog probes have also been reported. ^{18}F -(2*S*,4*R*)-4-fluoroglutamine (Fig. 2Biii) is the most used molecule because it resembles endogenous L-glutamine and shows differential uptake in xenograft models of glutamine-addicted gliomas and breast cancers (Lieberman et al. 2011; Qu et al. 2011; Liu et al. 2018). ^{18}F -glutamine has also been shown to accumulate in human patient tumors (Liu et al. 2018; Grkovski et al. 2020). A glutamine-based PET probe is especially useful for the clinical imaging of gliomas, where nonspecific uptake of glucose by the healthy brain makes conventional FDG-PET difficult (Fig. 2C; Venneti et al. 2015).

The mechanism by which tumor cells retain ^{18}F -glutamine has not been fully elucidated. Isolated rat kidney GLS1, the main isotype of glutaminase in tumors, can metabolize 4-fluoroglutamine to 4-fluoroglutamate in vitro (Cooper et al. 2012). However, a comparison of ^{18}F -glutamine and ^{18}F -glutamate showed uptake of both probes but long-term retention of ^{18}F -glutamine and rapid washout of ^{18}F -glutamate (Ploessl et al. 2012). This finding seems to suggest that although ^{18}F -glutamine is avidly taken up by tumor cells that up-regulate the neutral amino acid transporter ASCT2, the probe is not converted to glutamate. Inhibition of GLS in xenografts of triple-negative breast cancers that have high GLS expression results in in-

creased ^{18}F -glutamine uptake, indicating that fluoroglutamine PET signal is sensitive to the intracellular pool size of glutamine (Zhou et al. 2017; Viswanath et al. 2021b).

Hyperpolarized glutamine has also been investigated as a probe for glutaminolysis. The C1 and C5 carbons of L-glutamine do not have directly bonded hydrogens and are ideal candidates for ^{13}C enrichment, with T1 values of 25 and 16 sec, respectively (Gallagher et al. 2008; Jensen et al. 2009). Unfortunately, the chemical shift difference between [1- ^{13}C]glutamine and [1- ^{13}C]glutamate is only 0.5 ppm, which is too small to feasibly separate. Conversely, HP [5- ^{13}C]glutamine is a viable probe for glutaminolysis, with a favorable chemical shift difference between it and [5- ^{13}C]glutamate of ~ 3.4 ppm. Early in vitro experiments with HP [5- ^{13}C]glutamine in suspensions of glutamine-addicted tumor cells showed ready uptake and conversion to [5- ^{13}C]glutamate (Gallagher et al. 2008b; Qu et al. 2011; Canapè et al. 2015). Experiments in rat liver tumor (Cabella et al. 2013) and mouse pancreatic ductal adenocarcinoma models (Eskandari et al. 2022) show that HP [5- ^{13}C]glutamine is taken up and converted to [5- ^{13}C]glutamate by tumors (Fig. 2D). Additionally, the T1 relaxation time of [5- ^{13}C]glutamine can be extended by deuteration of the C4 carbon and replacement of the amide nitrogen with ^{15}N (Fig. 2Bi; Qu et al. 2011; Eskandari et al. 2022). While the comparatively shorter HP lifetime of HP [5- ^{13}C]glutamine presents a challenge for clinical translation, isotope enrichment, and further modifications may make this probe useful for the in vivo characterization and development of next-generation glutaminase inhibitor drugs. Another avenue of exploration is HP-substituted ^{15}N -labeled glutamine analogs, which are well tolerated in vivo and show remarkably long T1s of 2.5–5 min (Chiavazza et al. 2013; Durst et al. 2016). However, the applicability of these probes to metabolic studies remains to be shown.

2-Hydroxyglutarate

Increased glutamine uptake is also seen in cancers with mutations in isocitrate dehydrogenase 1/2 (IDH1/2) that confer a gain-of-function phe-

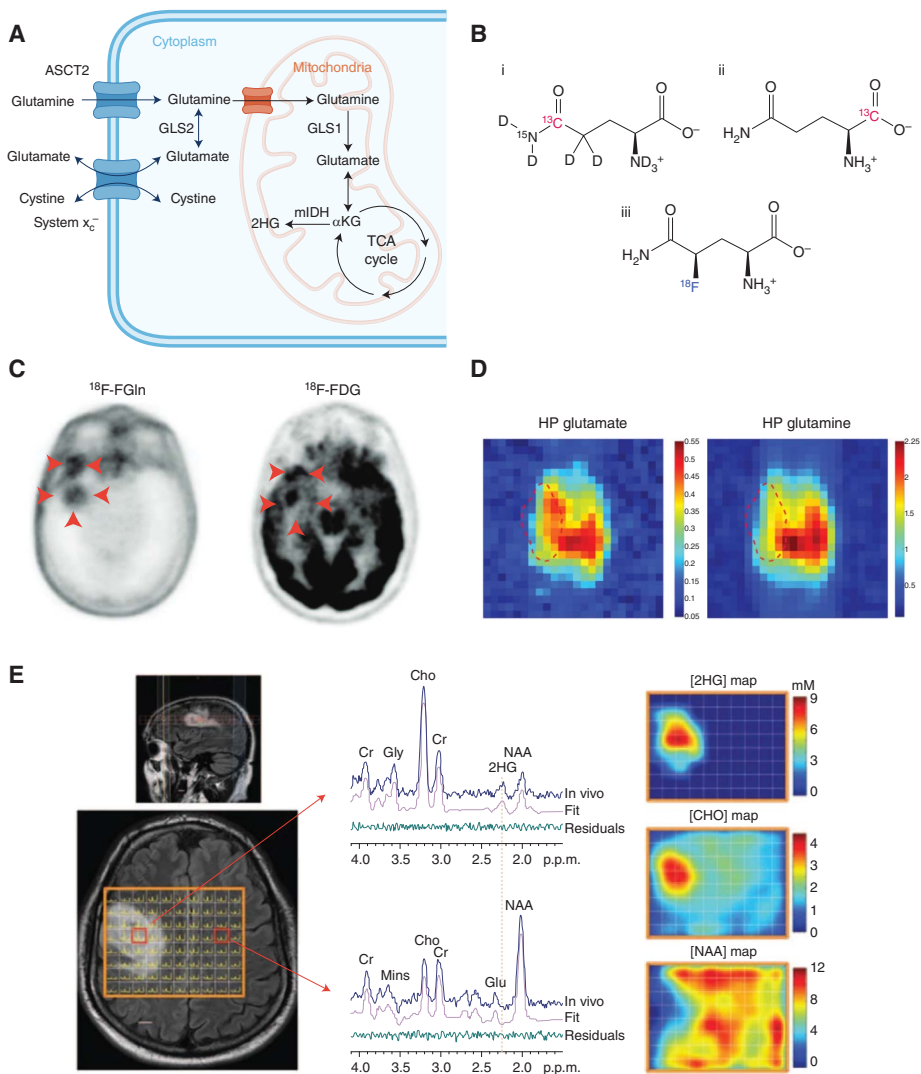


Figure 2. Molecular imaging of glutamine metabolism. (A) Diagram of metabolites, enzymes, and transporters relevant to glutamine metabolism. (α KG) α -ketoglutarate, (2HG) 2-hydroxyglutarate, (GLS1/2) glutaminase, (mIDH) mutant isocitrate dehydrogenase, (ASCT2) alanine–serine–cystine transporter 2. (A created with BioRender.com.) (B) Chemical structures of probes for imaging glutamine metabolism. (i) $[5-^{13}\text{C}, 4,4-^2\text{H}_2, 5-^{15}\text{N}]$ glutamine, (ii) $[1-^{13}\text{C}]$ glutamine, (iii) ^{18}F -(2S,4R)-4-fluoroglutamine. β -Emitting radioisotopes detected by positron emission tomography (PET) are blue, and nuclei detected by magnetic resonance (MR) are red. Structures created with ChemDraw. (C) ^{18}F -glutamine PET imaging of a glioblastoma patient (left) shows specific uptake in the tumor (red arrows) with minimal signal from the surrounding brain, whereas FDG-PET imaging of the same patient (right) shows indiscriminate uptake throughout the brain. (C reprinted from Venneti et al. 2015, The American Association for the Advancement of Science © 2015.) (D) Imaging of hyperpolarization (HP) $[5-^{13}\text{C}]$ glutamine in a MIA PaCa-2 xenograft mouse model shows elevated glutaminolysis in tumor. Metabolic maps of HP glutamate (left) and HP glutamine (right) with tumor region indicated with red dotted line show decreased uptake of HP glutamine but similar HP glutamate production in tumor compared to surrounding tissue. (D reprinted from Eskandari et al. 2022 under the terms of Creative Commons Attribution-NonCommercial-NoDerivatives Licences 4.0 [CC BY-NC-ND].) (E) Clinical ^1H MRSI shows high 2HG production in mutant IDH2 glioma. 3D metabolic maps of 2HG (left), glutamine/glutamate (center), and lactate (right) show that regions of with high levels of 2HG correlate with high lactate production, but not glutamine/glutamate levels, which are relatively homogeneous throughout the imaging field of view. (E reprinted from Choi et al. 2012, Springer Link © 2012.)

notype where α -ketoglutarate (α KG) is converted to 2-hydroxyglutarate (2HG). Elevated 2HG production has been characterized as a central feature of metabolic reprogramming in a variety of cancers and is being investigated as a target for molecular imaging (Dang et al. 2009; Ježek 2020). ^1H MRSI measurement of 2HG pool size in glioma patients consistently shows that IDH mutant gliomas, but not healthy tissue or IDH wild-type tumors, produce large quantities of 2HG (Fig. 2E; Choi et al. 2012; Andronesi et al. 2016; An et al. 2017, 2018). In this way, 2HG can be thought of as an imaging biomarker of IDH mutation status.

In this vein, HP [$1\text{-}^{13}\text{C}$]glutamine (Fig. 2Bii) has been leveraged to image flux to 2HG in mouse xenografts of mutant IDH patient-derived chondrosarcoma cells (Salamanca-Cardona et al. 2017). Using ^{13}C mass spectrometry tracing experiments, this paper demonstrated that glutamine, not glucose, is the primary carbon source for 2HG. HP [$1\text{-}^{13}\text{C}$] α KG has also been used to measure 2HG formation in IDH mutant tumor cells and mouse models (Chaumeil et al. 2013; Miura et al. 2021). Targeting flux to 2HG may prove useful in the context of mutant IDH1 gliomas, which appear unsuitable for imaging with HP pyruvate (Chaumeil et al. 2016). Low cell permeability of α KG has hampered HP imaging capability, although chemical modifications such as esterification may help with this issue (Zacharias et al. 2012; AbuSalim et al. 2021; Singh et al. 2021).

Anabolism

Cancer cells also up-regulate pathways of anabolic metabolism to fuel unrestrained proliferation (Fig. 3A). This section presents examples of imaging probes that report on fatty acid, protein, and nucleoside salvage.

Fatty Acid Synthesis

Rapid tumor cell division is accompanied by high levels of de novo fatty acid biosynthesis, a pathway that produces the lipid bilayers that make up cell membranes. One of the building blocks of fatty acids is acetyl-CoA, which is synthesized from acetate. To that end, PET of

[^{11}C]acetate has been used as a strategy to image fatty acid synthesis in cancers (Fig. 3Bi). In the clinic, [^{11}C]acetate PET has been useful in imaging tumors that are not FDG avid such as prostate cancer, well-differentiated hepatocarcinoma, and multiple myelomas (Grassi et al. 2011; Chen et al. 2021). Uptake of [^{11}C]acetate is sensitive to inhibition of fatty acid synthase (FAS) in prostate cancer cells, indicating that [^{11}C]acetate could act as an imaging biomarker of fatty acid synthesis (Vävere et al. 2008; Lewis et al. 2014). The first step of acetate metabolism is conversion to acetyl-CoA via acetyl-CoA synthetase (ACSS). ACSS1, the mitochondrial isoform of ACSS, is predominant in normal cells, and is used as an entry point for acetate into the TCA cycle. Tumor cells have low ACSS1 expression and instead up-regulate the cytosolic isoform ACSS2, diverting acetate incorporation into fatty acid synthesis (Yoshii et al. 2009). There has not been much success in developing ^{18}F -based acetate analogs as PET probes. Fluoroacetate is toxic at high doses and is used as a pesticide (Clarke 1991). Although ^{18}F -fluoroacetate is safe at low PET dosage concentration in nonhuman primates (Nishii et al. 2012), a study in healthy large animals showed that ^{18}F -fluoroacetate is mostly excreted through the blood and shows no specific uptake (Lindhe et al. 2009).

Acetate uptake has also been imaged with MR-based probes. DMI of infused ^2H -labeled acetate showed increased acetate uptake and reduced glutamate and glutamine labeling in tumors compared to healthy brain tissue in orthotopic models of glioma in rats, indicating reduced TCA cycle utilization by tumor cells (De Feyter et al. 2018). HP [$1\text{-}^{13}\text{C}$]acetate has also been used to measure TCA cycle flux in healthy rat hearts and kidneys, but this probe has yet to be applied to the context of cancer metabolism (Bastiaansen et al. 2015; Mikkelsen et al. 2017).

Amino Acid Uptake

Proliferative cancers display increased uptake of neutrally charged amino acids to fuel protein synthesis. The blood–brain barrier is permeable to neutrally charged amino acids, which are imported into cells by the L-type amino acid trans-

T. Ruan and K.R. Keshari

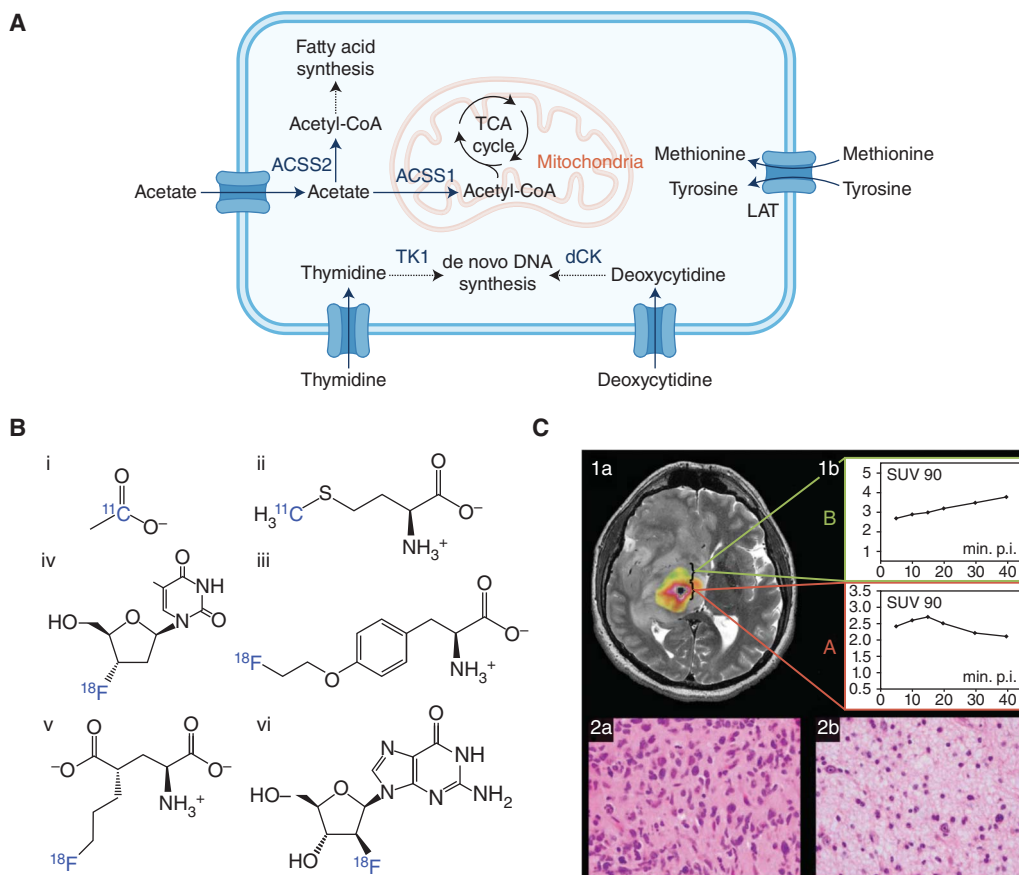


Figure 3. Molecular imaging of anabolic metabolism. (A) Diagram of metabolites, enzymes, and transporters relevant to anabolic metabolism. (ACSS1/2) acetyl-CoA synthase, (TK1) thymidine kinase, (dCK) deoxycytidine kinase, (LAT) large neutral amino acid transporter. (A created with BioRender.com.) (B) Chemical structures of probes for imaging glutamine metabolism. (i) $[^{11}\text{C}]$ acetate, (ii) $[^{11}\text{C}]$ -methyl-L-methionine (^{11}C -MET), (iii) O-(2- $[^{18}\text{F}]$ fluoroethyl)-L-tyrosine (^{18}F FET), (iv) (S)-4-(3- $[^{18}\text{F}]$ fluoropropyl)-L-glutamate ($[^{18}\text{F}]$ FSPG), (v) $[^{18}\text{F}]$ 3'-deoxy-3'-fluorothymidine ($[^{18}\text{F}]$ FLT), (vi) $[^{18}\text{F}]$ clofarabine ($[^{18}\text{F}]$ CFA). β -Emitting radioisotopes detected by positron emission tomography (PET) are blue, and nuclei detected by magnetic resonance (MR) are red. Structures created with ChemDraw. (C) Dynamic ^{18}F FET imaging of a glioma patient reveals intratumoral heterogeneity. The single time point ^{18}F FET image with anatomic magnetic resonance imaging (MRI) overlay (left) shows differential uptake of the probe. Kinetic data from specific regions (right) show the tumor periphery consistently accumulates ^{18}F FET (top), whereas the interior has a quick initial uptake of tracer followed by a steady decline of PET signal (bottom). These time courses correspond to WHO grade III and II phenotypes, respectively, as identified by matched histopathology. (C reprinted, with permission, from Kunz et al. 2011, © The Author(s) 2011. Published by Oxford University Press on behalf of the Society for Neuro-Oncology.)

porters (LATs). Up-regulation of the LATs in many cancers has been interpreted as a mechanism for fueling proliferative protein synthesis (Okubo et al. 2010; Wang et al. 2015; Häfliger and Charles 2019).

The original and most implemented amino acid-based PET probe is $[^{11}\text{C}]$ -methyl-L-methi-

onine (^{11}C -MET) (Fig. 3Bii; Bustany et al. 1986). ^{11}C -MET has been successfully used to image gliomas in the clinic, outperforming FDG-PET, particularly in low-grade tumors (Singhal et al. 2008; Sharma et al. 2016; Xu et al. 2017; Ninatti et al. 2022). The high spatial resolution of PET can enable discrimination between intratumoral

subcomponents; in one clinical study, low-grade astrocytomas showed increased ^{11}C -MET uptake in infiltrative exterior regions compared to interior regions with a solid tumor phenotype (Kracht et al. 2004).

As with all ^{11}C -based PET probes, the primary limitation of ^{11}C -MET is its short radioactive half-life. As such, there has been an effort to develop ^{18}F -labeled amino acid derivatives, the most notable example of which is *O*-(2- ^{18}F fluoroethyl)-L-tyrosine (^{18}F FET) (Fig. 3Biii; Langen et al. 2017). ^{18}F FET has found widespread success in the imaging of brain tumors. In particular, ^{18}F FET has markedly high sensitivity in the disambiguation of high-grade gliomas from lesions that appear identically in standard MRI, such as brain metastases and primary lymphomas (Puranik et al. 2019). The long lifetime of ^{18}F FET enables the measurement of probe uptake kinetics over the course of around an hour (Jansen et al. 2012, 2014; Lohmann et al. 2015). Dynamic information can be used to differentiate local phenotypes. For example, one kinetic study of ^{18}F FET showed that low-grade gliomas constantly import and retain tracer, whereas high-grade tumors have an early peak of uptake followed by a steady decline of PET signal (Fig. 3C; Kunz et al. 2011). Heterogeneity within tumors was also observed in the form of “hot spots” of high-grade-like malignant regions. One factor that may play a part in differential probe dynamics is specific interactions with LAT1. One study used a model of purified LAT1 reconstituted in *Xenopus* oocytes to show that ^{18}F FET is taken into cells by LAT1 but not effluxed (Habermeier et al. 2015). This asymmetry could help explain why ^{18}F FET accumulates in high-LAT1 gliomas despite a lack of probe incorporation into cellular protein.

Another amino acid-based PET probe that has shown success is the glutamate analog (S)-4-(3- ^{18}F fluoropropyl)-L-glutamate (^{18}F FSPG) (Fig. 3Biv; Koglin et al. 2011). ^{18}F FSPG is imported into cells via system x_c^- , which exchanges glutamate for cystine. Up-regulation of system x_c^- has been observed in many cancers and has been linked to several factors promoting malignancy. Cystine imported by system x_c^- is reduced in the cell to cysteine, a precursor of glu-

tathione (GSH), the most abundant antioxidant molecule. Therefore, increased uptake of ^{18}F FSPG by system x_c^- has been interpreted as an imaging biomarker of increased tumor cell resistance to oxidative stress (McCormick et al. 2018). In clinical trials spanning a variety of cancer types, ^{18}F FSPG was shown to outperform FDG in distinguishing lesions (Baek et al. 2012; Kavanaugh et al. 2016; Park et al. 2020; Wardak et al. 2022).

Nucleoside Salvage

Another hallmark of the proliferating cancer cells is increased nucleoside metabolism. Uptake of ^{18}F 3'-deoxy-3'-fluorothymidine (^{18}F FLT), a PET analog of thymidine (Shields et al. 1998) has been shown to correlate to proliferation (Fig. 3Bv). ^{18}F FLT is trapped in cells upon phosphorylation via thymidine kinase (TK), the first step in the *de novo* DNA biosynthesis pathway. ^{18}F FLT has been used in the clinic as a sensitive probe of tumor proliferation in brain tumors (Chen et al. 2005; Choi et al. 2005). A limitation of ^{18}F FLT is that it is specific to the thymidine salvage pathway. One study showed that ^{18}F FLT is not avidly taken up by tumor subtypes that rely on *de novo* thymidine synthesis, a complementary and competitive pathway (McKinley et al. 2013). Therefore, care should be taken not to conflate ^{18}F FLT uptake with more general proliferative markers, such as Ki67 staining.

Recent work has identified ^{18}F clofarabine (^{18}F CFA) as a promising nucleoside analog PET probe for imaging of nucleoside salvage (Fig. 3Bvi; Kim et al. 2016). ^{18}F CFA is a highly specific substrate for deoxycytidine kinase (dCK), and was shown to accumulate in leukemia cells. ^{18}F CFA has also been investigated as a probe of immunotherapy response in preclinical models of glioma (Antonios et al. 2017). Activated T cells up-regulate dCK, so ^{18}F CFA uptake can be interpreted as an imaging biomarker of activated T cell infiltration.

In conclusion, tumor cells power proliferative growth by up-regulating the biosynthesis of lipids, proteins, and DNA. These anabolic pathways can take up constituent carbon atoms from

T. Ruan and K.R. Keshari

the extracellular space, allowing imaging of anabolism through the labeling of building block molecules such as acetate, amino acids, and nucleosides, respectively.

Phenotypic Consequences of Cancer Metabolism

This last section will focus on imaging probes that target phenotypic traits associated with cancer metabolism: altered redox balance, acidification of the tumor microenvironment (TME), and hypoxia.

Redox Status

Rapid proliferation generates high levels of reactive oxygen species, leading to an oxidative stress phenotype. Elevated levels of antioxidants, primarily GSH, have been identified as a mechanism for tumor resistance to radiation or chemotherapy. Infusion of ^{13}C -labeled glycine, a building block of GSH, allows direct measurement of GSH by ^{13}C MRS in tumors (Thelwall et al. 2005, 2012). However, the scan times for these experiments are prohibitively long for widespread application.

HP [$1\text{-}^{13}\text{C}$]dehydroascorbic acid (DHA) is a promising probe of redox status: it has a favorable T_1 of 57 sec at 3 T, is preferentially taken up by tumor cells, and undergoes rapid reduction to [$1\text{-}^{13}\text{C}$]vitamin C with a chemical shift difference of 3.8 ppm (Fig. 4Ai; Bohndiek et al. 2011). There are two factors that influence the kinetics of DHA metabolism. First, DHA is reduced to vitamin C in the cell by enzymes that use GSH or NADPH as a cofactor, so the ratio of vitamin C to DHA functions as an indirect readout of the redox state of the cell. The ratio of HP DHA to vitamin C is elevated in lymphoma, prostate cancer, and colorectal cancer tumors, reflecting unbalanced redox phenotypes (Keshari et al. 2011; Timm et al. 2017). Another factor that influences the kinetics of DHA reduction is an expression of the GLUT transporters, which import DHA in addition to sugars. In a transgenic prostate cancer mouse model, increased vitamin C/DHA ratios in tumors corre-

lated with avid FDG-PET uptake (Fig. 4B; Keshari et al. 2013). Immunohistochemistry confirmed that these tumors up-regulate GLUT3 and GLUT4, accounting for the increase of both PET and HP MR probe import. The path to clinical translation of HP DHA has been complicated by concerns with toxicity. In one study, formulations of DHA administered at 10 mg/kg dose to tumor-bearing mice induced respiratory arrest and cardiac depression (Timm et al. 2017). However, studies using large animals and non-human primates showed that doses of upward of 500 mg/kg can be well tolerated, suggesting differential pharmacology of DHA (Banerjee et al. 1953; Ducruet et al. 2011). More work on the mechanisms of DHA toxicity is required before clinical translation of this probe can progress.

^{11}C -labeled DHA and vitamin C have also been developed as PET probes for redox, although these molecules are less sensitive to changes in the chemotherapeutic depletion of GSH than HP DHA (Carroll et al. 2016, Qin et al. 2018). A recent alternative for imaging DHA/vitamin C redox is the PET probe ^{18}F -KS1, a modified radioanalogue of vitamin C (Fig. 4Aii; Sai et al. 2019). ^{18}F -KS1 shows tumor specificity and favorable pharmacokinetics in rodent and nonhuman primate tumor models, making it attractive for clinical application (Damuka et al. 2022). The next step for ^{18}F -KS1 translation is a pilot study in humans. Another recently reported PET probe for redox is 4- ^{18}F fluoro-1-naphthol (^{18}F 4FN) (Pisaneschi et al. 2022). This probe is sensitive only to radical species with high redox potential, allowing specific imaging of innate immunity activation. Although ^{18}F 4FN has yet to be applied to the context of cancer metabolism, its mechanism provides the proof of concept of a tunable redox PET sensor, which may be leveraged for finer-grained quantification of intracellular redox states in cancer.

Extracellular pH

Acidification of the TME caused by excess lactate production is a widely observed cancer metabolic phenotype. Tumors evolve to thrive in this

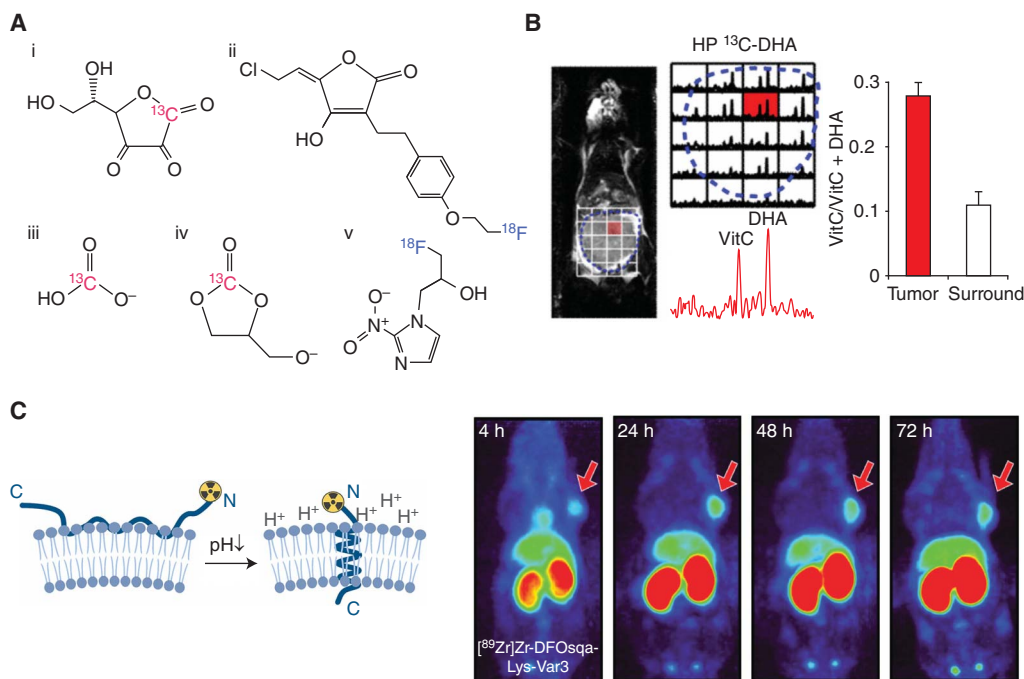


Figure 4. Molecular imaging of cancer metabolic phenotypes. (A) Chemical structures of probes for imaging redox, pH, and hypoxia. (i) [^{13}C]dehydroascorbic acid (DHA), (ii) (E)-5-(2-chloroethylidene)-3-((4-(2- ^{18}F) fluoroethoxy)benzyl)oxy)-4-hydroxyfuran-2(5H)-one (KS1), (iii) [^{13}C]bicarbonate, (iv) [^{13}C]1,2-glycerol carbonate, (v) [^{18}F]fluoromisonidazole (^{18}F -FMISO). β -Emitting radioisotopes detected by positron emission tomography (PET) are blue, and nuclei detected by magnetic resonance (MR) are red. Structures created with ChemDraw. (B) Measurement of intracellular redox states with magnetic resonance spectroscopic imaging (MRSI) of HP DHA. Anatomic coronal MR image of a transgenic model of prostate cancer mouse with tumor delineated with blue dashed line and overlaid spectra of HP DHA MRSI (left). Representative spectrum localized to the tumor (bottom middle) shows high uptake of DHA and conversion to vitamin C. Metabolite ratios summed over multiple spectra (right) show a 2.5-fold increase of flux of HP DHA to vitamin C in the tumor compared to surrounding healthy tissue, reflecting higher cellular concentrations of glutathione and increased transport of DHA via the glucose transporters GLUT1/3/4. (B reprinted, with permission, from Keshari et al. 2013, © SNMML.) (C) Structure of pHLIP probe (left) shows DOTA chelator moiety, which can bind to copper radio-nuclides for PET imaging, bound to a 37-residue long peptide sequence. At neutral pH, the peptide has a random coil conformation, but in acidic environments can form an α -helical structure capable of stable transmembrane incorporation. Example whole-body coronal and axial PET images of ^{64}Cu -DOTA-pHLIP in prostate cancer xenograft mice (right) show higher probe uptake in LNCaP (left) over PC3 (right), corresponding with increased acidity in LNCaP (measured tumor $\text{pH}_e = 6.78$) compared to PC3 (measured tumor $\text{pH}_e = 7.23$). (C, created with BioRender, was adapted from Bauer et al. 2022 under the terms of the Creative Commons Attribution License (CC BY). Copyright © Bauer, Visca, Weerakkody, Cody, Samuels, Kaminsky, Andreev, Reshetnyak, and Lewis.).

acidic environment, with in vitro tumor cell proliferation maximized at a subphysiological pH of 6.8 (Gatenby and Gillies 2004; Zhang et al. 2010). Lowered extracellular pH (pH_e) has thus been investigated as an imaging biomarker of the Warburg effect. Imaging of pH_e is achieved with molecular probes that are sensitive to local changes in pH.

Historically, changes in pH were annotated using ^{31}P NMR spectroscopy and later spectroscopic imaging by measuring chemical shift changes (Stubbs et al. 1992). While these could be enhanced through the use of an exogenous contrast agent (Gillies et al. 1994), these approaches suffered from low sensitivity due to the nucleus chosen. pH imaging using ^1H MR

approaches, including relaxivity or magnetization transfer, was more suited for spatially resolved pH maps given the sensitivity of ^1H MRI (Gillies et al. 2004). Relaxivity imaging involves the injection of a contrast agent, typically a gadolinium chelate, whose effect on the T1 relaxation of the water ^1H MR signal is pH-sensitive (RaghuNand et al. 2002). Magnetization transfer experiments measure the exchange between labile hydrogens on an injected probe and bulk water. This exchange process is pH-dependent and can be measured with chemical exchange saturation transfer (CEST) techniques similar to those used in glucoCEST to indirectly infer pH (Ward and Balaban 2000; Sun and Sorensen 2008; Longo et al. 2014, 2016). One major drawback of both these methods is that the magnitude of the effect of pH on the signal is dependent on the local concentration of the contrast agents. These methods thus confound pH measurement with pharmacokinetic dynamics, requiring reproducible calibration curves. Since calibration of in vivo signals is often challenging, these methods have intrinsic issues with reproducibility and comparability across contexts.

Since PET signals are not inherently environmentally responsive, imaging pH_e with PET requires coupling probe retention to pH. One elegant strategy involves PET tracers conjugated to a pH (low) insertion peptide (pHLIP), a 36-amino acid-long peptide that only inserts into lipid bilayer membranes in an α -helical conformation at low pH (Reshetnyak et al. 2006). At physiological pH, pHLIP is in a random coil conformation and cannot insert into membranes. This means that a radioisotope-labeled pHLIP will only retain in membranes and give persistent PET signal in low pH regions. The first pHLIP-based PET probe was conjugated to ^{64}Cu , a radioisotope with an especially long half-life of ~ 12.8 h, and showed long-lasting uptake and retention in prostate cancer xenograft models (Fig. 4C; Våvere et al. 2009). Subsequent work has improved targeting specificity through structural modification of the peptide (Tapmeier et al. 2015; Wyatt et al. 2018) or substitution of ^{64}Cu with other radioisotopes such as ^{18}F (Dau-mar et al. 2012) or ^{89}Zr (Bauer et al. 2022). Cor-

relative histology of prostate cancer tumors showed that low pH_e regions detected by pHLIP-PET are associated with increased expression of carbonic anhydrase IX (CAIX), a tumor-associated acid-extruding protein (Viola-Villegas et al. 2014), linking imaging data to one molecular mechanism of TME acidification. So far there has been one phase I clinical trial of ^{18}F -labeled pHLIP (NCT04054986).

The most studied HP probe for acidification is [^{13}C]bicarbonate (Fig. 4Aiii; Gallagher et al. 2008). Bicarbonate is in pH-dependent equilibrium with carbon dioxide via CAIX, and up-regulation of CAIX is likely a predominant mechanism of tumor adaptation to hypoxia and TME acidification (Gallagher et al. 2015). The ratio of bicarbonate to carbon dioxide concentrations can be used to calculate pH using the Henderson–Hasselbach equation. Since carbon dioxide can freely diffuse across the cell membrane, the pH measured by HP bicarbonate does not distinguish between extracellular and intracellular compartments. However, some data suggest that this ratio is weighted to pH_e (Gallagher et al. 2011). One particular advantage of imaging injected bicarbonate is that it is an endogenous buffer molecule, making clinical translation possible. However, the solubility of sodium bicarbonate in suitable formulations for HP is poor (Wilson et al. 2010). Recent work has addressed this limitation through the polarization of a carbonate precursor and rapid base-catalyzed hydrolysis to form HP bicarbonate (Korenchan et al. 2016). To this end, [$1\text{-}^{13}\text{C}$] 1,2-glycerol carbonate was used to measure grade-dependent acidification in transgenic mouse models of prostate cancer, where pH_e was markedly lower in higher-grade tumors (Fig. 4Aiv; Korenchan et al. 2019). Interestingly, in mice that had both low- and high-grade lesions, pH imaging allowed the separation of benign from aggressive tumor regions. This study also found a positive correlation between acidic TME regions and high expression of MCT4, the predominant exporter of lactate.

Besides HP bicarbonate, a number of molecules have been investigated for HP pH imaging: ^{13}C -enriched *N*-(2-acetamido-2-aminoethanesulfonic acid (Flavell et al. 2015), [$1,5\text{-}^{13}\text{C}_2$]zy-

monic acid (Düwel et al. 2017), amino acid derivatives (Hundshammer et al. 2018), [2-¹³C, D₁₀]diethylmalonic acid (Korenchan et al. 2017), ¹⁵N-pyridine derivatives (Jiang et al. 2015), and ⁸⁹Y chelates (Jindal et al. 2010; Wang et al. 2020). Although these exotic probes all feature suitable in vitro HP probe characteristics such as favorable T1 times and chemical shift differences, it is unclear whether they have much translational utility due to issues with toxicity and in vivo uptake.

Hypoxia

Finally, a central feature of the TME that shapes tumor metabolic phenotypes is chronic and transient hypoxia. A reduction in oxygen limits the capacity for oxidative phosphorylation in tumor cells, driving the evolution of hypoxia-tolerant up-regulation of glycolysis. A number of methods have been developed to quantitatively image the partial pressure of oxygen, or concentration of oxygen dissolved in blood (pO₂).

The “gold standard” PET probe for hypoxia is [¹⁸F]fluoromisonidazole (¹⁸F-FMISO) (Fig. 4A_v; Rasey et al. 1989; Koh et al. 1992). Upon entry into cells, the nitro group on ¹⁸F-FMISO is rapidly reduced, primarily via xanthine oxide. In cells with physiological oxygen levels, reduced ¹⁸F-FMISO is oxidized to its original form, which can then be exported out of the cell. However, oxidation is not possible in hypoxic cells and the reduced probe becomes trapped. Oxidation capacity is used as a proxy for oxygen concentration in the cell, making ¹⁸F-FMISO an indirect reporter of hypoxia. ¹⁸F-FMISO has been used to map hypoxic regions in a wide variety of cancers (Rajendran et al. 2006; Hendrickson et al. 2011; Hugonnet et al. 2011; Cheng et al. 2013; Tong et al. 2016). Widespread clinical translation of ¹⁸F-FMISO as a diagnostic probe has proven difficult due to slow clearance of the probe from normoxic areas and consequently low tumor-to-background ratios. Therefore, other nitroimidazole-derived molecules are being explored for hypoxia imaging, the most promising of which is ¹⁸F-FAZA, which shows favorable pharmacokinetics over ¹⁸F-FMISO

and is currently under clinical investigation (Busk et al. 2013; Saga et al. 2015, 2016).

Oxygen levels can be directly imaged with electron paramagnetic resonance imaging (EPRI), a technique similar to MRI that instead detects unpaired electrons such as free radicals (Krishna et al. 2012). The high sensitivity and spatial resolution of EPRI have been used to map pO₂ in a variety of tumors (Yasui et al. 2017; Kishimoto et al. 2021; Virani et al. 2021). These studies tend to focus on the relationship between therapy resistance and hypoxia, a posited mechanism for tumor evasion to radiation. One comparative modality study in pancreatic cancer mouse xenograft models found that EPRI pO₂ measurements positively correlated with FDG-PET in the periphery of the tumor and negatively correlated in the center, indicating regional differences in response to hypoxia independent of glucose uptake (Yamamoto et al. 2020).

In conclusion, cancer metabolism can also be imaged from the perspective of the phenotypic features that both drive and arise in response to up-regulated proliferation. These characteristics include altered redox capacity in the cell, increased extracellular acidification, and transient or chronic hypoxia.

CONCLUDING REMARKS

This review has described various examples of PET and MR methods used to image cancer metabolism. We hope that this work provides a clear survey of the power of molecular imaging to investigate tumor metabolism in its native contexts. In the clinic, molecular imaging can delineate malignant regions based on their underlying metabolic phenotype, which might be invisible to anatomic imaging. In basic research, molecular imaging reveals aspects of spatial heterogeneity that guide the metabolism of cancers as they form, grow, and respond to treatment.

A molecular imaging research program is inherently interdisciplinary and recursive. Basic biology identifies suitable metabolic targets for molecular imaging. Chemists synthesize probes to target these metabolic processes, and nuclear physicists optimize methods for the detection of

T. Ruan and K.R. Keshari

the probes in vivo. Biochemists characterize the metabolic mechanisms governing imaging signal formation, leveraging the findings of molecular imaging to suggest new avenues of investigation. Each of these phases relies upon and informs the others. Successful scientific discovery in metabolic imaging of cancer requires the perspectives from both the biology of metabolism and the development of molecular imaging techniques.

ACKNOWLEDGMENTS

We thank Garon Scott, Roxanne Morris, and Briana Turner for helpful comments.

REFERENCES

- AbuSalim JE, Yamamoto K, Miura N, Blackman B, Brender JR, Mushti C, Seki T, Camphausen KA, Swenson RE, Krishna MC, et al. 2021. Simple esterification of [1-¹³C]- α -ketoglutarate enhances membrane permeability and allows for noninvasive tracing of glutamate and glutamine production. *ACS Chem Biol* **16**: 2144–2150. doi:10.1021/acscchembio.1c00561
- Aggarwal R, Vigneron DB, Kurhanewicz J. 2017. Hyperpolarized 1-[¹³C]-pyruvate magnetic resonance imaging detects an early metabolic response to androgen ablation therapy in prostate cancer. *Eur Urol* **72**: 1028–1029. doi:10.1016/j.eururo.2017.07.022
- Alavi A, Lakhani P, Mavi A, Kung JW, Zhuang H. 2004. PET: a revolution in medical imaging. *Radiol Clin North Am* **42**: 983–1001. doi:10.1016/j.rcl.2004.08.012
- Albers MJ, Bok R, Chen AP, Cunningham CH, Zierhut ML, Zhang VY, Kohler SJ, Tropp J, Hurd RE, Yen Y-F, et al. 2008. Hyperpolarized ¹³C lactate, pyruvate, and alanine: noninvasive biomarkers for prostate cancer detection and grading. *Cancer Res* **68**: 8607–8615. doi:10.1158/0008-5472.CAN-08-0749
- Altman BJ, Stine ZE, Dang CV. 2016. From Krebs to clinic: glutamine metabolism to cancer therapy. *Nat Rev Cancer* **16**: 619–634. doi:10.1038/nrc.2016.71
- An Z, Ganji SK, Tiwari V, Pinho MC, Patel T, Barnett S, Pan E, Mickey BE, Maher EA, Choi C. 2017. Detection of 2-hydroxyglutarate in brain tumors by triple-refocusing MR spectroscopy at 3T in vivo. *Magn Reson Med* **78**: 40–48. doi:10.1002/mrm.26347
- An Z, Tiwari V, Ganji SK, Baxter J, Levy M, Pinho MC, Pan E, Maher EA, Patel TR, Mickey BE, et al. 2018. Echo-planar spectroscopic imaging with dual-readout alternated gradients (DRAG-EPSI) at 7 T: application for 2-hydroxyglutarate imaging in glioma patients. *Magn Reson Med* **79**: 1851–1861. doi:10.1002/mrm.26884
- Andronesi OC, Loebel F, Bogner W, Marjańska M, Heiden MG, Iafate AJ, Dietrich J, Batchelor TT, Gerstner ER, Kaelin WG, et al. 2016. Treatment response assessment in IDH-mutant glioma patients by noninvasive 3D functional spectroscopic mapping of 2-hydroxyglutarate. *Clin Cancer Res* **22**: 1632–1641. doi:10.1158/1078-0432.CCR-15-0656
- Antonios JP, Soto H, Everson RG, Moughon DL, Wang AC, Orpilla J, Radu C, Ellingson BM, Lee JT, Cloughesy T, et al. 2017. Detection of immune responses after immunotherapy in glioblastoma using PET and MRI. *Proc Natl Acad Sci* **114**: 10220–10225. doi:10.1073/pnas.1706689114
- Ardenkjær-Larsen JH, Fridlund B, Gram A, Hansson G, Hansson L, Lerche MH, Servin R, Thaning M, Golman K. 2003. Increase in signal-to-noise ratio of >10,000 times in liquid-state NMR. *Proc Natl Acad Sci* **100**: 10158–10163. doi:10.1073/pnas.1733835100
- Baek S, Choi C-M, Ahn SH, Lee JW, Gong G, Ryu JS, Oh SJ, Bacher-Stier C, Fels L, Koglin N, et al. 2012. Exploratory clinical trial of (4S)-4-(3-[¹⁸F]fluoropropyl)-L-glutamate for imaging x_C⁻ transporter using positron emission tomography in patients with non-small cell lung or breast cancer. *Clin Cancer Res* **18**: 5427–5437. doi:10.1158/1078-0432.CCR-12-0214
- Banerjee S, Belavady B, Mukherjee AK. 1953. Effect of dehydroascorbic acid in rabbits. *Proc Soc Exp Biol Med* **83**: 133–135. doi:10.3181/00379727-83-20287
- Bankson JA, Walker CM, Ramirez MS, Stefan W, Fuentes D, Merritt ME, Lee J, Sandulache VC, Chen Y, Phan L, et al. 2015. Kinetic modeling and constrained reconstruction of hyperpolarized [1-¹³C]-pyruvate offers improved metabolic imaging of tumors. *Cancer Res* **75**: 4708–4717. doi:10.1158/0008-5472.CAN-15-0171
- Bastiaansen JAM, Cheng T, Lei H, Gruetter R, Comment A. 2015. Direct noninvasive estimation of myocardial tricarboxylic acid cycle flux in vivo using hyperpolarized ¹³C magnetic resonance. *J Mol Cell Cardiol* **87**: 129–137. doi:10.1016/j.yjmcc.2015.08.012
- Batsios G, Taglang C, Cao P, Gillespie AM, Najac C, Subramani E, Wilson DM, Flavell RR, Larson PEZ, Ronen SM, et al. 2021. Imaging 6-phosphogluconolactonase activity in brain tumors in vivo using hyperpolarized δ -[1-¹³C]gluconolactone. *Front Oncol* **11**: 589570. doi:10.3389/fonc.2021.589570
- Bauer D, Visca H, Weerakkody A, Carter LM, Samuels Z, Kaminsky S, Andreev OA, Reshetnyak YK, Lewis JS. 2022. PET imaging of acidic tumor environment with 89Zr-labeled pHLIP probes. *Front Oncol* **12**: 882541. doi:10.3389/fonc.2022.882541
- Bender B, Herz K, Deshmane A, Richter V, Tabatabai G, Schittenhelm J, Skardelly M, Scheffler K, Ernemann U, Kim M, et al. 2022. GLINT: GlucoCEST in neoplastic tumors at 3 T—clinical results of GlucoCEST in gliomas. *MAGMA* **35**: 77–85. doi:10.1007/s10334-021-00982-5
- Bohndiek SE, Kettunen MI, Hu D, Kennedy BWC, Boren J, Gallagher FA, Brindle KM. 2011. Hyperpolarized [1-¹³C]-ascorbic and dehydroascorbic acid: vitamin C as a probe for imaging redox status in vivo. *J Am Chem Soc* **133**: 11795–11801. doi:10.1021/ja2045925
- Bohndiek SE, Kettunen MI, Hu D, Brindle KM. 2012. Hyperpolarized ¹³C spectroscopy detects early changes in tumor vasculature and metabolism after VEGF neutralization. *Cancer Res* **72**: 854–864. doi:10.1158/0008-5472.CAN-11-2795
- Bouvet V, Jans HS, Wuest M, Soueidan O-M, Mercer J, McEwan AJ, West FG, Cheeseman CI, Wuest F. 2014.

- Automated synthesis and dosimetry of 6-deoxy-6-[(18)F]fluoro-D-fructose (6-[(18)F]FDF): a radiotracer for imaging of GLUT5 in breast cancer. *Am J Nucl Med Mol Imaging* **4**: 248–259.
- Brindle KM, Bohndiek SE, Gallagher FA, Kettunen MI. 2011. Tumor imaging using hyperpolarized ¹³C magnetic resonance spectroscopy. *Magn Reson Med* **66**: 505–519. doi:10.1002/mrm.22999
- Busk M, Mortensen LS, Nordmark M, Overgaard J, Jakobsen S, Hansen KV, Theil J, Kallehauge JF, D'Andrea FP, Steiniche T, et al. 2013. PET hypoxia imaging with FAZA: reproducibility at baseline and during fractionated radiotherapy in tumour-bearing mice. *Eur J Nucl Med Mol Imaging* **40**: 186–197. doi:10.1007/s00259-012-2258-x
- Bustany P, Chatel M, Derlon JM, Darcel F, Sgouropoulos P, Soussaline F, Syrota A. 1986. Brain tumor protein synthesis and histological grades: a study by positron emission tomography (PET) with C11-L-methionine. *J Neurooncol* **3**: 397–404. doi:10.1007/BF00165590
- Cabella C, Karlsson M, Canapè C, Catanzaro G, Serra SC, Miragoli L, Poggi L, Uggeri F, Venturi L, Jensen PR, et al. 2013. In vivo and in vitro liver cancer metabolism observed with hyperpolarized [5-¹³C]glutamine. *J Magn Reson* **232**: 45–52. doi:10.1016/j.jmr.2013.04.010
- Canapè C, Catanzaro G, Terreno E, Karlsson M, Lerche MH, Jensen PR. 2015. Probing treatment response of glutaminolytic prostate cancer cells to natural drugs with hyperpolarized [5-¹³C]glutamine. *Magn Reson Med* **73**: 2296–2305. doi:10.1002/mrm.25360
- Capozza M, Anemone A, Dhakan C, Peruta MD, Bracesco M, Zullino S, Villano D, Terreno E, Longo DL, Aime S. 2022. GlucoCEST MRI for the evaluation response to chemotherapeutic and metabolic treatments in a murine triple-negative breast cancer: a comparison with [¹⁸F]FDG-PET. *Mol Imaging Biol* **24**: 126–134. doi:10.1007/s11307-021-01637-6
- Carroll VN, Truillet C, Shen B, Flavell RR, Shao X, Evans MJ, VanBrocklin HF, Scott PJH, Chin FT, Wilson DM. 2016. [¹¹C]Ascorbic and [¹¹C]dehydroascorbic acid, an endogenous redox pair for sensing reactive oxygen species using positron emission tomography. *Chem Commun* **52**: 4888–4890. doi:10.1039/C6CC00895J
- Carson RE. 2003. Tracer kinetic modeling in PET. In *Positron emission tomography: basic science and clinical practice* (ed. Valk PE, et al.), pp. 147–179. Springer, Amsterdam.
- Cember ATJ, Wilson NE, Rich LJ, Bagga P, Nanga RPR, Swago S, Swain A, Thakuri D, Elliot M, Schnall MD, et al. 2022. Integrating ¹H MRS and deuterium labeled glucose for mapping the dynamics of neural metabolism in humans. *Neuroimage* **251**: 118977. doi:10.1016/j.neuroimage.2022.118977
- Chaumeil MM, Larson PEZ, Yoshihara HAI, Danforth OM, Vigneron DB, Nelson SJ, Pieper RO, Phillips JJ, Ronen SM. 2013. Non-invasive in vivo assessment of IDH1 mutational status in glioma. *Nat Commun* **4**: 2429. doi:10.1038/ncomms3429
- Chaumeil MM, Radoul M, Najac C, Eriksson P, Viswanath P, Blough MD, Chesnelong C, Luchman HA, Cairncross JG, Ronen SM. 2016. Hyperpolarized ¹³C MR imaging detects no lactate production in mutant IDH1 gliomas: implications for diagnosis and response monitoring. *Neuroimage Clin* **12**: 180–189. doi:10.1016/j.nicl.2016.06.018
- Chen W, Cloughesy T, Kamdar N, Satyamurthy N, Bergsneider M, Liau L, Mischel P, Czernin J, Phelps ME, Silverman DHS. 2005. Imaging proliferation in brain tumors with ¹⁸F-FLT PET: comparison with ¹⁸F-FDG. *J Nucl Med* **46**: 945–952.
- Chen AP, Hurd RE, Schroeder MA, Lau AZ, Gu Y, Lam WW, Barry J, Tropp J, Cunningham CH. 2012. Simultaneous investigation of cardiac pyruvate dehydrogenase flux, Krebs cycle metabolism and pH, using hyperpolarized [1,2-¹³C₂]pyruvate in vivo. *NMR Biomed* **25**: 305–311. doi:10.1002/nbm.1749
- Chen H-Y, Aggarwal R, Bok RA, Ohliger MA, Zhu Z, Lee P, Gordon JW, Crikkinge M van, Carvajal L, Slater JB, et al. 2020. Hyperpolarized ¹³C-pyruvate MRI detects real-time metabolic flux in prostate cancer metastases to bone and liver: a clinical feasibility study. *Prostate Cancer P D* **23**: 269–276. doi:10.1038/s41391-019-0180-z
- Chen M, Zhu W, Du J, Yang C, Han B, Zhou D, Huo L, Zhuang J. 2021. ¹¹C-acetate positron emission tomography is more precise than ¹⁸F-fluorodeoxyglucose positron emission tomography in evaluating tumor burden and predicting disease risk of multiple myeloma. *Sci Rep* **11**: 22188. doi:10.1038/s41598-021-01740-2
- Cheng J, Lei L, Xu J, Sun Y, Zhang Y, Wang X, Pan L, Shao Z, Zhang Y, Liu G. 2013. ¹⁸F-fluoromisonidazole PET/CT: a potential tool for predicting primary endocrine therapy resistance in breast cancer. *J Nucl Med* **54**: 333–340. doi:10.2967/jnumed.112.111963
- Chiavazza E, Viale A, Karlsson M, Aime S. 2013. ¹⁵N-permethylated amino acids as efficient probes for MRI-DNP applications. *Contrast Media Mol Imaging* **8**: 417–421. doi:10.1002/cmim.1538
- Cho A, Eskandari R, Miloushev VZ, Keshari KR. 2018. A non-synthetic approach to extending the lifetime of hyperpolarized molecules using D₂O solvation. *J Magn Reson* **295**: 57–62. doi:10.1016/j.jmr.2018.08.001
- Choi SJ, Kim JS, Kim JH, Oh SJ, Lee JG, Kim CJ, Ra YS, Yeo JS, Ryu JS, Moon DH. 2005. [¹⁸F]3'-deoxy-3'-fluorothymidine PET for the diagnosis and grading of brain tumors. *Eur J Nucl Med Mol Imaging* **32**: 653–659. doi:10.1007/s00259-004-1742-3
- Choi C, Ganji SK, DeBerardinis RJ, Hatanpaa KJ, Rakheja D, Kovacs Z, Yang X-L, Mashimo T, Raisanen JM, Marin-Valencia I, et al. 2012. 2-Hydroxyglutarate detection by magnetic resonance spectroscopy in IDH-mutated patients with gliomas. *Nat Med* **18**: 624–629. doi:10.1038/nm.2682
- Chung BT, Chen H-Y, Gordon J, Mammoli D, Sriram R, Autry AW, Page LML, Chaumeil M, Shin P, Slater J, et al. 2019. First hyperpolarized [2-¹³C]pyruvate MR studies of human brain metabolism. *J Magn Reson* **309**: 106617. doi:10.1016/j.jmr.2019.106617
- Clarke DD. 1991. Fluoroacetate and fluorocitrate: mechanism of action. *Neurochem Res* **16**: 1055–1058.
- Cooper AJL, Krasnikov BF, Pinto JT, Kung HF, Li J, Ploessl K. 2012. Comparative enzymology of (2S,4R)4-fluoroglutamine and (2S,4R)4-fluoroglutamate. *Comp Biochem Physiol B Biochem Mol Biol* **163**: 108–120. doi:10.1016/j.cbpb.2012.05.010
- Crane JC, Gordon JW, Chen H, Autry AW, Li Y, Olson MP, Kurhanewicz J, Vigneron DB, Larson PEZ, Xu D. 2021.

T. Ruan and K.R. Keshari

- Hyperpolarized ^{13}C MRI data acquisition and analysis in prostate and brain at University of California, San Francisco. *NMR Biomed* **34**: e4280. doi:10.1002/nbm.4280
- Czernin J, Allen-Auerbach M, Nathanson D, Herrmann K. 2013. PET/CT in oncology: current status and perspectives. *Curr Radiol Rep* **1**: 177–190. doi:10.1007/s40134-013-0016-x
- Dafni H, Larson PEZ, Hu S, Yoshihara HAI, Ward CS, Venkatesh HS, Wang C, Zhang X, Vigneron DB, Ronen SM. 2010. Hyperpolarized ^{13}C spectroscopic imaging informs on hypoxia-inducible factor-1 and Myc activity downstream of platelet-derived growth factor receptor. *Cancer Res* **70**: 7400–7410. doi:10.1158/0008-5472.CAN-10-0883
- Damuka N, Bashetti N, Mintz A, Bansode AH, Miller M, Krizan I, Furdai C, Bhoopal B, Gollapelli K, Kumar JS, et al. 2022. [^{18}F]K51, a novel ascorbate-based ligand images ROS in tumor models of rodents and nonhuman primates. *Biomed Pharmacother* **156**: 113937. doi:10.1016/j.biopha.2022.113937
- Dang L, White DW, Gross S, Bennett BD, Bittinger MA, Driggers EM, Fantin VR, Jang HG, Jin S, Keenan MC, et al. 2009. Cancer-associated IDH1 mutations produce 2-hydroxyglutarate. *Nature* **462**: 739–744. doi:10.1038/nature08617
- Daumar P, Wanger-Baumann CA, Pillarsetty N, Fabrizio L, Carlin SD, Andreev OA, Reshetnyak YK, Lewis JS. 2012. Efficient ^{18}F -labeling of large 37-amino-acid pHLIP peptide analogs and their biological evaluation. *Bioconjug Chem* **23**: 1557–1566. doi:10.1021/bc3000222
- Day SE, Kettunen MI, Gallagher FA, Hu DE, Lerche M, Wolber J, Golman K, Ardenkjær-Larsen JH, Brindle KM. 2007. Detecting tumor response to treatment using hyperpolarized ^{13}C magnetic resonance imaging and spectroscopy. *Nat Med* **13**: 1382–1387. doi:10.1038/nm1650
- DeBerardinis RJ, Cheng T. 2010. Q's next: the diverse functions of glutamine in metabolism, cell biology and cancer. *Oncogene* **29**: 313–324. doi:10.1038/onc.2009.358
- DeBerardinis RJ, Keshari KR. 2022. Metabolic analysis as a driver for discovery, diagnosis, and therapy. *Cell* **185**: 2678–2689. doi:10.1016/j.cell.2022.06.029
- De Feyter HMD, de Graaf RA. 2021. Deuterium metabolic imaging—back to the future. *J Magn Reson* **326**: 106932. doi:10.1016/j.jmr.2021.106932
- De Feyter HMD, Behar KL, Corbin ZA, Fulbright RK, Brown PB, McIntyre S, Nixon TW, Rothman DL, de Graaf RA. 2018. Deuterium metabolic imaging (DMI) for MRI-based 3D mapping of metabolism in vivo. *Sci Adv* **4**: eaat7314. doi:10.1126/sciadv.aat7314
- Deh K, Zhang G, Park AH, Cunningham CH, Bragagnolo ND, Lyashchenko S, Ahmed S, Leftin A, Coffee E, Hricak H, et al. 2024. First in-human evaluation of [^{13}C] pyruvate in D_2O for hyperpolarized MRI of the brain: a safety and feasibility study. *Magn Reson Med* **11**: 10.1002/mrm.30002.
- de Kouchkovsky I, Chen HY, Ohliger MA, Wang ZJ, Bok RA, Gordon JW, Larson PEZ, Frost M, Okamoto K, Cooperberg MR, et al. 2022. Hyperpolarized 1- ^{13}C -pyruvate magnetic resonance imaging detects an early metabolic response to immune checkpoint inhibitor therapy in prostate cancer. *Eur Urol* **81**: 219–221. doi:10.1016/j.eururo.2021.10.015
- Dong Y, Eskandari R, Ray C, Granlund KL, Santos-Cunha LD, Miloushev VZ, Tee SS, Jeong S, Aras O, Chen YB, et al. 2018. Hyperpolarized MRI visualizes Warburg effects and predicts treatment response to mTOR inhibitors in patient-derived ccRCC xenograft models. *Cancer Res* **79**: canres.2231.2018.
- Ducruet AF, Mack WJ, Mocco J, Hoh DJ, Coon AL, D'Ambrosio AL, Winfree CJ, Pinsky DJ, Connolly ES. 2011. Preclinical evaluation of postischemic dehydroascorbic acid administration in a large-animal stroke model. *Transl Stroke Res* **2**: 399–403. doi:10.1007/s12975-011-0084-2
- Durst M, Chiavazza E, Haase A, Aime S, Schwaiger M, Schulte RF. 2016. α -Trideuteromethyl[^{15}N]glutamine: a long-lived hyperpolarized perfusion marker. *Magn Reson Med* **76**: 1900–1904. doi:10.1002/mrm.26104
- Dutta P, Le A, Jagt DLV, Tsukamoto T, Martinez GV, Dang CV, Gillies RJ. 2013. Evaluation of LDH-A and glutaminase inhibition in vivo by hyperpolarized ^{13}C -pyruvate magnetic resonance spectroscopy of tumors. *Cancer Res* **73**: 4190–4195. doi:10.1158/0008-5472.CAN-13-0465
- Düwel S, Hundshammer C, Gersch M, Feurecker B, Steiger K, Buck A, Walch A, Haase A, Glaser SJ, Schwaiger M, et al. 2017. Imaging of pH in vivo using hyperpolarized ^{13}C -labelled zymonic acid. *Nat Commun* **8**: 15126. doi:10.1038/ncomms15126
- Ericson K, Lilja A, Bergström M, Collins VP, Eriksson L, Ehrin E, von Hoist H, Lundqvist H, Längström B, Moskinn M. 1985. Positron emission tomography with [^{11}C] methyl-L-methionine, [^{11}C]D-glucose, and [^{68}Ga] EDTA in supratentorial tumors. *J Comput Assist Tomogr* **9**: 683–689. doi:10.1097/00004728-198507010-00005
- Eskandari R, Kim N, Mamakhanyan A, Saoi M, Zhang G, Berishaj M, Granlund KL, Poot AJ, Cross J, Thompson CB, et al. 2022. Hyperpolarized [^{13}C ,4,4- $^2\text{H}_2$,5- ^{15}N]-L-glutamine provides a means of annotating in vivo metabolic utilization of glutamine. *Proc Natl Acad Sci* **119**: e2120595119. doi:10.1073/pnas.2120595119
- Fala M, Somai V, Dannhorn A, Hamm G, Gibson K, Couturier D, Hesketh R, Wright AJ, Takats Z, Bunch J, et al. 2021. Comparison of ^{13}C MRI of hyperpolarized [^{1-13}C] pyruvate and lactate with the corresponding mass spectrometry images in a murine lymphoma model. *Magn Reson Med* **85**: 3027–3035. doi:10.1002/mrm.28652
- Faubert B, Li KY, Cai L, Hensley CT, Kim J, Zacharias LG, Yang C, Do QN, Doucette S, Burguete D, et al. 2017. Lactate metabolism in human lung tumors. *Cell* **171**: 358–371.e9. doi:10.1016/j.cell.2017.09.019
- Flavell RR, von Morze C, Blecha JE, Korenchan DE, Crieckinge MV, Sriram R, Gordon JW, Chen H-Y, Subramaniam S, Bok RA, et al. 2015. Application of Good's buffers to pH imaging using hyperpolarized ^{13}C MRI. *Chem Commun* **51**: 14119–14122. doi:10.1039/C5CC05348J
- Gallagher BM, Fowler JS, Gutterson NI, MacGregor RR, Wan CN, Wolf AP. 1978. Metabolic trapping as a principle of radiopharmaceutical design: some factors responsible for the biodistribution of [^{18}F] 2-deoxy-2-fluoro-D-glucose. *J Nucl Med* **19**: 1154–1161.
- Gallagher FA, Kettunen MI, Day SE, Hu DE, Ardenkjær-Larsen JH, Zandt RIT, Jensen PR, Karlsson M, Golman K,

- Lerche MH, et al. 2008. Magnetic resonance imaging of pH in vivo using hyperpolarized ^{13}C -labelled bicarbonate. *Nature* **453**: 940–943. doi:10.1038/nature07017
- Gallagher FA, Kettunen MI, Brindle KM. 2011. Imaging pH with hyperpolarized ^{13}C . *NMR Biomed* **24**: 1006–1015. doi:10.1002/nbm.1742
- Gallagher FA, Sladen H, Kettunen MI, Serrao EM, Rodrigues TB, Wright A, Gill AB, McGuire S, Booth TC, Boren J, et al. 2015. Carbonic anhydrase activity monitored in vivo by hyperpolarized ^{13}C -magnetic resonance spectroscopy demonstrates its importance for pH regulation in tumors. *Cancer Res* **75**: 4109–4118. doi:10.1158/0008-5472.CAN-15-0857
- Gallagher FA, Woitek R, McLean MA, Gill AB, Garcia RM, Provenzano E, Riemer F, Kaggie J, Chhabra A, Ursprung S, et al. 2020. Imaging breast cancer using hyperpolarized carbon-13 MRI. *Proc Natl Acad Sci* **117**: 2092–2098. doi:10.1073/pnas.1913841117
- Gatenby RA, Gillies RJ. 2004. Why do cancers have high aerobic glycolysis? *Nat Rev Cancer* **4**: 891–899. doi:10.1038/nrc1478
- Gatenby RA, Vincent TL. 2003. An evolutionary model of carcinogenesis. *Cancer Res* **63**: 6212–6220.
- Gelbard AS, Christie TR, Clarke LP, Laughlin JS. 1977. Imaging of spontaneous canine tumours with ammonia and L-glutamine labeled with N-13. *J Nucl Med* **18**: 718–723.
- Gierse M, Nagel L, Keim M, Lucas S, Speidel T, Lobmeyer T, Winter G, Josten F, Karaali S, Fellermann M, et al. 2023. Parahydrogen-polarized fumarate for preclinical in vivo metabolic magnetic resonance imaging. *J Am Chem Soc* **145**: 5960–5969. doi:10.1021/jacs.2c13830
- Gillies RJ, Liu Z, Bhujwala Z. 1994. 31P-MRS measurements of extracellular pH of tumors using 3-aminopropylphosphonate. *Am J Physiol* **267**: C195–C203. doi:10.1152/ajpcell.1994.267.1.C195
- Gillies RJ, Raghunand N, Garcia-Martin ML, Gatenby RA. 2004. Ph imaging. A review of pH measurement methods and applications in cancers. *IEEE Eng Med Biol* **23**: 57–64. doi:10.1109/MEMB.2004.1360409
- Golman K, Olsson LE, Axelsson O, Månsson S, Karlsson M, Petersson JS. 2003. Molecular imaging using hyperpolarized ^{13}C . *Br J Radiol* **76**: S118–S127. doi:10.1259/bjr/26631666
- Golman K, Zandt RIT, Lerche M, Pehrson R, Ardenkjaer-Larsen JH. 2006. Metabolic imaging by hyperpolarized ^{13}C magnetic resonance imaging for in vivo tumor diagnosis. *Cancer Res* **66**: 10855–10860. doi:10.1158/0008-5472.CAN-06-2564
- Granlund KL, Tee SS, Vargas HA, Lyashchenko SK, Reznik E, Fine S, Laudone V, Eastham JA, Touijer KA, Reuter VE, et al. 2020. Hyperpolarized MRI of human prostate cancer reveals increased lactate with tumor grade driven by monocarboxylate transporter 1. *Cell Metab* **31**: 105–114. e3. doi:10.1016/j.cmet.2019.08.024
- Grashei M, Biechl P, Schilling F, Otto AM. 2022. Conversion of hyperpolarized $[1-^{13}\text{C}]$ pyruvate in breast cancer cells depends on their malignancy, metabolic program and nutrient microenvironment. *Cancers (Basel)* **14**: 1845. doi:10.3390/cancers14071845
- Grassi I, Nanni C, Allegri V, Morigi JJ, Montini GC, Castellucci P, Fanti S. 2011. The clinical use of PET with (11C) -acetate. *Am J Nucl Med Mol Imaging* **2**: 33–47.
- Grkovski M, Goel R, Krebs S, Staton KD, Harding JJ, Melinghoff IK, Humm JL, Dunphy MPS. 2020. Pharmacokinetic assessment of ^{18}F - $(2\text{S},4\text{R})$ -4-fluoroglutamine in patients with cancer. *J Nucl Med* **61**: 357–366. doi:10.2967/jnumed.119.229740
- Habermeier A, Graf J, Sandhöfer BF, Boissel J-P, Roesch F, Closs EI. 2015. System L amino acid transporter LAT1 accumulates O-(2-fluoroethyl)-L-tyrosine (FET). *Amino Acids* **47**: 335–344. doi:10.1007/s00726-014-1863-3
- Häfliger P, Charles RP. 2019. The L-type amino acid transporter LAT1—an emerging target in cancer. *Int J Mol Sci* **20**: 2428. doi:10.3390/ijms20102428
- Hanahan D, Weinberg RA. 2011. Hallmarks of cancer: the next generation. *Cell* **144**: 646–674. doi:10.1016/j.cell.2011.02.013
- Harris T, Degani H, Frydman L. 2013. Hyperpolarized ^{13}C NMR studies of glucose metabolism in living breast cancer cell cultures. *NMR Biomed* **26**: 1831–1843. doi:10.1002/nbm.3024
- Harrison C, Yang C, Jindal A, DeBerardinis RJ, Hooshyar MA, Merritt M, Sherry AD, Malloy CR. 2012. Comparison of kinetic models for analysis of pyruvate-to-lactate exchange by hyperpolarized ^{13}C NMR. *NMR Biomed* **25**: 1286–1294. doi:10.1002/nbm.2801
- Hendrickson K, Phillips M, Smith W, Peterson L, Krohn K, Rajendran J. 2011. Hypoxia imaging with $[F-18]$ FMISO-PET in head and neck cancer: potential for guiding intensity modulated radiation therapy in overcoming hypoxia-induced treatment resistance. *Radiother Oncol* **101**: 369–375. doi:10.1016/j.radonc.2011.07.029
- Herholz K, Heindel W, Luyten PR, denHollander JA, Pietrzyk U, Voges J, Kugel H, Friedmann G, Heiss WD. 1992. In vivo imaging of glucose consumption and lactate concentration in human gliomas. *Ann Neurol* **31**: 319–327. doi:10.1002/ana.410310315
- Herrero P, Dence CS, Coggan AR, Kisrieva-Ware Z, Eisenbeis P, Gropler RJ. 2007. L-3-11C-lactate as a PET tracer of myocardial lactate metabolism: a feasibility study. *J Nucl Med* **48**: 2046–2055. doi:10.2967/jnumed.107.044503
- Hövenner J, Pravidtsev AN, Kidd B, Bowers CR, Glöggler S, Kovtunov KV, Plaumann M, Katz-Brull R, Buckenmaier K, Jerschow A, et al. 2018. Parahydrogen-based hyperpolarization for biomedicine. *Angew Chem Int Ed* **57**: 11140–11162. doi:10.1002/anie.201711842
- Hu S, Lustig M, Balakrishnan A, Larson PEZ, Bok R, Kurhanewicz J, Nelson SJ, Goga A, Pauly JM, Vigneron DB. 2010. 3D compressed sensing for highly accelerated hyperpolarized ^{13}C MRSI with in vivo applications to transgenic mouse models of cancer. *Magn Reson Med* **63**: 312–321. doi:10.1002/mrm.22233
- Hu S, Balakrishnan A, Bok RA, Anderton B, Larson PEZ, Nelson SJ, Kurhanewicz J, Vigneron DB, Goga A. 2011. ^{13}C -pyruvate imaging reveals alterations in glycolysis that precede c-Myc-induced tumor formation and regression. *Cell Metab* **14**: 131–142. doi:10.1016/j.cmet.2011.04.012
- Hugonnet F, Fournier L, Medioni J, Smadja C, Hindié E, Huchet V, Itti E, Cuenod C-A, Chatellier G, Oudard S, et al. 2011. Metastatic renal cell carcinoma: relationship between initial metastasis hypoxia, change after 1 month's sunitinib, and therapeutic response: an ^{18}F -fluoromisonidazole PET/CT study. *J Nucl Med* **52**: 1048–1055. doi:10.2967/jnumed.110.084517

T. Ruan and K.R. Keshari

- Hundshammer C, Düwel S, Ruseckas D, Topping G, Dzien P, Müller C, Feurecker B, Hövener JB, Haase A, Schwaiger M, et al. 2018. Hyperpolarized amino acid derivatives as multivalent magnetic resonance pH sensor molecules. *Sensors* **18**: 600. doi:10.3390/s18020600
- Ido T, Wan C, Casella V, Fowler JS, Wolf AP, Reivich M, Kuhl DE. 1978. Labeled 2-deoxy-D-glucose analogs. ¹⁸F-labeled 2-deoxy-2-fluoro-D-glucose, 2-deoxy-2-fluoro-D-mannose and ¹⁴C-2-deoxy-2-fluoro-D-glucose. *J Label Compd Radiopharm* **14**: 175–183. doi:10.1002/jlcr.2580140204
- Izquierdo-Garcia JL, Viswanath P, Eriksson P, Cai L, Radoul M, Chaumeil MM, Blough M, Luchman HA, Weiss S, Cairncross JG, et al. 2015. *IDH1* mutation induces reprogramming of pyruvate metabolism. *Cancer Res* **75**: 2999–3009. doi:10.1158/0008-5472.CAN-15-0840
- Jadvar H. 2016. Is there use for FDG-PET in prostate cancer? *Semin Nucl Med* **46**: 502–506. doi:10.1053/j.semnuclmed.2016.07.004
- James ML, Gambhir SS. 2012. A molecular imaging primer: modalities, imaging agents, and applications. *Physiol Rev* **92**: 897–965. doi:10.1152/physrev.00049.2010
- Jansen NL, Graute V, Armbruster L, Suchorska B, Lutz J, Eigenbrod S, Cumming P, Bartenstein P, Tonn JC, Kreth FW, et al. 2012. MRI-suspected low-grade glioma: is there a need to perform dynamic PET PET? *Eur J Nucl Med Mol Imaging* **39**: 1021–1029. doi:10.1007/s00259-012-2109-9
- Jansen NL, Suchorska B, Wenter V, Eigenbrod S, Schmid-Tannwald C, Zwergal A, Niyazi M, Drexler M, Bartenstein P, Schnell O, et al. 2014. Dynamic ¹⁸F-FET PET in newly diagnosed astrocytic low-grade glioma identifies high-risk patients. *J Nucl Med* **55**: 198–203. doi:10.2967/jnumed.113.122333
- Jensen PR, Karlsson M, Meier S, Duus JØ, Lerche MH. 2009. Hyperpolarized amino acids for in vivo assays of transaminase activity. *Chemistry (Easton)* **15**: 10010–10012. doi:10.1002/chem.200901042
- Ježek P. 2020. 2-Hydroxyglutarate in cancer cells. *Antioxid Redox Sign* **33**: 903–926. doi:10.1089/ars.2019.7902
- Jiang W, Lumata L, Chen W, Zhang S, Kovacs Z, Sherry AD, Khemtung C. 2015. Hyperpolarized ¹⁵N-pyridine derivatives as pH-sensitive MRI agents. *Sci Rep* **5**: 9104. doi:10.1038/srep09104
- Jindal AK, Merritt ME, Suh EH, Malloy CR, Sherry AD, Kovács Z. 2010. Hyperpolarized ⁸⁹Y complexes as pH sensitive NMR probes. *J Am Chem Soc* **132**: 1784–1785. doi:10.1021/ja910278e
- Kavanaugh G, Williams J, Morris AS, Nickels ML, Walker R, Koglin N, Stephens AW, Washington MK, Geevarghese SK, Liu Q, et al. 2016. Utility of [¹⁸F]FSPG PET to image hepatocellular carcinoma: first clinical evaluation in a US population. *Mol Imaging Biol* **18**: 924–934. doi:10.1007/s11307-016-1007-0
- Kelloff GJ, Hoffman JM, Johnson B, Scher HI, Siegel BA, Cheng EY, Cheson BD, O'Shaughnessy J, Guyton KZ, Mankoff DA, et al. 2005. Progress and promise of FDG-PET imaging for cancer patient management and oncologic drug development. *Clin Cancer Res* **11**: 2785–2808. doi:10.1158/1078-0432.CCR-04-2626
- Keshari KR, Wilson DM. 2014. Chemistry and biochemistry of ¹³C hyperpolarized magnetic resonance using dynamic nuclear polarization. *Chem Soc Rev* **43**: 1627–1659. doi:10.1039/C3CS60124B
- Keshari KR, Wilson DM, Chen AP, Bok R, Larson PEZ, Hu S, Crieckinge MV, Macdonald JM, Vigneron DB, Kurhanewicz J. 2009. Hyperpolarized [2-¹³C]-fructose: a hemiketal DNP substrate for in vivo metabolic imaging. *J Am Chem Soc* **131**: 17591–17596. doi:10.1021/ja9049355
- Keshari KR, Kurhanewicz J, Bok R, Larson PEZ, Vigneron DB, Wilson DM. 2011. Hyperpolarized ¹³C dehydroascorbate as an endogenous redox sensor for in vivo metabolic imaging. *Proc Natl Acad Sci* **108**: 18606–18611. doi:10.1073/pnas.1106920108
- Keshari KR, Sai V, Wang ZJ, VanBrocklin HF, Kurhanewicz J, Wilson DM. 2013. Hyperpolarized [1-¹³C]dehydroascorbate MR spectroscopy in a murine model of prostate cancer: comparison with ¹⁸F-FDG PET. *J Nucl Med* **54**: 922–928. doi:10.2967/jnumed.112.115402
- Kim W, Le TM, Wei L, Poddar S, Bazy J, Wang X, Uong NT, Abt ER, Capri JR, Austin WR, et al. 2016. [¹⁸F]CFA as a clinically translatable probe for PET imaging of deoxycytidine kinase activity. *Proc Natl Acad Sci* **113**: 4027–4032. doi:10.1073/pnas.1524212113
- Kim M, Eleftheriou A, Ravotto L, Weber B, Rivlin M, Navon G, Capozza M, Anemone A, Longo DL, Aime S, et al. 2022. What do we know about dynamic glucose-enhanced (DGE) MRI and how close is it to the clinics? Horizon 2020 GLINT consortium report. *MAGMA* **35**: 87–104. doi:10.1007/s10334-021-00994-1
- Kishimoto S, Brender JR, Chandramouli GVR, Saida Y, Yamamoto K, Mitchell JB, Krishna MC. 2021. Hypoxia-activated prodrug evofosfamide treatment in pancreatic ductal adenocarcinoma xenografts alters the tumor redox status to potentiate radiotherapy. *Antioxid Redox Sign* **35**: 904–915. doi:10.1089/ars.2020.8131
- Koglin N, Mueller A, Berndt M, Schmitt-Willich H, Toschi L, Stephens AW, Gekeler V, Friebe M, Dinkelborg LM. 2011. Specific PET imaging of x_c⁻ transporter activity using a ¹⁸F-labeled glutamate derivative reveals a dominant pathway in tumor metabolism. *Clin Cancer Res* **17**: 6000–6011. doi:10.1158/1078-0432.CCR-11-0687
- Koh W-J, Rasey JS, Evans ML, Grierson JR, Lewellen TK, Graham MM, Krohn KA, Griffin TW. 1992. Imaging of hypoxia in human tumors with [F-18]fluoromisonidazole. *Int J Radiat Oncol Biol Phys* **22**: 199–212. doi:10.1016/0360-3016(92)91001-4
- Korenchan DE, Flavell RR, Baligand C, Sriram R, Neumann K, Sukumar S, VanBrocklin H, Vigneron DB, Wilson DM, Kurhanewicz J. 2016. Dynamic nuclear polarization of biocompatible ¹³C-enriched carbonates for in vivo pH imaging. *Chem Commun* **52**: 3030–3033. doi:10.1039/C5CC09724J
- Korenchan DE, Taglang C, von Morze C, Blecha JE, Gordon JW, Sriram R, Larson PEZ, Vigneron DB, VanBrocklin HF, Kurhanewicz J, et al. 2017. Dicarboxylic acids as pH sensors for hyperpolarized ¹³C magnetic resonance spectroscopic imaging. *Analyst* **142**: 1429–1433. doi:10.1039/C7AN00076F
- Korenchan DE, Bok R, Sriram R, Liu K, Santos RD, Qin H, Lobach I, Korn N, Wilson DM, Kurhanewicz J, et al. 2019. Hyperpolarized in vivo pH imaging reveals grade-dependent acidification in prostate cancer. *Oncotarget* **10**: 6096–6110. doi:10.18632/oncotarget.27225

- Kracht LW, Miletic H, Busch S, Jacobs AH, Voges J, Hoevels M, Klein JC, Herholz K, Heiss WD. 2004. Delineation of brain tumor extent with [^{11}C]L-methionine positron emission tomography local comparison with stereotactic histopathology. *Clin Cancer Res* **10**: 7163–7170. doi:10.1158/1078-0432.CCR-04-0262
- Kreis F, Wright AJ, Hesse F, Fala M, Hu D, Brindle KM. 2019. Measuring tumor glycolytic flux in vivo by using fast deuterium MRI. *Radiology* **294**: 191242.
- Krishna MC, Matsumoto S, Yasui H, Saito K, Devasahayam N, Subramanian S, Mitchell JB. 2012. Electron paramagnetic resonance imaging of tumor pO_2 . *Radiat Res* **177**: 376–386. doi:10.1667/RR2622.1
- Kunz M, Thon N, Eigenbrod S, Hartmann C, Egensperger R, Herms J, Geisler J, la Fougere C, Lutz J, Linn J, et al. 2011. Hot spots in dynamic ^{18}F -PET-PET delineate malignant tumor parts within suspected WHO grade II gliomas. *Neuro Oncol* **13**: 307–316. doi:10.1093/neuonc/noq196
- Kurhanewicz J, Vigneron DB, Ardenkjaer-Larsen JH, Bankson JA, Brindle K, Cunningham CH, Gallagher FA, Keshari KR, Kjaer A, Laustsen C, et al. 2019. Hyperpolarized ^{13}C MRI: path to clinical translation in oncology. *Neoplasia* **21**: 1–16. doi:10.1016/j.neo.2018.09.006
- Langen KJ, Stoffels G, Filss C, Heinzel A, Stegmayr C, Lohmann P, Willuweit A, Neumaier B, Mottaghy FM, Galldiks N. 2017. Imaging of amino acid transport in brain tumours: positron emission tomography with O-(2- ^{18}F)fluoroethyl)-L-tyrosine (FET). *Methods* **130**: 124–134. doi:10.1016/j.ymeth.2017.05.019
- Lau JYC, Chen AP, Gu Y, Cunningham CH. 2016. Voxel-by-voxel correlations of perfusion, substrate, and metabolite signals in dynamic hyperpolarized ^{13}C imaging. *NMR Biomed* **29**: 1038–1047. doi:10.1002/nbm.3564
- Lewis DY, Boren J, Shaw GL, Bielik R, Ramos-Montoya A, Larkin TJ, Martins CP, Neal DE, Soloviev D, Brindle KM. 2014. Late imaging with [^{11}C]acetate improves detection of tumor fatty acid synthesis with PET. *J Nucl Med* **55**: 1144–1149. doi:10.2967/jnumed.113.134437
- Lieberman BP, Ploessl K, Wang L, Qu W, Zha Z, Wise DR, Chodosh LA, Belka G, Thompson CB, Kung HF. 2011. PET imaging of glutaminolysis in tumors by ^{18}F -(2S,4R) 4-fluoroglutamine. *J Nucl Med* **52**: 1947–1955. doi:10.2967/jnumed.111.093815
- Lindhe Ö, Sun A, Ulin J, Rahman O, Långström B, Sörensen J. 2009. [^{18}F]Fluoroacetate is not a functional analogue of [^{11}C]acetate in normal physiology. *Eur J Nucl Med Mol Imaging* **36**: 1453. doi:10.1007/s00259-009-1128-7
- Liu F, Xu X, Zhu H, Zhang Y, Yang J, Zhang L, Li N, Zhu L, Kung HF, Yang Z. 2018. PET imaging of ^{18}F -(2S,4R)4-fluoroglutamine accumulation in breast cancer: from xenografts to patients. *Mol Pharm* **15**: 3448–3455. doi:10.1021/acs.molpharmaceut.8b00430
- Lohmann P, Herzog H, Kops ER, Stoffels G, Judov N, Filss C, Galldiks N, Tellmann L, Weiss C, Sabel M, et al. 2015. Dual-time-point O-(2- ^{18}F)fluoroethyl)-L-tyrosine PET for grading of cerebral gliomas. *Eur Radiol* **25**: 3017–3024. doi:10.1007/s00330-015-3691-6
- Long NM, Smith CS. 2011. Causes and imaging features of false positives and false negatives on ^{18}F -PET/CT in oncologic imaging. *Insights Imaging* **2**: 679–698. doi:10.1007/s13244-010-0062-3
- Longo DL, Sun PZ, Consolino L, Michelotti FC, Uggeri F, Aime S. 2014. A general MRI-CEST ratiometric approach for pH imaging: demonstration of in vivo pH mapping with iobitridol. *J Am Chem Soc* **136**: 14333–14336. doi:10.1021/ja5059313
- Longo DL, Bartoli A, Consolino L, Bardini P, Arena F, Schwaiger M, Aime S. 2016. In vivo imaging of tumor metabolism and acidosis by combining PET and MRI-CEST pH imaging. *Cancer Res* **76**: 6463–6470. doi:10.1158/0008-5472.CAN-16-0825
- Marco-Rius I, Wright AJ, Hu D, Savic D, Miller JJ, Timm KN, Tyler D, Brindle KM, Comment A. 2021. Probing hepatic metabolism of [2- ^{13}C]dihydroxyacetone in vivo with ^1H -decoupled hyperpolarized ^{13}C -MR. *Magnetic Reson Mater Phys Biol Med* **34**: 49–56. doi:10.1007/s10334-020-00884-y
- Marini C, Ravera S, Buschiazzo A, Bianchi G, Orengo AM, Bruno S, Bottoni G, Emionite L, Pastorino F, Monteverde E, et al. 2016. Discovery of a novel glucose metabolism in cancer: the role of endoplasmic reticulum beyond glycolysis and pentose phosphate shunt. *Sci Rep* **6**: 25092. doi:10.1038/srep25092
- Marjańska M, Iltis I, Shestov AA, Deelchand DK, Nelson C, Uğurbil K, Henry P-G. 2010. In vivo ^{13}C spectroscopy in the rat brain using hyperpolarized [^{13}C]pyruvate and [^{13}C]pyruvate. *J Magn Reson* **206**: 210–218. doi:10.1016/j.jmr.2010.07.006
- Markovic S, Roussel T, Agemy L, Sasson K, Preise D, Scherz A, Frydman L. 2021. Deuterium MRSI characterizations of glucose metabolism in orthotopic pancreatic cancer mouse models. *NMR Biomed* **34**: e4569. doi:10.1002/nbm.4569
- Mayerhoefer ME, Prosch H, Beer L, Tamandl D, Beyer T, Hoeller C, Berzaczy D, Raderer M, Preusser M, Hochmair M, et al. 2020. PET/MRI versus PET/CT in oncology: a prospective single-center study of 330 examinations focusing on implications for patient management and cost considerations. *Eur J Nucl Med Mol Imaging* **47**: 51–60. doi:10.1007/s00259-019-04452-y
- McCormick PN, Greenwood HE, Glaser M, Maddocks ODK, Gendron T, Sander K, Gowrishankar G, Hoehne A, Zhang T, Shuhendler AJ, et al. 2018. Assessment of tumor redox status through (S)-4-(3- ^{18}F)fluoropropyl)-L-glutamic acid positron emission tomography imaging of system x_c^- activity. *Cancer Res* **79**: canres.2634.2018.
- McKinley ET, Ayers GD, Smith RA, Saleh SA, Zhao P, Washington MK, Coffey RJ, Manning HC. 2013. Limits of [^{18}F]-FLT PET as a biomarker of proliferation in oncology. *PLoS ONE* **8**: e58938. doi:10.1371/journal.pone.0058938
- Mikkelsen EFR, Mariager CØ, Nørtinger T, Qi H, Schulte RF, Jakobsen S, Frøkiær J, Pedersen M, Stødkilde-Jørgensen H, Laustsen C. 2017. Hyperpolarized [^{13}C]-acetate renal metabolic clearance rate mapping. *Sci Rep* **7**: 16002. doi:10.1038/s41598-017-15929-x
- Miloushev VZ, Granlund KL, Boltvanskii R, Lyashchenko SK, DeAngelis LM, Mellinshoff IK, Brennan CW, Tabar V, Yang TJ, Holodny AI, et al. 2018. Metabolic imaging of the human brain with hyperpolarized ^{13}C pyruvate demonstrates ^{13}C lactate production in brain tumor patients. *Cancer Res* **78**: 3755–3760. doi:10.1158/0008-5472.CAN-18-0221

T. Ruan and K.R. Keshari

- Minami N, Hong D, Taglang C, Batsios G, Gillespie AM, Viswanath P, Stevers N, Barger CJ, Costello JF, Ronen SM. 2023. Hyperpolarized δ -[^{13}C]gluconolactone imaging visualizes response to TERT or GABPB1 targeting therapy for glioblastoma. *Sci Rep* **13**: 5190. doi:10.1038/s41598-023-32463-1
- Mishkovsky M, Anderson B, Karlsson M, Lerche MH, Sherry AD, Gruetter R, Kovacs Z, Comment A. 2017. Measuring glucose cerebral metabolism in the healthy mouse using hyperpolarized ^{13}C magnetic resonance. *Sci Rep* **7**: 11719. doi:10.1038/s41598-017-12086-z
- Mishkovsky M, Gussyatiner O, Lanz B, Cudalbu C, Vassallo I, Hamou MF, Bloch J, Comment A, Gruetter R, Hegi ME. 2021. Hyperpolarized ^{13}C -glucose magnetic resonance highlights reduced aerobic glycolysis in vivo in infiltrative glioblastoma. *Sci Rep* **11**: 5771. doi:10.1038/s41598-021-85339-7
- Miura N, Mushti C, Sail D, AbuSalim JE, Yamamoto K, Brender JR, Seki T, AbuSalim DI, Matsumoto S, Camphausen KA, et al. 2021. Synthesis of [^{13}C -5- ^{12}C]- α -ketoglutarate enables noninvasive detection of 2-hydroxyglutarate. *NMR Biomed* **34**: e4588. doi:10.1002/nbm.4588
- Moreno KX, Harrison CE, Merritt ME, Kovacs Z, Malloy CR, Sherry AD. 2017. Hyperpolarized δ -[^{13}C]gluconolactone as a probe of the pentose phosphate pathway. *NMR Biomed* **30**: e3713. doi:10.1002/nbm.3713
- Nelson SJ, Kurhanewicz J, Vigneron DB, Larson PEZ, Harzstark AL, Ferrone M, van Criekinge M, Chang JW, Bok R, Park I, et al. 2013. Metabolic imaging of patients with prostate cancer using hyperpolarized [^{13}C]pyruvate. *Sci Transl Med* **5**: 198ra108. doi:10.1126/scitranslmed.3006070
- Neumann K, Flavell R, Wilson DM. 2017. Exploring metabolism in vivo using endogenous ^{11}C metabolic tracers. *Semin Nucl Med* **47**: 461–473. doi:10.1053/j.semnuclmed.2017.05.003
- Ninatti G, Sollini M, Bono B, Gozzi N, Fedorov D, Antunovic L, Gelardi F, Navarria P, Politi LS, Pessina F, et al. 2022. Preoperative [^{11}C]methionine PET to personalize treatment decisions in patients with lower-grade gliomas. *Neuro Oncol* **24**: 1546–1556. doi:10.1093/neuonc/noac040
- Nishii R, Tong W, Wendt R, Soghomonyan S, Mukhopadhyay U, Balatoni J, Mawlawi O, Bidaut L, Tinkey P, Borne A, et al. 2012. Pharmacokinetics, metabolism, biodistribution, radiation dosimetry, and toxicology of ^{18}F -fluoroacetate (^{18}F -FACE) in non-human primates. *Mol Imaging Biol* **14**: 213–224. doi:10.1007/s11307-011-0485-3
- Okubo S, Zhen HN, Kawai N, Nishiyama Y, Haba R, Tamiya T. 2010. Correlation of L-methyl- ^{11}C -methionine (MET) uptake with L-type amino acid transporter 1 in human gliomas. *J Neuro Oncol* **99**: 217–225. doi:10.1007/s11060-010-0117-9
- Oshima N, Ishida R, Kishimoto S, Beebe K, Brender JR, Yamamoto K, Urban D, Rai G, Johnson MS, Benavides G, et al. 2020. Dynamic imaging of LDH inhibition in tumors reveals rapid in vivo metabolic rewiring and vulnerability to combination therapy. *Cell Rep* **30**: 1798–1810.e4. doi:10.1016/j.celrep.2020.01.039
- Öz G, Alger JR, Barker PB, Bartha R, Bizzi A, Boesch C, Bolan PJ, Brindle KM, Cudalbu C, Dinçer A, et al. 2014. Clinical proton MR spectroscopy in central nervous system disorders. *Radiology* **270**: 658–679. doi:10.1148/radiol.13130531
- Park I, Larson PEZ, Zierhut ML, Hu S, Bok R, Ozawa T, Kurhanewicz J, Vigneron DB, VandenBerg SR, James CD, et al. 2010. Hyperpolarized ^{13}C magnetic resonance metabolic imaging: application to brain tumors. *Neuro Oncol* **12**: 133–144. doi:10.1093/neuonc/nop043
- Park JM, Josan S, Jang T, Merchant M, Yen Y, Hurd RE, Recht L, Spielman DM, Mayer D. 2012. Metabolite kinetics in C6 rat glioma model using magnetic resonance spectroscopic imaging of hyperpolarized [^{13}C]pyruvate. *Magn Reson Med* **68**: 1886–1893. doi:10.1002/mrm.24181
- Park JM, Josan S, Grafendorfer T, Yen Y, Hurd RE, Spielman DM, Mayer D. 2013. Measuring mitochondrial metabolism in rat brain in vivo using MR spectroscopy of hyperpolarized [^{13}C]pyruvate. *NMR Biomed* **26**: 1197–1203. doi:10.1002/nbm.2935
- Park JM, Spielman DM, Josan S, Jang T, Merchant M, Hurd RE, Mayer D, Recht LD. 2016. Hyperpolarized ^{13}C -lactate to ^{13}C -bicarbonate ratio as a biomarker for monitoring the acute response of anti-vascular endothelial growth factor (anti-VEGF) treatment. *NMR Biomed* **29**: 650–659. doi:10.1002/nbm.3509
- Park I, Larson PEZ, Gordon JW, Carvajal L, Chen H, Bok R, Criekinge MV, Ferrone M, Slater JB, Xu D, et al. 2018. Development of methods and feasibility of using hyperpolarized carbon-13 imaging data for evaluating brain metabolism in patient studies. *Magn Reson Med* **80**: 864–873. doi:10.1002/mrm.27077
- Park SY, Mosci C, Kumar M, Wardak M, Koglin N, Bullich S, Mueller A, Berndt M, Stephens AW, Chin FT, et al. 2020. Initial evaluation of (4S)-4-(3-[^{18}F]fluoropropyl)-l-glutamate (FSPG) PET/CT imaging in patients with head and neck cancer, colorectal cancer, or non-Hodgkin lymphoma. *EJNMMI Res* **10**: 100. doi:10.1186/s13550-020-00678-2
- Pavlova NN, Zhu J, Thompson CB. 2022. The hallmarks of cancer metabolism: still emerging. *Cell Metab* **34**: 355–377. doi:10.1016/j.cmet.2022.01.007
- Pisaneschi F, Gammon ST, Paolillo V, Qureshy SA, Piwnicka-Worms D. 2022. Imaging of innate immunity activation in vivo with a redox-tuned PET reporter. *Nat Biotechnol* **40**: 965–973. doi:10.1038/s41587-021-01169-y
- Ploessl K, Wang L, Lieberman BP, Qu W, Kung HF. 2012. Comparative evaluation of ^{18}F -labeled glutamic acid and glutamine as tumor metabolic imaging agents. *J Nucl Med* **53**: 1616–1624. doi:10.2967/jnumed.111.101279
- Puranik AD, Boon M, Purandare N, Rangarajan V, Gupta T, Moiyadi A, Shetty P, Sridhar E, Agrawal A, Dev I, et al. 2019. Utility of FET-PET in detecting high-grade gliomas presenting with equivocal MR imaging features. *World J Nucl Med* **18**: 266–272. doi:10.4103/wjnm.WJNM_89_18
- Qin H, Carroll VN, Striram R, Villanueva-Meyer JE, von Morze C, Wang ZJ, Mutch CA, Keshari KR, Flavell RR, Kurhanewicz J, et al. 2018. Imaging glutathione depletion in the rat brain using ascorbate-derived hyperpolarized MR and PET probes. *Sci Rep* **8**: 7928. doi:10.1038/s41598-018-26296-6
- Qu W, Zha Z, Lieberman BP, Mancuso A, Stetz M, Rizzi R, Ploessl K, Wise D, Thompson C, Kung HF. 2011. Facile synthesis [^{13}C -4- $^2\text{H}_2$]-L-glutamine for hyperpolarized

- MRS imaging of cancer cell metabolism. *Acad Radiol* **18**: 932–939. doi:10.1016/j.acra.2011.05.002
- Qu W, Oya S, Lieberman BP, Ploessl K, Wang L, Wise DR, Divgi CR, Chodosh LA, Chodosh LP, Thompson CB, et al. 2012. Preparation and characterization of L-[5-¹¹C]-glutamine for metabolic imaging of tumors. *J Nucl Med* **53**: 98–105. doi:10.2967/jnumed.111.093831
- Ragavan M, McLeod MA, Giacalone AG, Merritt ME. 2021. Hyperpolarized dihydroxyacetone is a sensitive probe of hepatic gluconeogenic state. *Metabolites* **11**: 441. doi:10.3390/metabol11070441
- Ragunand N, Zhang S, Sherry AD, Gillies RJ. 2002. In vivo magnetic resonance imaging of tissue pH using a novel pH-sensitive contrast agent, GdDOTA-4AmP. *Acad Radiol* **9**: S481–S483. doi:10.1016/S1076-6332(03)80270-2
- Rajendran JG, Schwartz DL, O'Sullivan J, Peterson LM, Ng P, Scharnhorst J, Grierson JR, Krohn KA. 2006. Tumor hypoxia imaging with [F-18] fluoromisonidazole positron emission tomography in head and neck cancer. *Clin Cancer Res* **12**: 5435–5441. doi:10.1158/1078-0432.CCR-05-1773
- Rao Y, Gammon S, Zacharias NM, Liu T, Salzillo T, Xi Y, Wang J, Bhattacharya P, Piwnica-Worms D. 2020. Hyperpolarized [1-¹³C]pyruvate-to-[1-¹³C]lactate conversion is rate-limited by monocarboxylate transporter-1 in the plasma membrane. *Proc Natl Acad Sci* **117**: 22378–22389. doi:10.1073/pnas.2003537117
- Rasey JS, Koh WJ, Grierson JR, Grunbaum Z, Krohn KA. 1989. Radiolabeled fluoromisonidazole as an imaging agent for tumor hypoxia. *Int J Radiat Oncol Biol Phys* **17**: 985–991. doi:10.1016/0360-3016(89)90146-6
- Reshetnyak YK, Andreev OA, Lehnert U, Engelman DM. 2006. Translocation of molecules into cells by pH-dependent insertion of a transmembrane helix. *Proc Natl Acad Sci* **103**: 6460–6465. doi:10.1073/pnas.0601463103
- Rich LJ, Bagga P, Wilson NE, Schnall MD, Detre JA, Haris M, Reddy R. 2020. ¹H magnetic resonance spectroscopy of ²H-to-¹H exchange quantifies the dynamics of cellular metabolism in vivo. *Nat Biomed Eng* **4**: 335–342. doi:10.1038/s41551-019-0499-8
- Rodrigues TB, Serrao EM, Kennedy BWC, Hu DE, Kettunen MI, Brindle KM. 2014. Magnetic resonance imaging of tumor glycolysis using hyperpolarized ¹³C-labeled glucose. *Nat Med* **20**: 93–97. doi:10.1038/nm.3416
- Rosenkrantz AB, Friedman K, Chandarana H, Melsaether A, Moy L, Ding YS, Jhaveri K, Beltran L, Jain R. 2016. Current status of hybrid PET/MRI in oncologic imaging. *Am J Roentgenol* **206**: 162–172. doi:10.2214/AJR.15.14968
- Rowe SP, Pomper MG. 2022. Molecular imaging in oncology: current impact and future directions. *CA Cancer J Clin* **72**: 333–352. doi:10.3322/caac.21713
- Saga T, Inubushi M, Koizumi M, Yoshikawa K, Zhang M, Tanimoto K, Horiike A, Yanagitani N, Ohyanagi F, Nishio M. 2015. Prognostic value of ¹⁸F-fluoroazomycin arabinoside PET/CT in patients with advanced non-small-cell lung cancer. *Cancer Sci* **106**: 1554–1560. doi:10.1111/cas.12771
- Saga T, Inubushi M, Koizumi M, Yoshikawa K, Zhang M-R, Obata T, Tanimoto K, Harada R, Uno T, Fujibayashi Y. 2016. Prognostic value of PET/CT with ¹⁸F-fluoroazomycin arabinoside for patients with head and neck squamous cell carcinomas receiving chemoradiotherapy. *Ann Nucl Med* **30**: 217–224. doi:10.1007/s12149-015-1048-5
- Sai KKS, Bashetti N, Chen X, Norman S, Hines JW, Meka O, Kumar JVS, Devanathan S, Deep G, Furdui CM, et al. 2019. Initial biological evaluations of ¹⁸F-KS1, a novel ascorbate derivative to image oxidative stress in cancer. *EJNMMI Res* **9**: 43. doi:10.1186/s13550-019-0513-x
- Salamanca-Cardona L, Shah H, Poot AJ, Correa FM, Gialleonardo VD, Lui H, Milousev VZ, Granlund KL, Tee SS, Cross JR, et al. 2017. In vivo imaging of glutamine metabolism to the oncometabolite 2-hydroxyglutarate in IDH1/2 mutant tumors. *Cell Metab* **26**: 830–841.e3. doi:10.1016/j.cmet.2017.10.001
- Sambuceti G, Cossu V, Bauckneht M, Morbelli S, Orengo A, Carta S, Ravera S, Bruno S, Marini C. 2021. ¹⁸F-fluoro-2-deoxy-D-glucose (FDG) uptake. What are we looking at? *Eur J Nucl Med Mol Imaging* **48**: 1278–1286. doi:10.1007/s00259-021-05368-2
- Schroeder MA, Atherton HJ, Ball DR, Cole MA, Heather LC, Griffin JL, Clarke K, Radda GK, Tyler DJ. 2009. Real-time assessment of Krebs cycle metabolism using hyperpolarized C magnetic resonance spectroscopy. *FASEB J* **23**: 2529–2538. doi:10.1096/fj.09-129171
- Serrao EM, Kettunen MI, Rodrigues TB, Dzien P, Wright AJ, Gopinathan A, Gallagher FA, Lewis DY, Frese KK, Almeida J, et al. 2016. MRI with hyperpolarised [1-¹³C] pyruvate detects advanced pancreatic preneoplasia prior to invasive disease in a mouse model. *Gut* **65**: 465. doi:10.1136/gutjnl-2015-310114
- Sharma R, D'Souza M, Jaimini A, Hazari PP, Saw S, Pandey S, Singh D, Solanki Y, Kumar N, Mishra AK, et al. 2016. A comparison study of ¹¹C-methionine and ¹⁸F-fluoro-deoxyglucose positron emission tomography-computed tomography scans in evaluation of patients with recurrent brain tumors. *Indian J Nucl Med* **31**: 93–102.
- Shields AF, Grierson JR, Dohmen BM, Machulla HJ, Stayanoff JC, Lawhorn-Crews JM, Obradovich JE, Muzik O, Mangner TJ. 1998. Imaging proliferation in vivo with [F-18]FLT and positron emission tomography. *Nat Med* **4**: 1334–1336. doi:10.1038/3337
- Singh J, Suh EH, Sharma G, Chen J, Hackett EP, Wen X, Sherry AD, Khemtong C, Malloy CR, Park JM, et al. 2021. ¹³C-labeled diethyl ketoglutarate derivatives as hyperpolarized probes of 2-ketoglutarate dehydrogenase activity. *Anal Sens* **1**: 156–160. doi:10.1002/anse.202100021
- Singhal T, Narayanan TK, Jain V, Mukherjee J, Mantil J. 2008. ¹¹C-L-methionine positron emission tomography in the clinical management of cerebral gliomas. *Mol Imaging Biol* **10**: 1–18. doi:10.1007/s11307-007-0115-2
- Skoura E, Ardeshtna K, Halsey R, Wan S, Kayani I. 2016. False-positive ¹⁸F-FDG PET/CT imaging. *Clin Nucl Med* **41**: e171–e172. doi:10.1097/RLU.0000000000001083
- Spence AM, Muzi M, Graham MM, O'Sullivan F, Krohn KA, Link JM, Lewellen TK, Lewellen B, Freeman SD, Berger MS, et al. 1998. Glucose metabolism in human malignant gliomas measured quantitatively with PET, 1-[C-11]glucose and FDG: analysis of the FDG lumped constant. *J Nucl Med* **39**: 440–448.
- Sriram R, Crieckinge MV, Hansen A, Wang ZJ, Vigneron DB, Wilson DM, Keshari KR, Kurhanewicz J. 2015. Real-time measurement of hyperpolarized lactate production and efflux as a biomarker of tumor aggressiveness in an MR

T. Ruan and K.R. Keshari

- compatible 3D cell culture bioreactor. *NMR Biomed* **28**: 1141–1149. doi:10.1002/nbm.3354
- Stødkilde-Jørgensen H, Laustsen C, Hansen ESS, Schulte R, Ardenkjaer-Larsen JH, Comment A, Frøkiær J, Ringgaard S, Bertelsen LB, Ladekarl M, et al. 2020. Pilot study experiences with hyperpolarized [$^{1-13}$ C]pyruvate MRI in pancreatic cancer patients. *J Magn Reson Imaging* **51**: 961–963. doi:10.1002/jmri.26888
- Stubbs M, Bhujwala ZM, Tozer GM, Rodrigues LM, Maxwell RJ, Morgan R, Howe FA, Griffiths JR. 1992. An assessment of 31 P MRS as a method of measuring pH in rat tumours. *NMR Biomed* **5**: 351–359. doi:10.1002/nbm.1940050606
- Sun PZ, Sorensen AG. 2008. Imaging pH using the chemical exchange saturation transfer (CEST) MRI: correction of concomitant RF irradiation effects to quantify CEST MRI for chemical exchange rate and pH. *Magn Reson Med* **60**: 390–397. doi:10.1002/mrm.21653
- Sushentsev N, McLean MA, Warren AY, Benjamin AJV, Brodie C, Frary A, Gill AB, Jones J, Kaggie JD, Lamb BW, et al. 2022. Hyperpolarised 13 C-MRI identifies the emergence of a glycolytic cell population within intermediate-risk human prostate cancer. *Nat Commun* **13**: 466. doi:10.1038/s41467-022-28069-2
- Tang S, Meng MV, Slater JB, Gordon JW, Vigneron DB, Stohr BA, Larson PEZ, Wang ZJ. 2021. Metabolic imaging with hyperpolarized 13 C pyruvate magnetic resonance imaging in patients with renal tumors—initial experience. *Cancer* **127**: 2693–2704. doi:10.1002/cncr.33554
- Tapmeier TT, Moshnikova A, Beech J, Allen D, Kinchesh P, Smart S, Harris A, McIntyre A, Engelman DM, Andreev OA, et al. 2015. The pH low insertion peptide pHLLIP variant 3 as a novel marker of acidic malignant lesions. *Proc Natl Acad Sci* **112**: 9710–9715. doi:10.1073/pnas.1509488112
- Tee SS, Kim N, Cullen Q, Eskandari R, Mamakhanyan A, Srouji RM, Chirayil R, Jeong S, Shakiba M, Kastenhuber ER, et al. 2022. Ketohexokinase-mediated fructose metabolism is lost in hepatocellular carcinoma and can be leveraged for metabolic imaging. *Sci Adv* **8**: eabm7985. doi:10.1126/sciadv.abm7985
- Temma T, Kawashima H, Kondo N, Yamazaki M, Koshino K, Iida H. 2018. One-pot enzymatic synthesis of l-[3- 11 C] lactate for pharmacokinetic analysis of lactate metabolism in rat brain. *Nucl Med Biol* **64–65**: 28–33. doi:10.1016/j.nucmedbio.2018.07.001
- Thelwall PE, Yemin AY, Gillian TL, Simpson NE, Kasibhatla MS, Rabbani ZN, Macdonald JM, Blackband SJ, Gamcsik MP. 2005. Noninvasive in vivo detection of glutathione metabolism in tumors. *Cancer Res* **65**: 10149–10153. doi:10.1158/0008-5472.CAN-05-1781
- Thelwall PE, Simpson NE, Rabbani ZN, Clark MD, Pourdeyhimi R, Macdonald JM, Blackband SJ, Gamcsik MP. 2012. In vivo MR studies of glycine and glutathione metabolism in a rat mammary tumor. *NMR Biomed* **25**: 271–278. doi:10.1002/nbm.1745
- This JA. 2004. Understanding the standardized uptake value, its methods, and implications for usage. *J Nucl Med* **45**: 1431–1434.
- Timm KN, Hu DE, Williams M, Wright AJ, Kettunen MI, Kennedy BWC, Larkin TJ, Dzien P, Marco-Rius I, Bohnediek SE, et al. 2017. Assessing oxidative stress in tumors by measuring the rate of hyperpolarized [$^{1-13}$ C]dehydroascorbic acid reduction using 13 C magnetic resonance spectroscopy. *J Biol Chem* **292**: 1737–1748. doi:10.1074/jbc.M116.761536
- Tong X, Srivatsan A, Jacobson O, Wang Y, Wang Z, Yang X, Niu G, Kiesewetter DO, Zheng H, Chen X. 2016. Monitoring tumor hypoxia using 18 F-FMISO PET and pharmacokinetics modeling after photodynamic therapy. *Sci Rep* **6**: 31551. doi:10.1038/srep31551
- Tran M, Latifoltojar A, Neves JB, Papoutsaki M-V, Gong F, Comment A, Costa ASH, Glaser M, Tran-Dang MA, Sheikh SE, et al. 2019. First-in-human in vivo non-invasive assessment of intra-tumoral metabolic heterogeneity in renal cell carcinoma. *BJR Case Rep* **5**: 20190003.
- Ursprung S, Woitek R, McLean MA, Priest AN, Crispin-Ortuzar M, Brodie CR, Gill AB, Gehrung M, Beer L, Riddick ACP, et al. 2022. Hyperpolarized 13 C-pyruvate metabolism as a surrogate for tumor grade and poor outcome in renal cell carcinoma—a proof of principle study. *Cancers (Basel)* **14**: 335. doi:10.3390/cancers14020335
- Varma G, Seth P, de Souza PC, Callahan C, Pinto J, Vaidya M, Sonzogni O, Sukhatme V, Wulf GM, Grant AK. 2021. Visualizing the effects of lactate dehydrogenase (LDH) inhibition and *LDH-A* genetic ablation in breast and lung cancer with hyperpolarized pyruvate NMR. *NMR Biomed* **34**: e4560. doi:10.1002/nbm.4560
- Våvere AL, Kridel SJ, Wheeler FB, Lewis JS. 2008. $^{1-11}$ C-acetate as a PET radiopharmaceutical for imaging fatty acid synthase expression in prostate cancer. *J Nucl Med* **49**: 327–334. doi:10.2967/jnumed.107.046672
- Våvere AL, Biddlecombe GB, Spees WM, Garbow JR, Wijesinghe D, Andreev OA, Engelman DM, Reshetnyak YK, Lewis JS. 2009. A novel technology for the imaging of acidic prostate tumors by positron emission tomography. *Cancer Res* **69**: 4510–4516. doi:10.1158/0008-5472.CAN-08-3781
- Venneti S, Dunphy MP, Zhang H, Pitter KL, Zanzonico P, Campos C, Carlin SD, Rocca GL, Lyashchenko S, Ploessl K, et al. 2015. Glutamine-based PET imaging facilitates enhanced metabolic evaluation of gliomas in vivo. *Sci Transl Med* **7**: 274ra17. doi:10.1126/scitranslmed.aaa1009
- Viola-Villegas NT, Carlin SD, Ackerstaff E, Sevak KK, Divilov V, Serganova I, Kruchevsky N, Anderson M, Blasberg RG, Andreev OA, et al. 2014. Understanding the pharmacological properties of a metabolic PET tracer in prostate cancer. *Proc Natl Acad Sci* **111**: 7254–7259. doi:10.1073/pnas.1405240111
- Virani N, Kwon J, Zhou H, Mason R, Berbeco R, Protti A. 2021. In vivo hypoxia characterization using blood oxygen level dependent magnetic resonance imaging in a preclinical glioblastoma mouse model. *Magn Reson Imaging* **76**: 52–60. doi:10.1016/j.mri.2020.11.003
- Viswanath P, Batsios G, Ayyappan V, Taglang C, Gillespie AM, Larson PEZ, Luchman HA, Costello JF, Pieper RO, Ronen SM. 2021a. Metabolic imaging detects elevated glucose flux through the pentose phosphate pathway associated with TERT expression in low-grade gliomas. *Neuro Oncol* **23**: 1509–1522. doi:10.1093/neuonc/noab093
- Viswanath V, Zhou R, Lee H, Li S, Cragin A, Doot RK, Mankoff DA, Pantel AR. 2021b. Kinetic modeling of 18 F-(2S,4R)4-fluoroglutamine in mouse models of breast

- cancer to estimate glutamine pool size as an indicator of tumor glutamine metabolism. *J Nucl Med* **62**: 1154–1162. doi:10.2967/jnumed.120.250977
- Walker-Samuel S, Ramasawmy R, Torrealdea F, Rega M, Rajkumar V, Johnson SP, Richardson S, Gonçalves M, Parkes HG, Årstad E, et al. 2013. In vivo imaging of glucose uptake and metabolism in tumors. *Nat Med* **19**: 1067–1072. doi:10.1038/nm.3252
- Wang P, Sun C, Zhu T, Xu Y. 2015. Structural insight into mechanisms for dynamic regulation of PKM2. *Protein Cell* **6**: 275–287. doi:10.1007/s13238-015-0132-x
- Wang ZJ, Ohliger MA, Larson PEZ, Gordon JW, Bok RA, Slater J, Villanueva-Meyer JE, Hess CP, Kurhanewicz J, Vigneron DB. 2019. Hyperpolarized ¹³C MRI: state of the art and future directions. *Radiology* **291**: 182391.
- Wang Q, Parish C, Niedbalski P, Ratnakar J, Kovacs Z, Lumata L. 2020. Hyperpolarized 89Y-EDTMP complex as a chemical shift-based NMR sensor for pH at the physiological range. *J Magn Reson* **320**: 106837. doi:10.1016/j.jmr.2020.106837
- Warburg O. 1956. On the origin of cancer cells. *Science* **123**: 309–314. doi:10.1126/science.123.3191.309
- Ward KM, Balaban RS. 2000. Determination of pH using water protons and chemical exchange dependent saturation transfer (CEST). *Magn Reson Med* **44**: 799–802. doi:10.1002/1522-2594(200011)44:5<799::AID-MRM18>3.0.CO;2-S
- Ward CS, Venkatesh HS, Chaumeil MM, Brandes AH, Van-Criekinge M, Dafni H, Sukumar S, Nelson SJ, Vigneron DB, Kurhanewicz J, et al. 2010. Noninvasive detection of target modulation following phosphatidylinositol 3-kinase inhibition using hyperpolarized ¹³C magnetic resonance spectroscopy. *Cancer Res* **70**: 1296–1305. doi:10.1158/0008-5472.CAN-09-2251
- Wardak M, Sonni I, Fan AP, Minamimoto R, Jamali M, Hatami N, Zaharchuk G, Fischbein N, Nagpal S, Li G, et al. 2022. ¹⁸F-FSPG PET/CT imaging of system x_c⁻ transporter activity in patients with primary and metastatic brain tumors. *Radiology* **303**: 620–631. doi:10.1148/radiol.203296
- Wilson DM, Keshari KR, Larson PEZ, Chen AP, Hu S, Crieckinge MV, Bok R, Nelson SJ, Macdonald JM, Vigneron DB, et al. 2010. Multi-compound polarization by DNP allows simultaneous assessment of multiple enzymatic activities in vivo. *J Magn Reson* **205**: 141–147. doi:10.1016/j.jmr.2010.04.012
- Woitek R, McLean MA, Gill AB, Grist JT, Provenzano E, Patterson AJ, Ursprung S, Torheim T, Zaccagna F, Locke M, et al. 2020. Hyperpolarized ¹³C MRI of tumor metabolism demonstrates early metabolic response to neoadjuvant chemotherapy in breast cancer. *Radiol Imaging Cancer* **2**: e200017. doi:10.1148/rycan.2020200017
- Wuest M, Trayner BJ, Grant TN, Jans HS, Mercer JR, Murray D, West FG, McEwan AJB, Wuest F, Cheeseman CI. 2011. Radiopharmacological evaluation of 6-deoxy-6-[¹⁸F]fluoro-D-fructose as a radiotracer for PET imaging of GLUT5 in breast cancer. *Nucl Med Biol* **38**: 461–475. doi:10.1016/j.nucmedbio.2010.11.004
- Wuest M, Hamann I, Bouvet V, Glubrecht D, Marshall A, Trayner B, Soueidan O, Krys D, Wagner M, Cheeseman C, et al. 2017. Molecular imaging of GLUT1 and GLUT5 in breast cancer: a multitracer PET imaging study in mice. *Mol Pharmacol* **93**: mol.117.110007.
- Wyatt LC, Moshnikova A, Crawford T, Engelman DM, Andreev OA, Reshetnyak YK. 2018. Peptides of pHLIP family for targeted intracellular and extracellular delivery of cargo molecules to tumors. *Proc Natl Acad Sci* **115**: E2811–E2818. doi:10.1073/pnas.1715350115
- Xu HN, Kadlecck S, Profka H, Glickson JD, Rizi R, Li LZ. 2014. Is higher lactate an indicator of tumor metastatic risk? A pilot MRS study using hyperpolarized ¹³C-pyruvate. *Acad Radiol* **21**: 223–231. doi:10.1016/j.acra.2013.11.014
- Xu X, Chan KWY, Knutsson L, Artemov D, Xu J, Liu G, Kato Y, Lal B, Laterra J, McMahon MT, et al. 2015. Dynamic glucose enhanced (DGE) MRI for combined imaging of blood–brain barrier break down and increased blood volume in brain cancer. *Magnet Reson Med* **74**: 1556–1563. doi:10.1002/mrm.25995
- Xu W, Gao L, Shao A, Zheng J, Zhang J. 2017. The performance of ¹¹C-methionine PET in the differential diagnosis of glioma recurrence. *Oncotarget* **8**: 91030–91039. doi:10.18632/oncotarget.19024
- Yamamoto K, Brender JR, Seki T, Kishimoto S, Oshima N, Choudhuri R, Adler SS, Jagoda EM, Saito K, Devasahayam N, et al. 2020. Molecular imaging of the tumor microenvironment reveals the relationship between tumor oxygenation, glucose uptake, and glycolysis in pancreatic ductal adenocarcinoma. *Cancer Res* **80**: 2087–2093. doi:10.1158/0008-5472.CAN-19-0928
- Yasui H, Kawai T, Matsumoto S, Saito K, Devasahayam N, Mitchell JB, Camphausen K, Inanami O, Krishna MC. 2017. Quantitative imaging of pO₂ in orthotopic murine gliomas: hypoxia correlates with resistance to radiation. *Free Radic Res* **51**: 861–871. doi:10.1080/10715762.2017.1388506
- Yoshii Y, Waki A, Furukawa T, Kiyono Y, Mori T, Yoshii H, Kudo T, Okazawa H, Welch MJ, Fujibayashi Y. 2009. Tumor uptake of radiolabeled acetate reflects the expression of cytosolic acetyl-CoA synthetase: implications for the mechanism of acetate PET. *Nucl Med Biol* **36**: 771–777. doi:10.1016/j.nucmedbio.2009.05.006
- Zaccagna F, McLean MA, Grist JT, Kaggie J, Mair R, Riemer F, Woitek R, Gill AB, Deen S, Daniels CJ, et al. 2022. Imaging glioblastoma metabolism by using hyperpolarized [¹⁻¹³C]pyruvate demonstrates heterogeneity in lactate labeling: a proof of principle study. *Radiol Imaging Cancer* **4**: e210076. doi:10.1148/rycan.210076
- Zacharias NM, Chan HR, Sailasuta N, Ross BD, Bhattacharya P. 2012. Real-time molecular imaging of tricarboxylic acid cycle metabolism in vivo by hyperpolarized 1-¹³C diethyl succinate. *J Am Chem Soc* **134**: 934–943. doi:10.1021/ja2040865
- Zhang X, Lin Y, Gillies RJ. 2010. Tumor pH and its measurement. *J Nucl Med* **51**: 1167–1170. doi:10.2967/jnumed.109.068981
- Zhou R, Pantel AR, Li S, Lieberman BP, Ploessl K, Choi H, Blankemeyer E, Lee H, Kung HF, Mach RH, et al. 2017. [¹⁸F](2S,4R)4-fluoroglutamine PET detects glutamine pool size changes in triple-negative breast cancer in response to glutaminase inhibition. *Cancer Res* **77**: 1476–1484. doi:10.1158/0008-5472.CAN-16-1945